



ADAPT TO NEW CHALLENGES, TAKE
ADVANTAGE OF NEW OPPORTUNITIES

COPPER ALLOYS 2022

Conference Proceedings

kupfer_

Scientific conference on copper materials

 SWERIM

R.
I.
S.E

COPPER ALLOYS 2022

Experimental optimization of tool geometry and lubricoolant supply in plunge milling of lead-free Brass (Baier, S.; Brans, K.; Schraknepper, D.; Bergs, T.).....	4
Modern clad material systems for battery, charging and thermal management challenges in automotive electrification (Frehn, A.; Greschner, U.).....	8
Wettability of Copper on Industrial Filter Materials (Gumban, C. G.; Hubálková, J.; Fankhänel, B.; Charitos, A.; Aneziris, C. G.; Voigt, C.).....	12
Microstructure and crystallographic variations in different positions in OFP copper outer shell of canisters for spent nuclear fuel storage (Hagström, J.; Sandström, R.; Sarnet, J.)	16
Casting properties of lead-free brass (Hagström, J.; Nordin, M.; Persson, P. E.)	20
CuSn4Zn2PS – Lead Free Gunmetal for drinking water applications (Haake, M.; Hansen, A.)	23
Efficient processing of copper and its alloys with blue diode laser (Heine, L.-M.; Schlett, M.; Ocylok, S.; Rütering, M.)	24
Phase Transformations and Kinetic Simulations of Cu-based Alloys (Jansson, Å.; Tang, Y.; Jin, S.; Ghasemi, M.; Lancelot, C. M.; Grundy, N.; Chen, Q.; Bratberg, J.).....	28
Corrosion resistance of lead-free brass alloys in contact with drinking water (Klein, T.).....	32
Effect of Heat Treatment on Transformation Temperatures, Microstructure, and Deformation Behavior of a High Temperature Copper-based Shape Memory Alloy (Kranner, C.; Schelnberger, B.; Hoffmann, F.; Keßler, R.; Krieg, R.; Theiß, R.; Dültgen, P.)	34
Copper Wave Springs for Electromechanical Applications (Philipp, J.; Frehn, A.; Seeger, S., Aust, M.; Hertweck, B.).....	39
Innovative Laser Technologies for Copper Applications in e-Mobility (Möller, M.; Papastathopoulos, E.; Bocksrocker, O.)	40
Investigation of heat treatment to improve the machinability of lead-free brass alloy CW511L (Müller, M. S.; Tomovic Petrovic, S.; Sørby, K.).....	42

Distribution of alloying elements and measurable shape memory effect of continuous cast copper aluminum alloy

(Schelnberger, B.; Kranner, C.; Krieg, R.; Theiß, R.; Dültgen, P.) **46**

Corrosion susceptibility of the CuZn35Pb1,5AlAs (CW625N) brass alloy in various environments

(Tomovic-Petrovic, S.; Gulbrandsen-Dahl, S.; Wenner, S.) **52**

Assessment and Comparison of the Machinability of Innovative Copper Alloys

(Zachert, C.; Brans, K.; Schraknepper, D.; Bergs, T.) **56**

Production of Polypropylene and Polyethylene Matrix Copper Reinforced Bio-composite and Investigation of Mechanical, Thermal and Morphologic Properties

(Kaplan, Ü.; Birol, F.; Kaya, Ö. A.; Zığındere, O.; Taşdemir, M.) **60**

Analysis of CuSn8 components manufactured using the material jetting process

(Plötz, M.; Kirchebner, B.; Volk, W.; Lechner, P.) **64**

Overview of non-metallic inclusions in Copper and Copper Alloys

(Voigt, C.; Gumban, G. C.; Hubálková, J.; Aneziris, C. G.) **67**

Sponsors:



ISBN 978-3-910411-01-2

Experimental optimization of tool geometry and lubricoolant supply in plunge milling of lead-free Brass

Baier, S. (1); Brans, K. (1); Schraknepper, D. (1); Bergs, T. (1, 2)

Electrical connectors are currently gaining relevance due to continuous electrification in mobility, manufacturing and other applications. Many connector types have rectangular geometry elements that are used for clamping cables. Plunge milling is a critical process step in mass manufacturing of these rectangular shapes in electrical connector components. These shapes are manufactured by drilling a pilot hole and subsequently plunge milling at an offset one or more times. Since the plunge-milled cavity serves as guidance for the final broaching cut, its geometric accuracy is crucial for staying within the workpiece-specific tolerances. In machining of lead-free brass alloys, process reliability is insufficient for automated production due to lacking accuracy and tool breakage. In previous research, insufficient chip evacuation and high radial cutting forces were identified as the main cause for this reduction in process reliability.

In this publication, the working mechanisms and interaction of tool geometry and process kinematics regarding chip evacuation and process forces are analysed in detail for the plunge milling of CuZn21Si3P, CuZn37 and CuZn42. Additionally, the effect of direct lubricoolant supply on chip evacuation is analyzed. Regarding tool geometry, the effects of the cutting edge angle κ_c , the number of cutting edges z and the face rake angle γ_s on chip form and cutting force components are investigated. These results improve process reliability in plunge milling of lead-free brass alloys.

Plunge milling refers to a machining process with purely axial feed direction. Therefore, it belongs in the category of drilling processes even if the term plunge milling is established in the industry [KLOC18]. In machining of copper base alloys, plunge milling is mainly used as an intermediate step for mass manufacturing of electrical connectors (Figure 1). After drilling, one or more axial plunge milling cuts are performed, resulting in a figure-eight-shape. The final geometry is manufactured by a broaching tool which has the same profile as the cavity. Due to the typically small inner profiles (width of ca. 1.5 mm to 5 mm) of the terminals, the broach has a low stiffness. Therefore, the plunge milled cavity provides guidance to the broach. The accuracy of the broached channel in the finished workpiece is therefore determined by the accuracy of the prior plunge milling process. In plunge milling, the area of engagement has a sickle shape and is not sym-

metrical to the tools rotation axis like in conventional drilling. Therefore, the radial forces acting on the tool are not cancelling out and cause a bending moment on the tool. This leads to deflection of the tool tip which leads to a deviation of the cavity. This challenge is especially pronounced in plunge milling of lead-free ($m_{pb} < 0,1 \text{ %Mass}$) brass alloys due to disadvantageous chip forms, increased friction and higher cutting force in comparison

to similar leaded alloys. This causes a drastic (5 - 10-fold) increase in radial cutting force components over the course of a cut [BAIE 21b]. Maximum radial force components reached up to $F_{rad} = 160 \text{ N}$ causing frequent breakage of the carbide end mills with a diameter of $d = 2 \text{ mm}$. The result is an instable process with low accuracy and high risk of tool breakage. Insufficient chip evacuation and subsequent build-up of chips in the tools flutes and the cavities was identified as the main cause for this force increase [BAIE 21c, BAIE 21a].

It is therefore the aim of this work to investigate possible strategies for the stabilization of this process and to minimize the radial force components. As a first step, the effect of directed lubricoolant supply with and without elevated pressure on the radial force will be analysed. As a secondary step, tool geometry is varied regarding cutting edge angle κ_c , the number of cutting edges z and the face rake angle γ_s .

Procedure

The workpiece materials CuZn37 (Diehl alloy 023), CuZn42 (Aurubis PNA 277) and CuZn21Si3P (Wieland



Fig. 1: Typical manufacturing sequence in production of rectangular cavities in electrical terminals

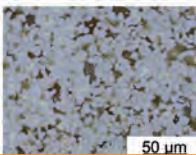
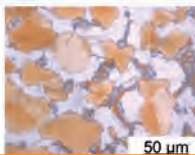
Material	CuZn37	CuZn42	CuZn21Si3P
Phase content	100 % α -CuZn	50 % α -CuZn, 50 % β -CuZn,	60 % α -CuZn, 40 % κ -CuZnSi
Hardness HBW 2.5/31.25	108 - 112	152 - 156	159 - 176
Tensile strength R_m / MPa	400	595	674 - 687
Microstructure	  		
	50 μm	50 μm	50 μm

Table 1: Workpiece materials and their properties

SW1) were chosen for the experiments in order to represent a wide range of available brass alloys (Table 1). CuZn37 was chosen as a homogenous brass alloy with 100 % α -CuZn content. The CuZn42 alloy had roughly equal concentrations of α - and β -CuZn. CuZn21Si3P was selected from the class of CuZnSi alloys.

The materials were provided in the form of cylindrical rods with a diameter of $d = 10$ mm from which workpieces with a length of $l = 14$ mm were cut. The experiments were conducted of a four-axis milling centre NHX 5000 from DMG Mori (Figure 2). A piezoelectric dynamometer 9119AA2 from Kistler measured the cutting force components with a sample frequency of $f = 10$ kHz. The clamping device was

direct supply and dry machining were investigated. The cutting speed was set to $v_c = 50$ m/min.

Cutting the more brittle CuZn21Si3P alloy generally forms a high degree of chip segmentation whereas the more ductile binary brass alloys generally show reduced degrees of chip segmentation with increasing contents in α -CuZn ([HOFM18], [NOBE14]).

In plunge milling, chip length is limited due to the process' kinematics resulting in an interrupted cut. The chip form, however, is still relevant due to the frequent clogging of the tool's flutes and the milled cavities. Micrographs of the chips cross sections allowed an assessment of the chip formation mechanism. The chips

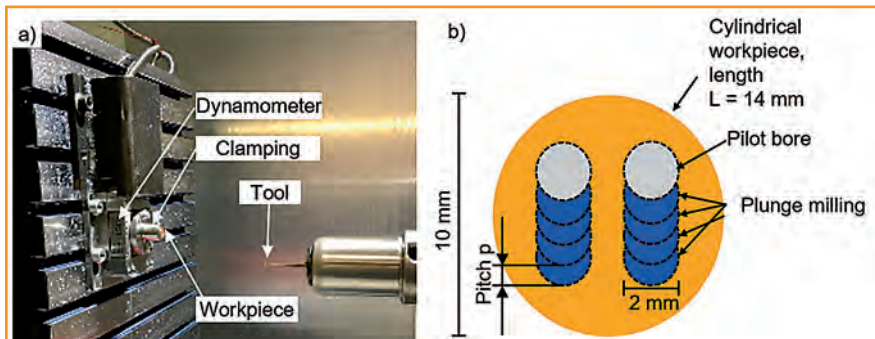


Fig. 2: Experimental setup in the machining centre (a) and workpiece geometry (b)

The tools were manufactured by Gühring KG and had a diameter of $d = 2$ mm (Figure 3). In order to preserve

made of CuZn37 were continuous with mostly homogenous deformation of the initial microstructure (Figure 3). In plunge milling of CuZn42, some segmentation in the form of strain localization occurred. The chips cut from CuZn21Si3P showed evenly dis-

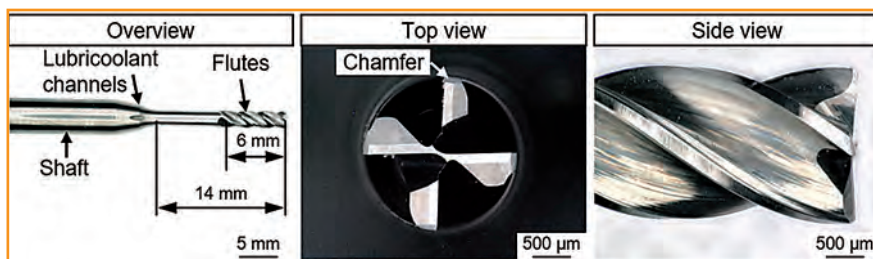


Fig. 3: Tool overview

especially designed to be lightweight in order to have as high a resonance frequency as possible when mounted on the dynamometer. The plunge milling tests were performed in the front face of the workpieces through the entire length of the workpiece ($L = 14$ mm, Figure 2b). After manufacturing two pilot bores, four plunging cuts were done on each side of the workpiece. The parameters were kept constant within each workpiece. So, every experimental point was performed twice. Flood cooling with a 6 % emulsion of Blaser Vasco TP lubricoolant was used as a standard. Additionally,

the tools stiffness in the cylindrical section, the flutes were only $l = 6$ mm long. Four lubricoolant channels were situated in the tools shaft and enabled a directed lubricoolant supply into the milled cavity. Tool geometry was varied coming from a reference geometry with separate tools with different cutting edge angle κ_r , number of teeth z and rake angle γ_s (Table 2). All cutting edges were considered to be sharp with cutting edge radii between $r_\beta = 7.7 \mu\text{m}$ and $r_\beta = 10.6 \mu\text{m}$.

In conventional turning operations, the three workpiece materials exhibit significant differences in chip form.

	Reference	Variation
Cutting edge angle κ_r / °	94	100
Number of teeth z / -	4	3; 2
Rake angle γ_s / °	5	10
Manufacturer	Gühring KG	
Nomination	303926025	
Substrate	Carbide (K55SF), uncoated	
Corner chamfer b_v / mm	F0.08 x 45°	
Tool diameter D / mm	2	
Radial rake angle γ_r / °	3	
Face clearance angle α_s / °	10	
Helix angle ϵ / °	35	
Shaft diameter D_s / mm	4	

Table 2: Tool geometry and variations

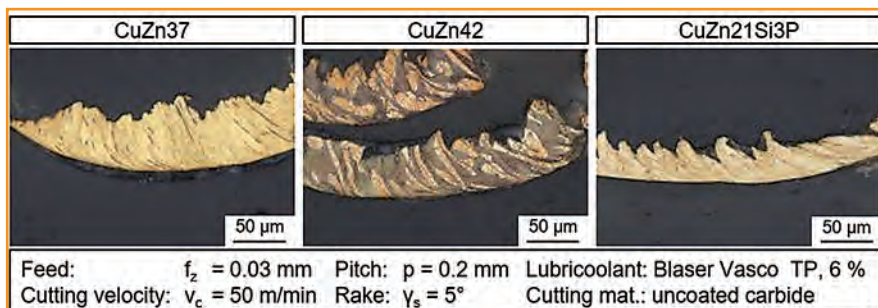


Fig. 4: Longitudinal chip cross sections from the three workpiece materials

tributed segmentation. This indicates a lower force in cutting this material due to less deformation work being done in chip formation which has been measured in previous works ([BAIE 21a]). The CuZn37 and CuZn42 chips appear thicker than CuZn21Si3P chips in the microsections. However, a valid measurement of the chip thickness ratio could not be taken due to the chips not being embedded evenly.

In order to achieve a more stable process, the chips evacuation out of the cavity needs to be optimized. Figure 5 shows the radial force component F_{rad} over time for four consecutive plunge milling cuts. With conventional flood cooling, the results from earlier work ([BAIE 21b], [BAIE 21a]) were reproduced: A short time after tool entry, the radial force increased drastically by about five to ten times reaching a maximum at the end of the cut due to chips building up inside the cavity. The peak lowered within the following cuts due to the cavities size increasing with every cut.

Dry machining was evaluated in order to test the hypothesis, that the coolant pushing the chips back into the cavity might hinder chip evacuation. This had little impact on the progression of the radial force and the hypothesis was therefore dismissed.

As a second step, the lubricoolant was supplied through the tool shafts nozzles directed towards the tool tip inside the cavity. This is referred to as direct cooling. With direct cooling with a lubricoolant supply pressure of $p = 3.3$ bar, the radial force remained mostly constant throughout a cut. After about one third of the cut, a slight increase in radial force was observed in all cuts. This was caused by the entry of the cylindrical section of the tool shaft without flutes into the cavity after about $l_f = 6 \text{ mm}$ of cutting depth (see

Figure 3). The entry of the cylindrical shaft reduced the total cross section,

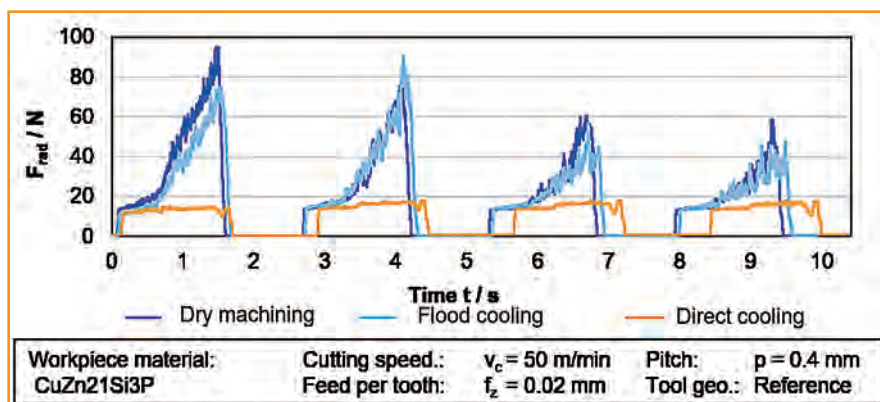


Fig. 5: Radial force over time in plunge milling of CuZn21Si3P

which lead to the increase in radial force. The same effect was observed in plunge milling of the other workpiece materials CuZn37 and CuZn42. Trials were also done with elevated coolant supply pressures of up to $p = 50$ bars. This showed no significant impact on radial force, indicating that a pressure of $p = 3.3$ bar is sufficient for advantageous chip evacuation. With the increase cutting forces during a cut minimized, the process has been stabilized and reliability increased in comparison to the state of technology. Tool geometry influences the radial force in plunge milling. Further

experiments with systematically varied tool geometries (see Table 2) were therefore conducted under conditions with sufficient chip evacuation. The effect of a reduction of the number of teeth from $z = 4$ (reference) to $z = 3$ and $z = 2$ aimed at further improving chip evacuation due to the larger flutes between the teeth. The mean chip cross section reduces linearly with the number of teeth. Therefore, a linear interdependency between the number of teeth z and radial force F_{rad} was expected. However, radial

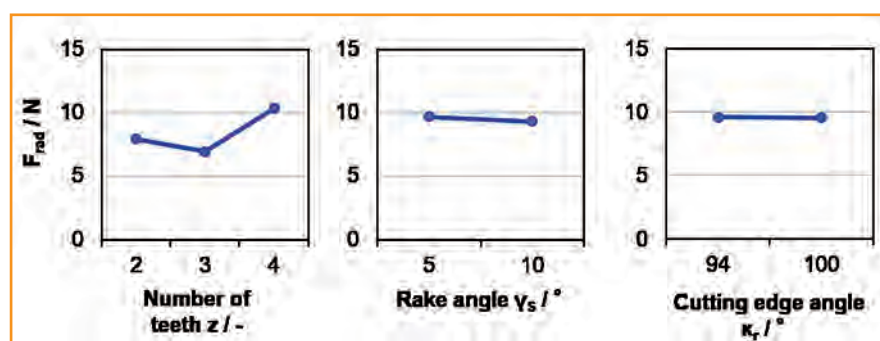


Fig. 6: Mean effect of tool geometry features on radial force in plunge milling of lead free brass

the tools chamfer. Therefore, rubbing and squeezing effects are dominant in this stage of the process, likely causing a higher degree of vibration of the tool tip. In plunge milling with $z = 3$ teeth, upon entry or exit of one tooth, another tooth will always be located at an angle of 120° in the workpiece. This resulted in a stabilizing effect reducing the process dynamics and therefore the mean radial force.

The face rake angle was varied between $\gamma_s = 5^\circ$ and $\gamma_s = 10^\circ$ with the intention of lowering the cutting force F_c which is a large part of the radial force in plunge milling. The effect of this parameter on radial force only resulted in a reduction in mean radial force of $\Delta F_{\text{rad}} = 0,4 \text{ N}$.

The cutting force F_c is usually the largest force component in metal cutting and it is orthogonal to the cutting edge. The variation of the cutting edge angle κ_r was intended to shift the direction of the cutting force towards the outside of the tool, counteracting other force components acting in radial direction. This effect was not measurable when varying between $\kappa_r = 94^\circ$ and $\kappa_r = 100^\circ$.

Conclusion and outlook

Using conventional flood cooling in plunge milling, radial forces increased drastically throughout the duration of a cut. With the application of direct lubricant supply, even at low pressures, chip evacuation was improved in plunge milling of lead-free brass alloys.

Under such stabilized conditions, the radial force and its dynamics were further reduced by using a tool with three instead of four teeth. Since tool bending is caused by radial forces, these results are crucial for improving process reliability and accuracy. In further research, the effects of these measures on workpiece accuracy and tool wear should be investigated.

References

- [BAIE 21a] Baier, S.; Kokozinski, L.; Schraknepper, D.; Bergs, T.: Tool geometry analysis for plunge milling of lead-free CuZn-alloys. In: ESAFORM 2021. International Conference on Material Forming, Liège, Belgium, 2021
- [BAIE 21b] Baier, S.; Schraknepper, D.; Bergs, T.: Entwicklung angepasster Werkzeuge und Prozesse zur Steigerung der Produktivität und Prozesssicherheit beim Fräsen innovativer bleifreier Kupferwerkstoffe. Schlussbericht zu IGF-Vorhaben Nr. 20029 N. Aachen: RWTH Aachen University, 2021
- [BAIE 21c] Baier, S.; Schraknepper, D.; Bergs, T.: Werkstoffspezifische Entwicklung der Werkzeuggeometrie für das Tauchfräsen von bleifreien Cu-Zn-Werkstoffen. In: Deutsches Kupferinstitut (Hrsg.): Kupfer-Symposium 2021. Werkstofftagung vom 24.-25. November 2021. Düsseldorf, 2021, S. 40–42
- [HOFM18] Hofmann, U.; Nobel, C.; Baier, S.; Buchkremer, S.; Döbbeler, B.; Klocke, F.: Über den Einfluss von Werkstoffkennwerten auf das Spanbruchverhalten von bleiarmem Messing. In: Materialwissenschaft und Werkstofftechnik, 49. Jg., 2018, Bd. 6, S. 753–768
- [KLOC18] Klocke, F.: Fertigungsverfahren 1. Zerspanung mit geometrisch bestimmter Schneide. (Reihe: VDI-Buch). 9. Aufl. 2018. Berlin, Heidelberg: Springer Vieweg, 2018
- [NOBE14] Nobel, C.; Klocke, F.; Lung, D.; Wolf, S.: Machinability Enhancement of Lead-free Brass Alloys. In: Procedia CIRP, 14. Jg., 2014, S. 95–100

(1) *Laboratory for Machine Tools and Production Engineering (WZL) of RWTH Aachen University, Aachen, Germany*

(2) *Fraunhofer Institute for Production Technology IPT, Aachen, Germany*

Modern clad material systems for battery, charging and thermal management challenges in automotive electrification

Frehn, A.; Greschner, U. (1)

Clad materials have already found their way into many different markets and products, they are widely used in aviation, aerospace, machinery, medical treatment, food, civil, automotive and other fields [1, 2].

The combination of different properties of the core and cover materials play a decisive role here. For example, this process can be used to combine strength values, stiffness values, corrosion resistances or conductivities of a wide variety of materials in order to be able to achieve the requirements of the resulting component. Fig. 1 shows an overview of the different process variants, with rolling of different material partners with a subsequent annealing being the most frequently used process type.

As a result of measures to reduce CO₂ emissions, electromobility is not only on the rise for passenger cars, but is now also being discussed for other types of mobility. In these process chains (from energy generation through storage to the consumer), whether in battery applications or hydrogen propulsion, clad solutions can help with complex material problems where special property combinations are required. This publication is intended to show examples of some developments in clad materials that are either already being used in series production in electromobility applications or are already being tested in components. The main focus will be on material combinations based on copper, since this material will be the core topic of this conference.

Challenges to Cu-Al compounds

In many cases, joining different materials with different property combinations is the main challenge in the production of multi-material connec-

tions. In case of welding or brazing processes, the joining of dissimilar material combinations implies many challenges such as the formation of an intermetallic seam, microcrack formation, contact corrosion and ensuring a sufficient wettability. In case of aluminium and copper, one of the most important material compounds, the welding is limited due to a confined solubility and the difference in melting temperature (Al: 660°C, Cu: 1083°C), thermal conductivity, thermal capacity and coefficient of thermal expansion [3]. Additionally, the high reflectivity of copper, the thermally stable oxide layer of aluminium and in particular the formation of different intermetallic phases

must be considered here, which cause a drastic decrease of the mechanical strength due to their significant brittleness. Fig. 2 shows the associated phase diagram and the resulting phases [4]. Compared to conventional fusion welding, modern welding technologies such as laser or electron beam welding allow an exact control of the stirring of the base metals and a reduction of the energy input and hence reduce both the size of the intermetallic phase as well as the amount of residual stresses and distortion (e.g. [5-7]). Nevertheless, the intermetallic phase could not yet be completely averted by the many optimisation processes documented in literature. Several new technologies and strategies such as Laser Beam Welding (LBW) using highly dynamic beam deflection, Friction Stir Welding (FSW), Laser Induction Roll Plating (LIRP) and Electromagnetic Pulse Welding

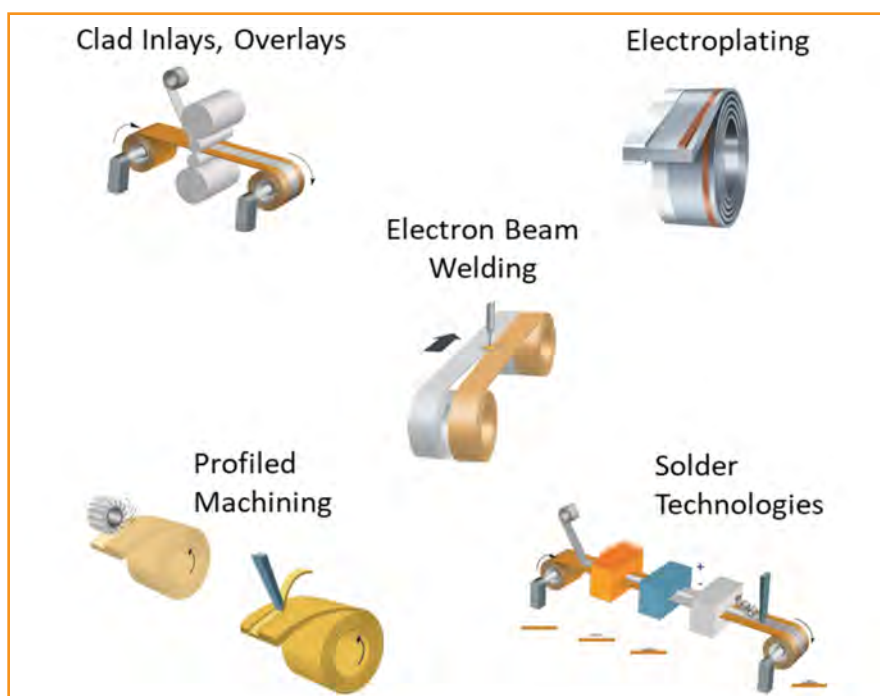


Fig. 1: Variety of cladding processes

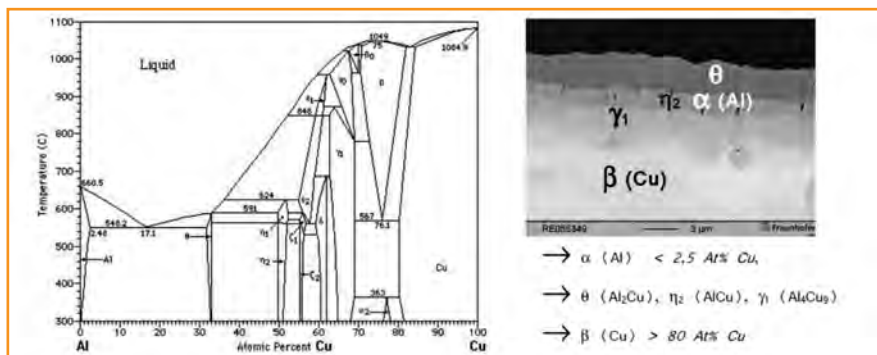


Fig. 2: Al-Cu phase diagram and resulting phases [4]

(EMPW) are under development to further advance the efforts in joining aluminium and copper. In addition, the existence of joining defects must always be taken into account for welded or brazed joints, which are often to be minimized by precise control of the welding parameters or by downstream inspection processes. In some applications, such welding defects cannot be tolerated, so that bolted connections are often still used, although these require higher process efforts, usually also have a higher weight and lead to a higher cost.

Solution based on clad materials

Cu-Al-overlay clad and eStainless

Fig. 1 also shows the overlay cladding process. This has been used for years to produce either the Cu-Al or the compound with two overlays (Cu-Al-Cu). The process basically consists of 2 steps:

Step 1 - A Single 75% Roll Reduction, with which a 4X new surface area at the Interface is created. Furthermore, this process step breaks apart respec-

tively disperses oxide layers creating new atomic scale contact between the two metals.

energy to drive diffusion and alloying between the two layers. After the green bond is heat treated, the metal strip is then processed using traditional methods like further rolling, annealing, slitting, forming, etc.). The process is nowadays technical standard and various suppliers produce this type of clad material. By optimizing the process, over 10 billion automotive Cu-Al lead frames have been produced and during the last 30 years "on the road" no field failures were reported.

This standard process and clad alloy provides excellent conductivity prop-

eStainless® Grade	Electrical Conductivity (%IACS)	X-Y Thermal Conductivity (W/m*K)	Z-Thermal Conductivity (W/m*K)	Bending Modulus (GPa)			
eStainless 300	73%	290	57	162			
eStainless 240	60%	240	38	177			
eStainless 200	50%	200	31	184			
MECHANICAL PROPERTIES¹							
Grade	Temper	SUS Hardness	Bending Yield Strength	0.2% Offset Yield Strength	Ultimate Tensile Strength	Elongation	90° Bend Formability (Longitudinal)
eStainless 300 15/70/15 ²	H0	180-240 HV	292-462 MPa	135 MPa	290 MPa	17%	<0.5
	H1	240-300 HV	462-632 MPa	-	-	-	-
	H2	290-350 HV	604-774 MPa	370 MPa	400 MPa	6%	<1.0
	H3	320 HV min.	689 MPa min.	400 MPa	430 MPa	2%	-
eStainless 240 20/60/20 ²	H0	180-240 HV	322-511 MPa	200 MPa	400 MPa	22%	<0.5
	H1	240-300 HV	511-699 MPa	-	-	-	-
	H2	290-350 HV	667-856 MPa	433 MPa	490 MPa	8%	<1.0
	H3	320 HV min.	761 MPa min.	-	-	-	<2.0
eStainless 200 25/50/25 ²	H0	180-240 HV	342-542 MPa	260 MPa	461 MPa	25%	<0.5
	H1	240-300 HV	542-742 MPa	350 MPa	510 MPa	22%	<0.5
	H2	290-350 HV	708-908 MPa	510 MPa	590 MPa	11%	<1.0
	H3	320 HV min.	808 MPa min.	560 MPa	620 MPa	4%	<1.25

Fig. 3: Different eStainless grades and resulting properties

Step 2 – Heat treatment at low temperatures of the strip which supplies

erties combined with weight savings due to the Al content. However, this material does not offer high strength or stiffness, so another clad material was developed based on this combination. Here, the copper was combined with a stainless steel and is named eStainless® Clad accordingly. Due to the high strength and stiffness of the stainless steel as the covering material, up to 80% of the strength or stiffness of the stainless steel can be achieved in this clad material. Additionally, the copper core significantly improves thermal and electrical conductivity. Fig. 3 shows the different material grades and the corresponding mechanical and physical properties. The different grades result from

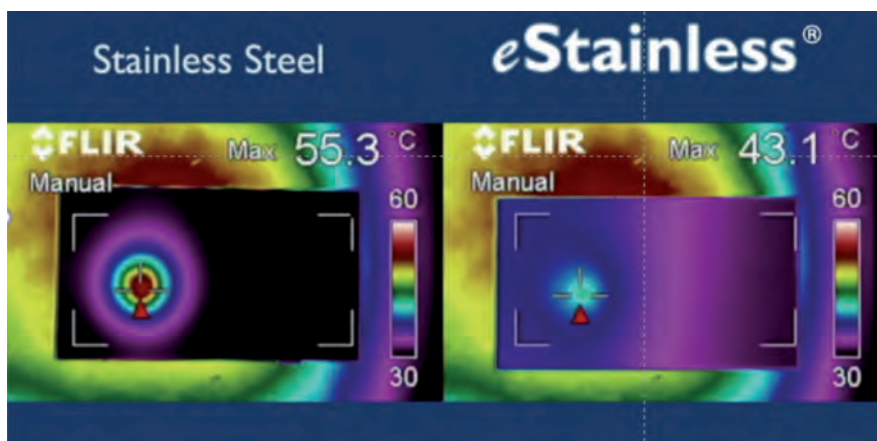


Fig. 4: FLIR Comparative Test: Stainless Steel versus eStainless® Clad, after 40s heating time



Fig. 5: Initial clad design (left) and resulting Dovetail (right), cross sections

the different material thicknesses of the individual materials, so that the properties can be set very flexibly. The advantages in thermal conductivity have been investigated in various studies. For example, in the so-called FLIR test, which visualizes heat dissipation during spot heating. Fig. 4 shows the results of a stainless steel compared with the eStainless solution after approximately 40s of heating. It can be seen that as a result of the better thermal conductivity, the heat is very well dissipated into the environment and (unlike the stainless steel) no hot (=heat) spot remains. In addition, the maximum temperature reached during spot heating is over 10°C lower. This material can therefore be an option where high strength or stiffness is required on the one hand, and good heat dissipation on the other. For example, the focus is on components in batteries, where the use of these materials could prevent overheating during charging.

Dovetail

For battery production, or more precisely for intercell connections, the materials described above are not suitable. What is desired here is a clad material that is not connected over the entire surface but, similar to a butt weld connection, has a clear material separation over the length. The aim is to create a clean material transition to the battery anode or cathode and also to avoid the disadvantages of the appropriate joining processes described above. The goal was therefore side-by-side cladding, and various geometries of the single-material coils had been investigated in the past. It became clear that a considerable number of joint geometries showed problems in mechanical strength. The so-called single angle geometry required extremely wide joints for even a marginal performance and was therefore not pursued. Instead, a multiple connec-

tion was developed that was named Dovetail because of its appearance. Fig. 5 shows the described initial cross-section geometries and the resulting development of Dovetail. In the manufacturing process, the

failure took place in the area of the Aluminium material. Especially in intercell connections, the fatigue strength, particularly in the connection zone, is of considerable importance, since this determines the service life of the battery and joining errors should therefore be avoided. These tests were also carried out, see Fig. 6. In these tests under cyclic loading, also no failure could be detected in the area of the joint zone. Again, the failure occurred in the aluminum

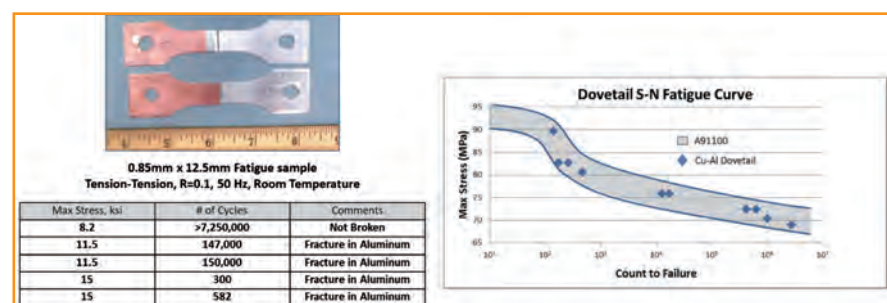


Fig. 6: Results from fatigue tests and comparison with Al-alloy

coils of both materials, i.e. Aluminium and Copper, are machined at the edges using a modified machining process. After that the edges are cleaned again and then joined together by applying the above described clad process. As with the other clad materials, rolling is followed by annealing at low temperatures to ensure the metallic bonding of the individual materials.

area. So it is not really surprising that the results in the form of a Wöhler curve were in the range of the aluminum material.

As with the eStainless material described above, FLIR tests were performed and the obtained results were compared with laser-welded Al-Cu specimens. Fig. 7 shows the corresponding comparison. For the Dovetail material, especially at shorter

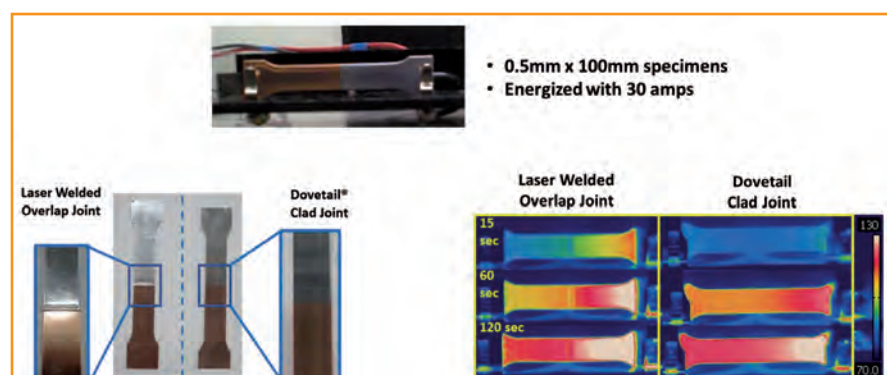


Fig. 7: FLIR Comparative Test: Laser welded samples versus Dovetail

During the development process, this material was studied and characterized in detail. The main focus was laid on the properties of the joint area. In quasi-static tensile tests, no failure could be determined in the joint zone;

heating times, a significantly more homogeneous temperature distribution over the specimen is shown than for the laser-welded joint. Only at longer heating times the thermographic images converge.

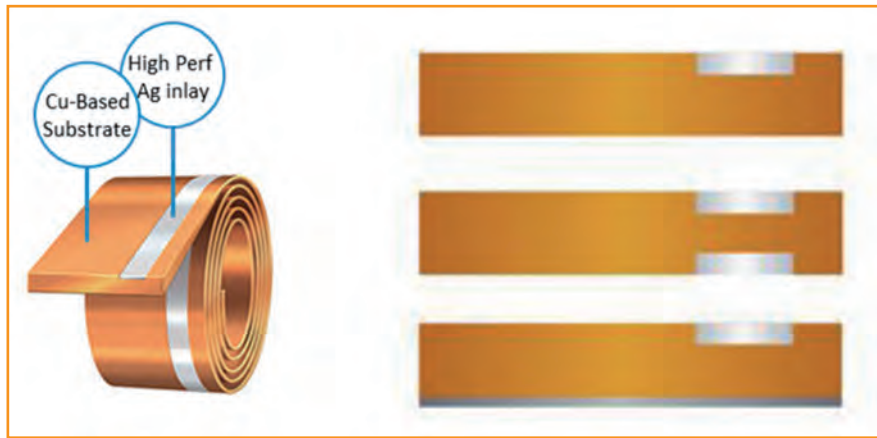


Fig. 8: iON EV concept (left) and different variants (right)

As already described, the Dovetail material is an interesting alternative to bolted connections in battery modules, with busbars and lead tabs being the main focus here.

ION EV

The last example of clad materials in the electromobility environment is in the area of charging infrastructure for e-vehicles. Compared to the materials presented so far, in this application not only the conductivity is of interest, but also the properties wear resistance and insertion force. Transferred to the charging connectors for e-vehicles, these properties are expected to result in a higher number of cycles and thus a longer service life, as well as in a higher power density.

The basis of this clad material combination with the designation iON EV is a copper base alloy with an inlay cladding of a Silver alloy. The Copper alloy can be selected from the usual commercially available alloys. The Silver alloys, on the other hand, are proprietary developments and can be modified according to the requirements profile. The hardness ranges between 140 and 170 HV, depending on the chemical composition and the production process. Also variable is the inlay cladding, which can be precisely adjusted and produced in terms of position, width and thickness. If additional stiffness is required, the material can be provided with a top layer of stainless steel on the reverse side. Fig. 8 schematically shows the concept and possible variants.

The material combination results in a coefficient of friction of lower than $0,20\mu\text{m}$, which reduces the insertion force of the component by up to a factor of 7. This contributes to the low wear of the charging connector in the component life. Fig. 9 shows a comparison of the wear rates from the typical "Block on Ring" test for iON EV

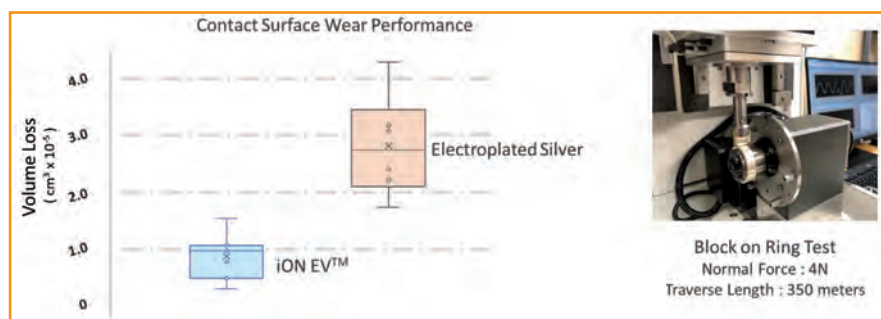


Fig. 9: Results from wear performance tests in comparison with electroplated silver

compared to a Silver coating that was electroplated. In these tests, the wear rate of the clad material was up to 10 times lower than that of the coated material.

Summary and outlook

These presented application examples show the advantages of clad materials, which can be flexibly designed depending on the application and profile. On the one hand, this flexibility can be achieved by the various process routes, and on the other hand, different materials can be combined. These examples also show the importance of copper in this group of materials, especially when electrical or thermal conductivity is a requirement which

is the case in many electromobility applications. Copper thus forms the basis here and is further improved by other metals when (as in the case of eStainless) higher strength respectively stiffness or (as in the case of iON EV) a better wear resistance is required. Other material solutions are currently being under development, not only in the field of electromobility, and the presented alloys are further optimized. Additionally, the range of dimensions will be expanded to include larger widths.

References

- [1] J. X. Xie, C. J. Wu, X.F. Liu, X. H. Liu: A novel forming process of copper cladding aluminum composite materials with core-filling continuous casting, Materials Science Forum 539-543 (2007): 956-961
- [2] S. Xiong, Z. Shang, H. Gao, Q. Zhai: Rolling-Cladding Technology for Cu-Al Thin Sheet, IOP Conf. Series: Materials Science and Engineering 677 (2019)
- [3] F.-W. Bach, L. Engelbrecht, K. Lau, Hochleistungsfügetechniken für

- Hybridstrukturen, Fügen von Stahl-Aluminium-Mischverbindungen, in: M. Geiger, R.F. Singer (Hrsg.), Tagungsband zum Industriekolloquium 2006 des SFB 396 (2006), 109-119
- [4] J. Kaspar, M. Zimmermann, A. Ostwaldt, G. Goebel, J. Standfuß, B. Brenner: Challenges in joining aluminium with copper for applications in electromobility, Materials Science Forum Vols. 783-786 (2014) pp 1747-1752
- [5] Z. Sun, R. Karppi: Electron beam welding of dissimilar metals, VTT, Research Notes, Technical Research Centre of Finland (1994) 1544
- [6] M. Krätzsch, J. Standfuß, A. Klotzbach, J. Kaspar, B. Brenner, E. Beyer: LBW with highfrequency beam oszillation: Welding of dissimilar materials with brilliant fibre lasers, Phys. Proc. 12 (2011), 142-149
- [7] [4] U. Reisgen, S. Olschok, J. Holk, O. Odehnal, N. Wagner: Untersuchungen zum strahlschweißtechnischen Fügen von artfremden metallischen Werkstoffkombinationen; Schweißen und Schneiden 61 (2009), 182-190

(1) Dr. A. Frehn; U. Greschner, Materion Brush GmbH, Stuttgart, Germany

Wettability of Copper on Industrial Filter Materials

Gumban, C. G. (1); Hubálková, J. (1); Fankhänel, B. (2); Charitos, A. (2); Aneziris, C. G. (1); Voigt, C. (1)

The interfacial interactions between molten copper and ceramics is of great significance in metallurgical processes such as copper melting, refining, and casting. Copper-ceramic contact can be found in the refining furnace, casting troughs, launder and, in the gating system containing ceramic filters. Copper foundries have started using ceramic foam filters for melt flow control and impurities removal, which substantially contribute to the improvement of melt and cast quality. The wetting behavior between the metal and the ceramic filter influences the filtration efficiency. Presently, there are limited studies on the wetting properties and chemical interactions between the commercially available filter materials in contact with copper. The novelty and growing importance of the subject necessitates further research. This study investigates the wetting behavior of copper on commercially available filter materials using sessile drop test. Aside from contact angle measurement, the chemical interactions between copper and the filter materials will be characterized using scanning electron microscopy (SEM) and energy dispersive X-ray spectroscopy (EDX).

In the foundry, refractory materials are used as launder and furnace lining, crucible and rammed material, die inserts and melt filters [1,2,3]. The production of a high-quality copper cast is dependent on many parameters such as the selection of the suitable ceramic material. A good understanding of the casting principles, supported by an overview of the pre-casting melt treatment is indispensable in order to avoid defects and optimize the process in general. Among the most common casting defects in copper and copper-based alloys attributable to the melt quality and fluid mechanics are gas porosity, inclusion defects, mold penetration, sweating and formation of oxide films [4,5]. They are detrimental to the cast quality as they induce a significant decrease in mechanical strength, conductivity, machinability, corrosion and wear resistance [4,6]. Melt treatment procedures like gas purging, fluxing, vacuum treatment and, melt filtration can prevent these defects. Utilization of ceramic foams filters results in the reduction of melt turbulence and non-metallic inclusions [7, 8]. Although melt filtration is used in copper foundries [9,10,11], there is a lack of detailed information on the process.

Ceramic foam filter material selection is based on process conditions, thermo-mechanical properties and cost issue of the filter material. Metal and metal alloys with higher casting temperatures (e.g. iron and steel) also require filter materials with superior thermo-mechanical properties like zirconia (ZrO_2) and carbon bonded alumina (Al_2O_3-C).

Chemical interactions and wetting behavior also constitute an essential criterion when selecting the filter material. The ceramic material should have little to no reaction with the alloy at the given casting parameters. The wetting behavior between the metal and the ceramic filter material also has an influence on melt filtration i.e. in aluminum melt filtration, a higher contact angle leads to higher filtration efficiency [12].

To the authors' knowledge, no literature on the interfacial interactions between the copper melt and the commercial filter materials except for zirconia and silicon carbide was published. Authors [13, 14,15] investigating the wettability of copper on ZrO_2 substrates under vacuum at 1200 °C report a contact angle of 116°, 120° and 140°, while the contact angle of copper on silicon carbide is around 140 ° [16]. The high contact angles ($\theta > 90^\circ$) denotes poor wetting [17].

For the investigation of the wetting behavior between copper melt and filter materials, the sessile drop test is a practical method. In this study, the conventional sessile drop technique was used. The copper was placed directly on the ceramic substrate with the same material chemistry as commercially available filters. The assembly was heated in a furnace at a designated temperature. During heating and holding time, the drop shape was recorded allowing the characterization of the wetting properties.

After cooling the copper/ceramic filter material system was examined with the help of SEM and EDX to obtain information about the interactions between the copper and the filter material.

The aim of this study is to characterize the wetting properties and chemical interactions between the copper melt and commercially available ceramic filter materials as a preliminary investigation on the effects of these interfacial interactions on copper melt filtration.

Materials and methods

Preparation of copper and substrates

The copper used for this study is oxygen free copper. Its purity was determined with spark spectrometry using the Thermo Fisher ARL 4460 OES Metals Analyzer and melt extraction by carrier gas process using the G8 Galileo CS/ONH. For the sessile drop experiments, the copper was cut into small cubic pieces with masses equal to 100 ± 50 mg. The metal surface was cleaned using a glass fiber brush.

Six different commercially available ceramic filter materials were investigated: zirconia (ZrO_2), zirconia toughened alumina, ($Al_2O_3-ZrO_2$), phosphate bonded alumina (Al_2O_3-P), silicate bonded alumina (Al_2O_3 -



Fig. 1: SEM micrographs of copper on Al_2O_3 substrates at 1180°C for 30 minutes under a) air b) argon c) vacuum

Si), silicon carbide (SiC) and, carbon bonded alumina (Al_2O_3 -C). The sessile drop technique requires flat and plane substrates. For the first five materials, the slurries used for the production of the ceramic foam filters were dried and ground up into powder. The powders were then uniaxially pressed with 60 MPa pressure to form substrates with a diameter of 12 mm and a height of 3 mm. The substrates were sintered under the same conditions as the ceramic foams filter in the industrial production. The carbon bonded alumina material was cast by the supplier to round substrates with a diameter of around 50 mm and coked under the same parameters as the Al_2O_3 -C filters. In order to fit into the sessile drop apparatus, the Al_2O_3 -C substrates were broken. Moreover, tablets composed of pure alumina were also made as reference material. Prior to the experiments, all substrates were polished and dried. Afterwards, the surface roughness was measured with a laser scanning microscope, VK-X 1000 (Keyence, Japan), whereby an area of $6 \times 2 \text{ mm}^2$ in the center of the substrate was evaluated at 20x magnification. The determination of the surface roughness, S_a , was conducted on processed areas whereby a cut-off wavelength λ_c of 0.8 was used. Each substrate type was scanned at least 5 times.

Sessile Drop Test Procedure

The sessile drop tests were conducted in a closed tube furnace manufactured by Gero GmbH (Neuhausen, Germany) at the Institute of Nonferrous Metallurgy and Purest Materials (TU Bergakademie Freiberg, Germany). The furnace is connected to a vacuum pump and an argon gas inlet. Images were taken at set intervals with a camera running on a digital analyzer

software. The software is used for the measurement of the height (h) and the base diameter (d) in order to calculate the contact angle [17]:

$$\theta_{\text{cal}} = 2 \tan^{-1}(2hd^{-1}) \quad (1)$$

Prior to the investigation of the interactions between copper and the filter materials, the influence of the atmosphere was investigated whereby copper on alumina substrates were tested under air, argon and vacuum atmospheres at 1180°C holding temperature. In the next step, the copper and the substrates made of different filter materials were examined under vacuum. The metal/ceramic filter material system was heated to 1180°C under a starting vacuum pressure of 1.8×10^{-5} mbar. The pressure during holding time was $p < 1.4 \times 10^{-5}$ mbar. The set temperature of 1180°C was maintained for 30 minutes. At the end of the holding time, the contact angle was measured. A minimum of two trials per ceramic material was conducted.

Results and Discussion

Influence of the atmosphere

Fig. 1 shows SEM images of the $\text{Cu}/\text{Al}_2\text{O}_3$ couple under different atmospheres. There is a significant difference between the contact angles in air compared to the other two atmospheres. The contact angle of around 5° denotes good wetting behaviour for the $\text{Cu}/\text{Al}_2\text{O}_3$ system in air. According to literature, sessile drop experiments with copper under varying oxygen partial pressures conclude that an increase in oxygen partial pressure results in a lower contact angle [18,19] explained by the formation of copper oxide which then reacts with alumina to form CuAlO_2 [20,21]. Eustathopoulos et al. [22] presented some studies

[18,20,21] which collectively agree on the inverse relation between oxygen partial pressure and, liquid-vapor (σ_{LV}) and solid-liquid surface energies (σ_{SL}) i.e. an increase in $p\text{O}_2$ results to a decrease in both surface tensions. According to the Young-Dupre equation (equation 2), lowering either σ_{LV} or σ_{SL} yields a lower contact angle.

$$\theta_{\text{cal}} = \cos^{-1}((\sigma_{\text{SV}} - \sigma_{\text{SL}})/(\sigma_{\text{LV}})) \quad (2)$$

EDX analysis of the $\text{Cu}/\text{Al}_2\text{O}_3$ system melted under air in this study revealed the newly formed structure composed of copper, oxygen and aluminium.

Both vacuum and argon atmospheres hinder oxygen from coming into the system preventing the reaction described above [20]. Contact angles for $\text{Cu}/\text{Al}_2\text{O}_3$ systems are available in literature but cannot be directly compared as there are some differences i.e. in substrates preparation and roughness, temperature, and partial oxygen pressure during the sessile drop test. Nonetheless, all postulate that at temperatures up to 1200°C , copper does not wet alumina under an inert atmosphere [22, 23, 24]. The interaction between copper and alumina will only be of a physical manner. The contact angle of around 121° under argon atmosphere and the contact angle of 151° under vacuum for the $\text{Cu}/\text{Al}_2\text{O}_3$ couple in this study suggest poor wettability and is in line with the published data [17]. The difference between the two could be attributed to the fact that oxygen may still be present in technical grade argon. Additionally, evacuation and argon purging conducted for the argon experiments may not have completely prevented entry of oxygen completely. This can result to the same interfacial reaction described above [20].

Filter Materials	Surface Roughness S_a (μm)	Contact angle ($^\circ$)	
		Trial 1	Trial 2
ZrO_2	6.6 ± 1.5	113	115
$\text{Al}_2\text{O}_3\text{-ZrO}_2$	2.8 ± 1.2	139	140
$\text{Al}_2\text{O}_3\text{-P}$	4.6 ± 0.8	156	150
$\text{Al}_2\text{O}_3\text{-Si}$	5.9 ± 2.2	153	151
SiC	7.8 ± 1.3	-	-
$\text{Al}_2\text{O}_3\text{-C}$	21.8 ± 4.3	136	137
Al_2O_3 reference	1.8 ± 0.2	152	151

Table 1: Surface roughness of the ceramic substrates and contact angle of copper on the different filter material after 30 minutes at 1180°C under vacuum pressure = 1.8×10^{-5} mbar

Investigation of interactions between filter materials and copper

Table 1 shows the measured surface roughness and the contact angles. The substrate roughness is relatively low with values $< 8 \mu\text{m}$. The $\text{Al}_2\text{O}_3\text{-C}$ substrate roughness $21.8 \mu\text{m}$ was an exception. This was due to the large porosity of the material – as polishing of this material opens more pores. The close contact angle values resulting from the two trials for each copper/ceramic pair shows good repeatability. For the SiC substrate, no contact angles are given due to the roll off of the droplet from the substrates. In order to obtain a Cu/SiC couple, the SiC substrate was grinded to produce a shallow depression. In this way, the droplet could

not roll off the SiC substrate surface. However, the resulting contact angle cannot be determined as the substrate depression prevented an accurate measurement of the height and base diameter. All the measured contact angles are greater than 90° , indicating poor wetting behavior between copper and the commercially available filter materials. There are significant differences in the contact angles between the different filter materials ranging from 114° (ZrO_2), 136° ($\text{Al}_2\text{O}_3\text{-C}$), 140° ($\text{Al}_2\text{O}_3\text{-ZrO}_2$) and $> 150^\circ$ for alumina containing filter materials. The contact angle for the Cu/ ZrO_2 in this study is comparable to those found in literature [13,14]. However, it should be noted that the other sessile drop tests

[13,14] were done at 1200°C using CaO-stabilized zirconia. This study, on the other hand used 1180°C as holding temperature and a different stabilizer for zirconia.

The SEM investigations of the samples after sessile drop experiments are presented in Figure 2 and 3. Conducted EDX analysis of the interface between ceramic and copper did not show interactions.

Studies [16, 25] on copper and SiC at 1100°C under vacuum have shown poor wettability of copper on silicon carbide. Gnesin et al [25] determined an initial wetting angle of around 140° which decreased with time due to a formation of an interfacial layer that was later revealed to be a solid solution of copper and silicon as determined from spectral and chemical analyses. In this study however, no kind of interaction was detected between the copper and the silicon carbide substrate.

The contact angle between copper and carbon ranges from $139\text{-}145^\circ$ under vacuum at temperatures close to the melting temperature of copper [1,26]. This may help explain the poor wetting behavior between copper and the carbon bonded alumina substrate. The lower contact angle of 137° between the Cu/ $\text{Al}_2\text{O}_3\text{-C}$ system compared to the Cu/oxidic alumina containing materials system determined in the study is surprising as carbon containing materials are characterized

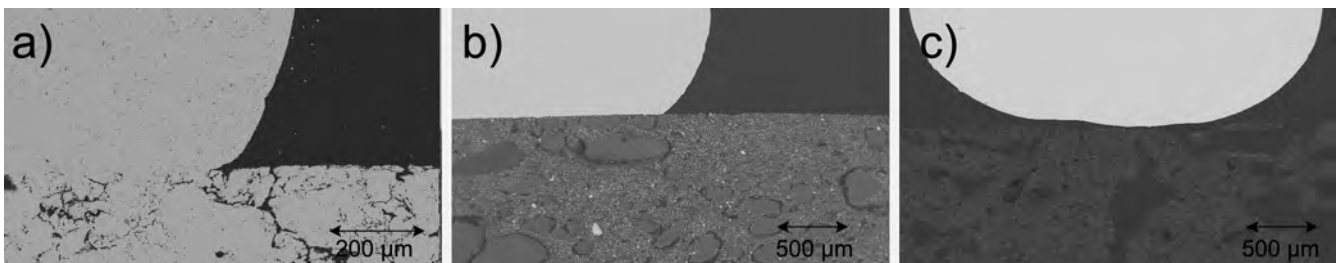


Fig. 2: SEM micrographs of Cu on a) ZrO_2 b) $\text{Al}_2\text{O}_3\text{-ZrO}_2$ c) $\text{Al}_2\text{O}_3\text{-C}$

as having the highest contact angles

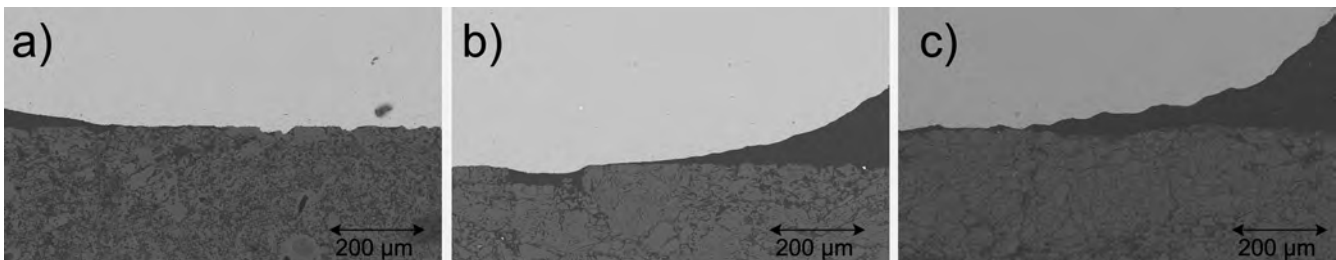


Fig. 3: SEM micrographs of Cu on a) $\text{Al}_2\text{O}_3\text{-Si}$ b) $\text{Al}_2\text{O}_3\text{-P}$ c) SiC

with non-reactive metals such as copper [22, 26].

Conclusion

In all the copper/ceramic filter materials systems investigated, the contact angles $> 90^\circ$ between the copper and the different filter materials indicate poor wetting. Further study and characterization are necessary to explain the significant differences in the contact angles of the different Cu/ceramic filter material systems.

Acknowledgements

The authors would like to thank the Federal Ministry of Education and Research (BMBF) for supporting these investigations as part of the Junior Research Group PurCo (Project-ID 03XP0420). The authors would also like to acknowledge the support of colleagues from INEMET (Thomas Kraft, Ralf Dost and Janine Finger-Kaden) and the IKFVW (Gert Schmidt, Carolin Ludewig, Ricardo Fricke, Rico Kaulfürst and Madlen Müller).

References

- [1] R. Wilson, "Graphite and Refractory Ceramics Used in Continuous Casting," in A Practical Approach to Continuous Casting of Copper-Based Alloys and Precious Metals, Lonon, IOM Communications Limited, 2000, pp. 73-90.
- [2] M. Schlesinger, "Refractories for Copper Production," Mineral Processing and Extractive Metallurgy Review: An International Journal, vol. 16, no. 2, pp. 125-131, 2008.
- [3] I. Khader, A. Renz, A. Kailer and D. Haas, "Thermal and Corrosion Properties of Silicon Nitride for Copper Die Casting," Journal of the European Ceramic Society, no. 33, p. 593, 2013.
- [4] D. Neff, Casting Defects Handbook-Copper and Copper Based Alloys, Schaumburg: American Foundry Society, 2010.
- [5] McGraw-Hill Education, "Defects Typical on Copper Castings," Access Engineering, 2020.
- [6] X. Zhao, Y. Qi, J. Wang, Z. Zhang, J. Zhu, L. Quan and D. He, "Effect of Cast Defects on the Corrosion Behavior and Mechanism of UNS C95810 Alloy in Artificial Seawater," Materials, vol. 13, pp. 1-2, 2020.
- [7] C. Voigt, F. Beate, E. Jäckel, C. Aneziris, M. Stelter and J. Hubálková, "Effect of the Filter Surface Chemistry on the Filtration of Aluminum," Metallurgical and Materials Transactions B, p. 1066, 2015.
- [8] Vesuvius , "Filtration for Copper Alloy Castings," Foseco International Limited, Staffordshire, 2019.
- [9] B. Kamath, R. Adiga, L. Sharma and S. Gupta, "Productivity Improvements at Continuous Casting Rod Plant of Sterlite CopperatSilvassa," in Copper 2003-Cobre 2003, Vol. 1: Plenary lectures, economics and applications of copper, Montreal, 2003.
- [10] B. Friedrich and C. Kräutlein, "Melt Treatment of Copper and Aluminum-The Complex Step Before Casting," in Continuous Casting: Proceedings of the International Conference on Continuous Casting of Non-Ferrous Metals, 2005.
- [11] A. L. Matthews, "Filters Help Eliminate Dross in Copper-base Alloy Castings," Modern Castings (American Foundry Society), 1995.
- [12] C. Voigt, L. Ditscherlein, E. Werzner, T. Ziemert, R. Nowak, U. Peuker, N. Sobczak and C. Aneziris, "Influence of the Wetting Behaviour on the Aluminum Mel Filtration," Light Metals, pp. 1071-1079, 2019.
- [13] M. Ueki, M. Naka and I. Okamoto, "Wettability of Some Metals Against Zirconia Ceramics," Journal of Materials Science Letters, vol. 5, pp. 1261-1262, 1986.
- [14] P. Nikolopoulos and D. Sotiropoulou, "Wettability Between Zirconia Ceramics and the Liquid Metals Copper, Nickel and Cobalt," Journal of Materials Science Letters volume , vol. 6, pp. 1429-1430, 1987.
- [15] K. Nakashima, H. Matsumoto and K. Mori, "Effect of Additional Elements Ni and Cr on Wetting Characteristics of liquid Cu on Zirconia Ceramics," Acta Materialia, vol. 48, no. 18-19, pp. 4677-1681, 2000.
- [16] S. M. Ordoñez, L. Olivares, F. Castro and J. Marin, "Wetting of Silicon Carbide by Copper Alloys," Journal of Material Science, pp. 416-418, 2003.
- [17] N. Eustathopoulos, M. Nicholas and B. Drevet, "Methods of Measuring Wettability Parameters," in Wettability at High Temperatures, New York, Pergamon Materials Series, 1999, p. 117.
- [18] P. Ownby and J. Liu, "Surface Energy of Liquid Copper and Its Wetting Behavior on Sapphire Substrates," Journal on Adhesion Science and Technology, vol. 2, p. 255, 1988.
- [19] M. Nicholas, "Ceramic-Metal Interfaces," in Surfaces and Interfaces of Ceramic Material, Dodrecht/Boston/London, Kluwer Academic Publishers, 1989, p. 403.
- [20] A. Chaklader, A. Armstrong and S. Misra, "Interface Reactions Between Metals and Ceramics: IV, Wetting of Sapphire by Liquid Copper-Oxygen Alloys," Journal of the American Ceramic Society, vol. 51, no. 11, pp. 630-633, 1968.
- [21] V. Ghetta, J. Fouletier and D. Chatain, "Oxygen adsorption isotherms at the surfaces of liquid Cu and Ausingle bondCu alloys and their interfaces with Al₂O₃ detected by wetting experiments," Acta Materialia, vol. 44, no. 5, pp. 1927-1936, 1996.
- [22] N. Eustathopoulos, M. Nicholas and B. Drevet, "Wetting Properties of Metal/Oxide Systems," in Wettability at High Temperatures, New York, Pergamon Materials Series, 1999, p. 225.
- [23] J. Zhang, R. Chandel and H. Seow, "A Study of Chromium on Wettability of Liquid Copper on Alumina Ceramics," International Journal of Modern Physics B, vol. 16, no. 1, pp. 50-56, 2002.
- [24] V. Ghetta and D. Chatain, "Morphologies Adopted by Al₂O₃ Single-Crystal Surfaces in Contact with Cu Droplets," Journal of the American Ceramic Society, vol. 85, no. 4, pp. 961-964, 2004.
- [25] G. Gnesin and Y. V. Naidich, "Contact Reaction of Silicon Carbide with Fused Copper," Soviet Powder Metallurgy and Metal Ceramics, vol. 8, pp. 128-132, 1969.
- [26] N. Eustathopoulos, M. Nicholas and B. Drevet, "Wetting Properties of Metal/Carbon Systems," in Wettability at High Temperatures, New York, Pergamon Materials Series, 1999, p. 320.
- [27] S. Amicone, Radivojević, P. S. Quinn and B. Christoph, "Pyrotechnological connections? Re-investigating the Link Between Pottery Firing Technology and the Origins of Metallurgy in the Vinča Culture, Serbia," Journal of Archaeological Science, p. 16, 2020.
- [28] Haworth Castings, "What are inclusions?" Exprometh Technologies Group, Hampshire, 2018.
- [29] P. Wenschot, "Defects Caused by Precipitation in Liquid Copper-Nickel-Aluminium-Bronze alloys Dissolved Carbon and Removal by Treatment of Melt," International Journal of Cast Metals Research , vol. 24, no. 2, p. 72, 2014.
- [30] N. Eustathopoulos and L. Coudurier, "Influence of Alloying Elements on Wettability and Adhesion Energy in Liquid Metal-Ceramic System," Journal of Adhesion Science and Technology, vol. 6, no. 9, pp. 1011-1022, 1992.
- [31] A. Durov, Y. Naidich and B. Kostyuk, "Investigation of Interaction of Metal Melts and Zirconia," Journal of Material Science, vol. 40, pp. 2173-2178, 2055.
- [32] Y. Yoshino, "Role of Oxygen in Bonding Copper to Alumina," Journal of the American Ceramic Society, vol. 72, no. 8, p. 1323, 1989.

(1) Gayle Celaida Gumban, Jana Hubálková, Christos G. Aneziris, Claudia Voigt, Technische Universität Bergakademie Freiberg, Institute of Ceramics, Refractories and Composite Materials, Agricolastr. 17, 09599 Freiberg, Germany

(2) Beate Fankhänel, Alexandros Charitos, Technische Universität Bergakademie Freiberg, Institute of Nonferrous Metallurgy and Purest Materials, Leipziger Str. 34, 09599 Freiberg, Germany

Microstructure and crystallographic variations in different positions in OFP copper outer shell of canisters for spent nuclear fuel storage

Hagström, J. (1); Sandström, R. (2); Sarnet, J. (3)

In Sweden and in Finland it is planned to use large canisters, 5 meter high and 25 metric tons weight, with an outer shell of 5 cm copper for final disposal of spent nuclear fuel, Figure 1. The canisters will then be placed in the stable bedrock surrounded by bentonite clay.

The spent nuclear fuel will be dangerous for many thousands of years and the long-term properties are therefore of interest. The copper shell will protect the canisters from leakage and corrosion properties are very important. The shell consists of a hot-worked seamless tube with a lid welded onto the tube. Friction stir welding under protective atmosphere is used. Corrosion rate depends to some extent on the crystallographic plane which is exposed to the corrosive media and information on the crystallographic texture is necessary for corrosion models. Resistance to failure from mechanical forces is also vital and due to long time exposure at elevated temperatures creep properties are important. The material is OFP copper, oxygen free copper with additions of 50 ppm phosphorous

(P). P increases creep ductility in OFP copper [1]. Models for creep that are being developed need high quality information on grain boundary disorientation distribution, especially the fraction of coincident site lattice (CSL) boundaries are of interest since such boundaries often have special properties. The microstructure and physical- and mechanical properties of the copper are determined by the casting and the hot working processes and will vary to some extent in different positions in the canister wall and lid. addition to the long-term properties, the mechanical integrity during handling and the ultrasonic inspectability can be affected by a coarse copper grain structure [5]. The cylinder is extruded in two steps from a copper ingot. The ingot weight is 12 metric tons, and the original coarse grained cast structure

is transformed during hot working at temperatures $>700^{\circ}\text{C}$ to a relatively homogeneous recrystallized microstructure. The lid is forged by pressing (up-setting) a cylinder from a continuously cast billet into the final disc shape. The contains a certain amount of dislocation sub-structure. The two hot-working processes are different in terms of total amounts of strain and stress states. The recrystallized structure can therefore differ between the tube and the lid [6]. This paper describes how the analysis of the grain boundaries was made and the distribution of grain boundaries in the material. Modelling of phosphorus interaction with grain boundaries is discussed because it is a crucial element for the creep strength and ductility of OFP copper. Even minor amounts dramatically reduce the climb rate of dislocations and thereby increase the creep strength.

Experimental work

This work has focused on crystallographic analysis of the copper material in the canister walls and top-sealing lid. Large area EBSD (electron back-scattered diffraction) analysis was used to extract high quality information on grain boundary disorientation distribution with special focus on CSL boundaries. Furthermore, very detailed information on grain size distribution and texture was gathered. Analyses were made over the complete 50 mm wall thickness and the analyses contained well over 70.000 grains each. Ten such large area analyses were made at different positions in the walls from two canisters (8) and in one top-sealing lid (2). The high

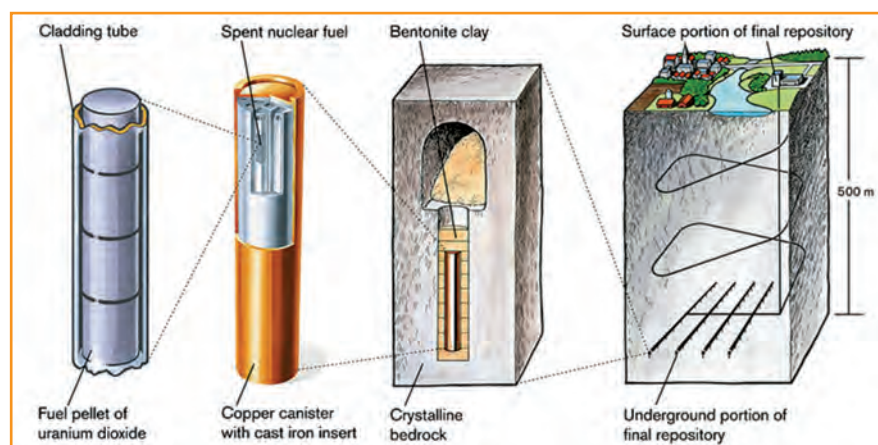


Fig. 1: Description of how the spent nuclear waste will be stored in the Swedish crystalline bedrock

grade of detail in combination with large area made it possible to analyse microstructural differences over the section, through the wall thickness. The different positions and sections were chosen to gather information about the homogeneity of the microstructure in the canister wall and lid. The specimens were cut using Electrical Discharge Machining (EDM) to minimise the mechanical damage of the specimen surface. The surface was then ground with SiC paper finishing with P4000 paper. Electro-polishing was performed using orthophosphoric acid and water (50/50). Electro-polishing effectively removes material leaving deformation free surfaces, however etching was a problem and to get around this problem OP-S polishing was added as a final step. This extra preparation step using OP-S with additions of ammonia and hydrogen

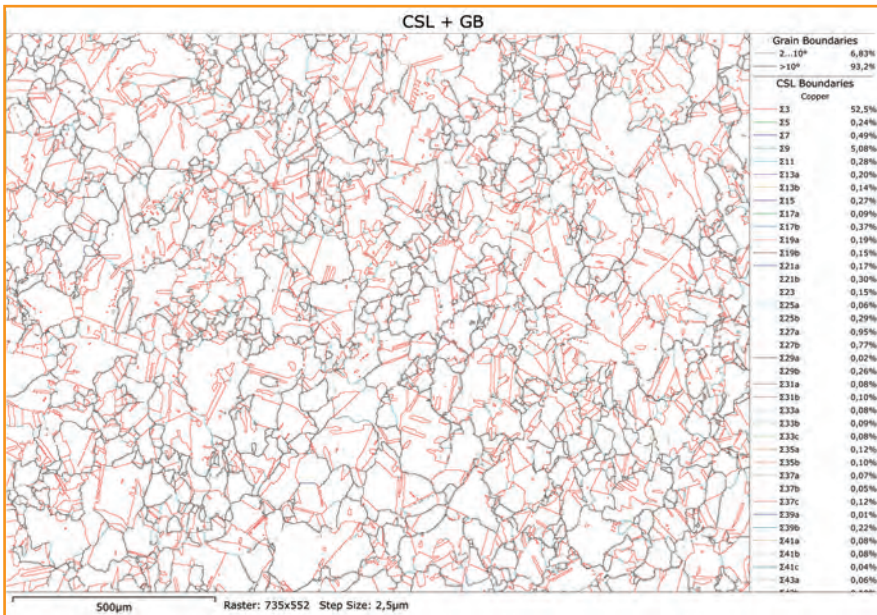


Fig. 2: CSL boundaries in the top sealing lid. The amount of low angle boundaries was 7% and high angle boundaries 93%. A list of the frequency of the 40 first CSL boundaries is given.

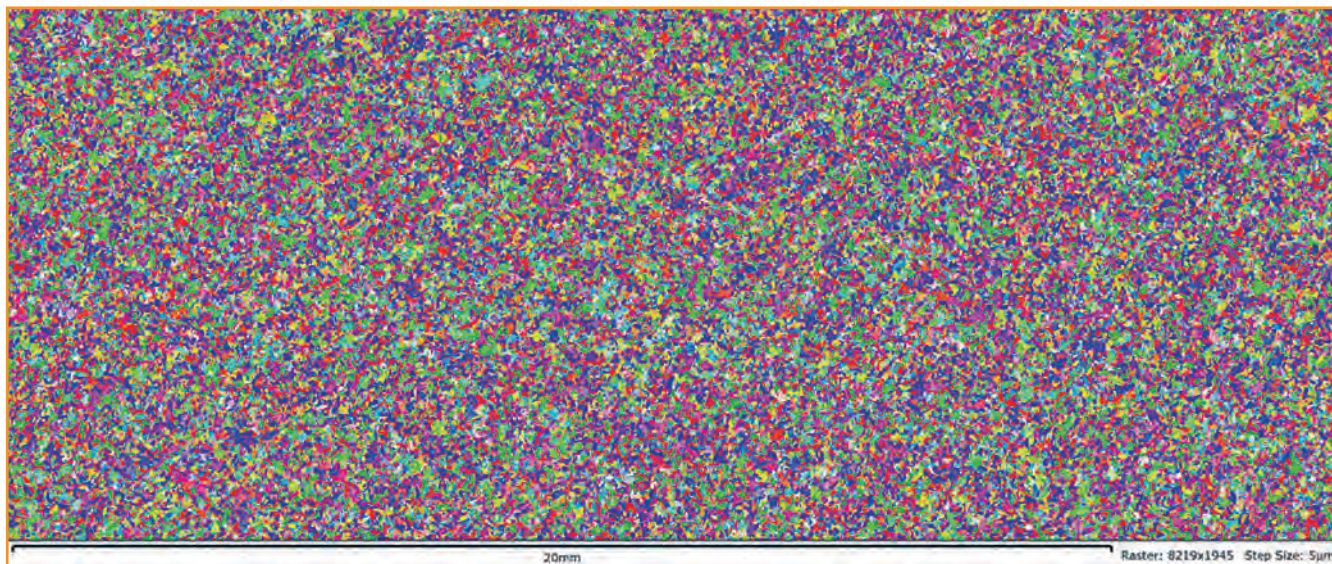


Fig. 3a: Part of a large area EBSD analysis stitched from many individual analyses. The colors show crystal orientations according to the inverse pole figure color code.

peroxide (90 ml OP-S, 6 ml ammonia and 4 ml hydrogen peroxide) successfully improved the surface and the final surface condition showed to be perfect for EBSD.

The EBSD analyses were made using a Zeiss GeminiSEM450 microscope. This microscope can deliver high current combined with a small spot which is important for high speed EBSD analysis. The EBSD detector was an Oxford instrument Symmetry detector which can be run at very high speed, >3000 Hz, but often lower speeds are chosen for improved pattern quality. In this

case very large areas were analysed by combining many individual EBSD maps that automatically were stitched together, typically the analysed area was 45-48 mm vs. 12-15 mm. The step size was 5 µm which resulted in data sets of about 25-30 million points. Running at 2000 Hz one specimen took typically 6 hours effective analysis time in the microscope.

Results

CSL boundaries are frequent in copper and the analysis showed that $\Sigma 3$

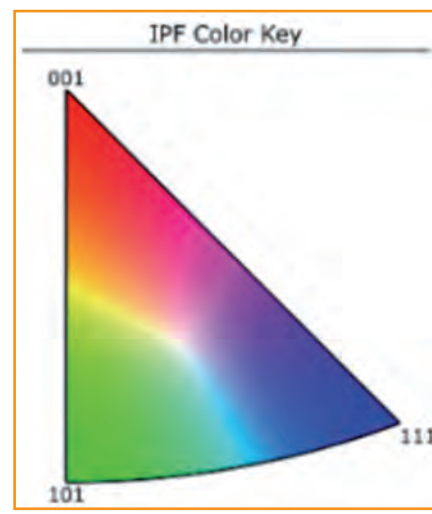


Fig. 3b: IPF crystal orientations color code

CSL boundary	1a. C1 Axial F	1b. C2 Axial F	2. C2 Axial C	3. C2 Tang F	4. C1 Tang C	5. C2 Radial F	6. C1 Radial C	7. C2 Radial F	8. Lid Axial C	9. Lid Tang C
$\Sigma 1$ (LAGB 2-10°)	2,85	2,68	2,96	2,59	2,50	2,90	2,42	4,63	17,0	24,4
$\Sigma 3$ 60,00° <111>	49,78	50,64	51,13	49,86	49,98	51,18	50,20	53,71	51,96	48,53
$\Sigma 5$ 36,87° <100>	0,22	0,21	0,21	0,21	0,22	0,22	0,24	0,20	0,32	0,32
$\Sigma 7$ 38,21° <111>	0,64	0,64	0,64	0,64	0,63	0,63	0,64	0,57	0,45	0,51
$\Sigma 9$ 38,94° <110>	2,59	2,34	2,26	2,33	2,53	2,44	2,64	2,16	5,31	5,03
$\Sigma 11$ 50,48° <110>	0,54	0,53	0,52	0,55	0,55	0,53	0,53	0,56	0,48	0,52

Table 1. CSL boundary fractions in the 10 positions in the canister wall and lid

twin boundaries constituted >50% of the high angle boundaries in the material. An EBSD map showing CSL boundaries is given in Figure 2. Figure 3 show a part of a large area analysis over the complete wall thickness. $\Sigma 3$ boundaries are often related to annealing twins, and they show a 60° rotation around the <111> axis. $\Sigma 9$ boundaries were the second most frequent boundaries and constituted 5% of the high angle boundaries in the canister wall material.

The variation in microstructure was not very big in the canister wall material, but texture and grain size varied to some extent over the wall thickness. The top-sealing lid material was however different to the canister wall material. The lid contained substantial amounts of low angle (dislocation) grain boundaries, which were not present in the canister wall. The grain size was larger and the texture weaker in the lid material compared to the canister wall material. Table 1 presents summarised results from the analysis of CSL boundary fractions up to $\Sigma 11$. CSL fractions up to $\Sigma 49$ was analysed in this work.

Modelling P occupancy in the grain boundaries

It is well documented that the various GB types are associated with different segregation energies for alloying and impurity elements [1, 2]. In this paper the focus will be on phosphorus

because it is a crucial element for the creep strength and ductility of copper. Even minor amounts dramatically reduce the climb rate of dislocations and thereby increase the creep strength. It also strongly enhances the creep ductility that is vital for the

the segregation energy at site i, $\Delta \bar{E}_{PGB}$ is the average segregation energy, k is Boltzmann's constant and T the absolute temperature. From eq. (1), an expression for the average segregation energy can be obtained by formula (2).

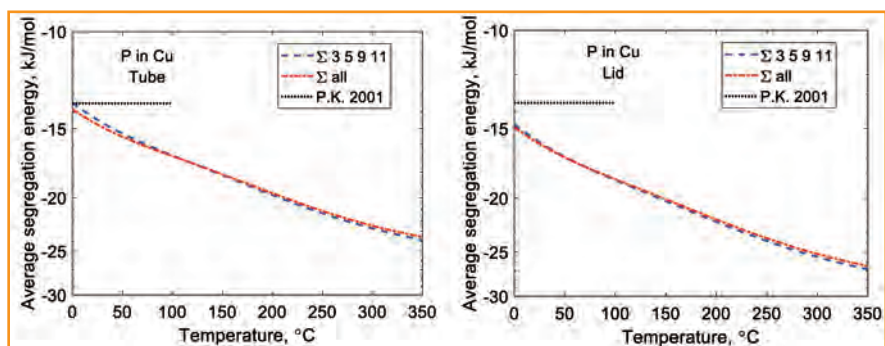


Fig. 4: Average segregation energy for P at GBs in Cu versus temperature according to eq. (2). For the dashed curve only $\Sigma 3$, $\Sigma 5$, $\Sigma 9$ and $\Sigma 11$ were taken into account. For the dashed-dotted curve also other GB types between $\Sigma 7$ and $\Sigma 27$ were included assuming the same segregation energies as for $\Sigma 11$. P.K. 2001 refers to the previously used value [4]; a) canister tube; b) canister lid.

copper canisters for storage of nuclear waste. The segregation energies of P at the GBs is a critical factor for the creep ductility [3].

A model for segregation energies is presented in detail in [1] and only the results are shown here. The fraction of atomic sites x_{PGB} in and around the GBs that are filled by P atoms is given by formula (1).

x_p is the concentration of P in the material expressed in moles, p_i is the frequency of occurrence of the different GB types and sites, $\Delta E_{PGB(i)} < 0$ is

The value used for the P concentration is $x_p = 123$ at. ppm. The values for $\Delta E_{PGB(i)}$ and the frequency factors p_i for the sites are taken from [1] for $\Sigma 5$, $\Sigma 7$ and $\Sigma 11$ and from [2] for $\Sigma 9$. The frequency factors p_i for the GB types are those in Table 1, positions 1 a and 8. In comparison to the previous study [1], there are two major differences. i) $\Sigma 9$ is directly considered. ii) In the previous study data from a published distribution of GB types was used with different appearance compared to Table 1.

The derived average segregation energies are presented in Figure 4 for tube and lid material in the canister. The values are derived in two different ways. In the first case only values for $\Sigma 5$, $\Sigma 7$, $\Sigma 9$ and $\Sigma 11$ are included. In

$$x_{PGB} = x_p \exp(-\Delta \bar{E}_{PGB} / kT) = x_p \sum_i \frac{p_i \exp(-\Delta E_{PGB(i)} / kT)}{1 + x_p \exp(-\Delta E_{PGB(i)} / kT)} \quad (1)$$

$$\Delta \bar{E}_{PGB} = -kT \ln \left(\sum_i \frac{p_i \exp(-\Delta E_{PGB(i)} / kT)}{1 + x_p \exp(-\Delta E_{PGB(i)} / kT)} \right) \quad (2)$$

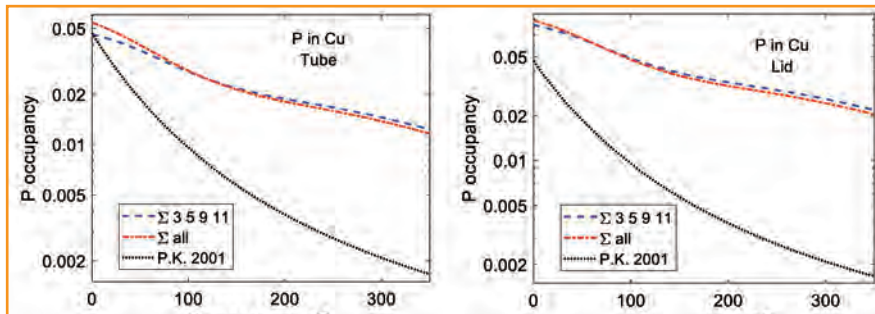


Fig. 5: Computed occupancy of P at GBs in Cu versus temperature according to eq. (1). For the dashed curve only $\Sigma 3$, $\Sigma 5$, $\Sigma 9$ and $\Sigma 11$ were considered. For the dashed-dotted curve also other GB types between $\Sigma 7$ and $\Sigma 27$ were taken into account assuming the same segregation energies as for $\Sigma 11$. P.K. 2001 refers to a previously used value [4].

the second case the influence of the remainder of the GBs is estimated by assuming that they have about the same properties as $\Sigma 11$.

The absolute value of the average segregation energy increases with increasing temperature. The trend is the same for tube and lid material, but the absolute value is slightly higher for the lid material. The lid material has a small amount of cold deformation (2 to 3%). It is known that cold work increases the $\Sigma 9$ fraction of boundaries, Figure 1. The two alternative ways to assess the average segregation energy yield quite similar results. In Figure 5, results for the P occupancy in the GBs are shown.

The P-occupancy decreases with increasing temperature in a simi-

lar way for tube and lid material although the values for the lid are slightly larger due to the higher absolute segregation energies. The two alternative ways of modelling the P occupancy give again about the same results.

That the difference between these two modelling alternatives is considerably smaller than in the previous analysis [1] illustrates the value of including $\Sigma 9$ in the analysis. Before data for individual GBs were available, a constant value for the segregation energy was used [4]. The resulting values are included in Figures 4 and 5. It is evident that the new results give higher absolute segregation energies and P occupancy suggesting that the predicted creep strength and ductil-

ity are even higher than previously modelled.

The difference between the tube and lid material illustrates that microstructure plays an important role for the properties.

References

- [1] R. Sandström, C.M. Lousada, The role of binding energies for phosphorus and sulphur at grain boundaries in copper, *J Nucl Mater*, 544 (2020) 152682.
- [2] C.M. Lousada, P.A. Korzhavyi, Single vacancies at $\Sigma 5$, $\Sigma 9$ and $\Sigma 11$ grain boundaries of copper and the geometrical factors that affect their site preference, *Journal of Physics and Chemistry of Solids*, 169 (2022).
- [3] R. Sandström, R. Wu, J. Hagström, Grain boundary sliding in copper and its relation to cavity formation during creep, *Materials Science and Engineering: A*, 651 (2016) 259–268.
- [4] P.A. Korzhavyi, B. Johansson, A.Y. Lozovoi, A. Alavi, Segregation of 3sp impurities to $S5(310)$ tilt grain boundary in copper, Swedish Nuclear Waste Management Company, TR-01-25, 2001, pp. 32–39.
- [5] M. Jonsson, G. Emilsson, L. Emilsson. Mechanical design analysis for the canister. Posiva SKB Report 04, Posiva Oy, Svensk Kärnbränslehantering AB (2018).
- [6] G. W. Rowe, *Principles of Industrial Metalworking Processes*. London: Edward Arnold (1977).

(1) Joacim Hagström, Swerim AB,

(2) Rolf Sandström, KTH Royal Institute of Technology

(3) Jan Sarnet, SKB AB

Casting properties of lead-free brass

Hagström, J. (1); Nordin, M. (2); Persson, P. E. (3)

Brass is traditionally alloyed with lead to improve machinability and casting properties. However, due to health and environmental hazards, lead is foresight to be banned within the EU during the coming decade. Implementation of existing lead-free alloys is as of today very limited due to higher material and/or production costs. Published research papers on casting related issues with lead-free alloys are few, most research are focused on machining properties. A Swedish national funded project, OPTIBRASS [1], with participation from 13 companies, 1 university and 2 research institutes in Sweden, Norway and Germany has worked with machining and casting issues in the implementation of lead-free brass alloys. It is necessary for the European brass industry to be pro-active and develop systems for lead-free brass through the whole value chain. The project has mainly focused on the downstream processes from material production to final products, which have been identified as major hinders for a wide use of lead-free brass. The work presented here focus on casting related issues.

One study within the OPTIBRASS project focussed on pressure die casting and compared production with standard CB772S (1.1% Pb) and CB771S (0.1% Pb). More than 10.000 components were produced in lead-free brass after an optimisation pro-

It showed to be difficult to produce defect free components with lower lead than 0.54%. For the low lead alloy with 0.30% Pb casting faults occurred, intrusions at positions with thick walls were observed. With the lead-free alloy (0.12% Pb) the casting related issues got worse with larg-

er and more frequent intrusions. To further examine what mechanisms that change during solidification of brass with low lead content the same alloys were cast by gravity casting in a small laboratory mould. This study is presented here. The results showed that the alloy containing 0.54% Pb worked well with similar behaviour and microstructure as the reference material. When the lead content was lower, 0.30% and 0.12%, the grain size became significantly larger and plastic strains occurred in the central parts of the ingot, which could be detected by EBSD, electron back-scattered diffraction.

Experimental work

Gravity casting experiments were conducted using a copper mould, 40 mm times 40 mm base and 50 mm height, sections from the three ingots with different lead content are shown in Figure 1. Strong efforts were made to keep all handling procedures and casting parameters constant, only the lead content changed between the experiments. The ingots were cut along the height and the surface was then ground with SiC paper finishing with P4000 paper. Electro-polishing was performed using orthophosphoric acid and water (50/50). Electro-polishing effectively removes material leaving deformation free surfaces. OP-S polishing was added as a final step to obtain a good surface for micro-analysis. This extra

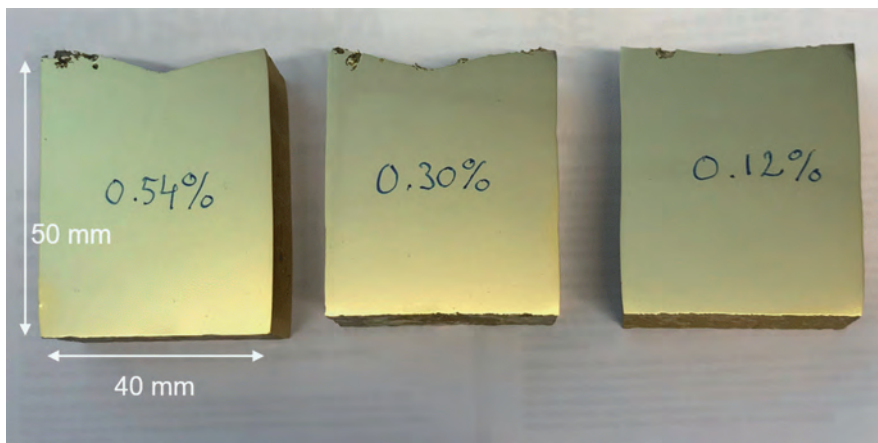


Fig. 1: Test samples

cedure to find the best set of parameters for high quality components. The components were analysed for porosity and surface quality and the obtained results showed that similar production rate and quality could be obtained with the lead-free alloy.

Another study within OPTIBRASS focused on low pressure casting and components were produced with three different lead levels, 0.54%, 0.30% and 0.10%, and standard CB772S as reference (1.04% Pb).

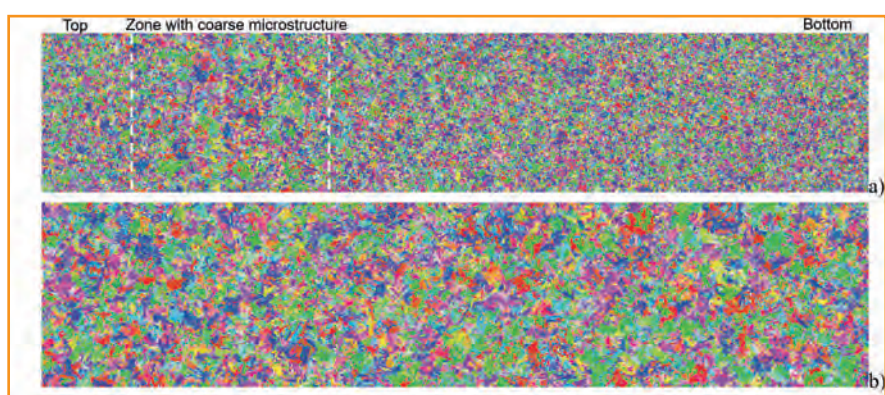


Fig. 2 a, b: Grain structure in the 0.54% lead alloy (a) and in the 0.10% alloy (b)

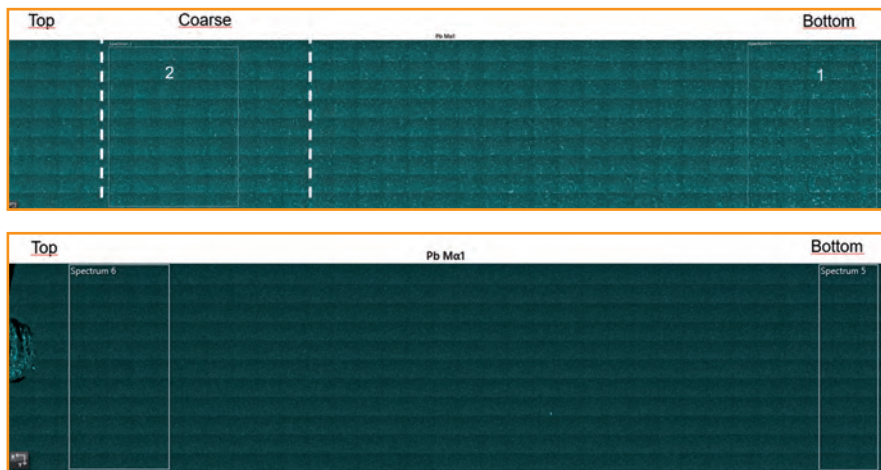


Fig. 3 a, b: EDS analysis over the complete sections. The analysis showed that lead was precipitated as small particles more or less homogeneously over the section. 0.54% Pb (a, top) and 0.10% Pb (b, bottom)

preparation step using OP-S with additions of ammonia and hydrogen peroxide (90 ml OP-S, 6 ml ammonia and 4 ml hydrogen peroxide) successfully improved the surface and the final surface condition showed to be perfect for EBSD. Metallographic analyses with SEM based micro-analysis EBSD and EDS (energy dispersive X-ray spectroscopy) were made using a Zeiss GeminiSEM450 FEG-SEM. The EBSD detector was an Oxford instrument Symmetry detector which can be run at very high speed with maintained angular resolution. The EDS spectrometer was also from Oxford instruments, and it was run in parallel with the EBSD analysis. In this case large areas were analysed by combining many individual EBSD and EDS maps that automatically were stitched together, typically the analysed area was 45 mm times 10 mm. The step size was 5 µm which resulted in data sets of about 20 million points. Running at 1000 Hz one analysis typically lasted 5-6 hours effective analysis time in the microscope. The data was analysed with the AZTEC Crystal software from Oxford Instruments. The mechanisms for the plastic strain was not investigated, but the warmer temperature at solidification could be one factor.

Results

The EBSD analysis showed that the microstructure changed when the lead level decreased, the grain size became larger for the 0.30% Pb and

0.12% Pb alloys compared to the 0.54% alloy. The ingots were analysed from top to bottom with combined EBSD and EDS and the variation of grain size could be seen, Figures 2 a and b show the EBSD analysis over 45 mm ingot height. The 0.54% Pb alloy showed fine grains except for a zone in the centre (a) whereas the 0.12% Pb alloy showed coarse grain size over the complete ingot (b). EDS analysis showed finely dispersed lead particles over the complete section for both alloys, but with higher number density in the 0.54% alloy. Figures 3 a) and b) show the distribution of particles over the complete section from bottom to top and Figures 4 a) and b) analysis at higher resolution. The analysis showed that, in the 0.54% alloy, lead was precipitated as small particles less than 5 µm diameter. The largest particles form patterns that propose they were precipi-

tated from the melt between growing grains/dendrites. The smallest particles were probably precipitated from solid phase. In the 0.12 % alloy the lead particles were fewer and smaller, around 1 µm diameter. In this case the particles were probably precipitated from the solid phase during cooling. Analysis of average lead content in the marked areas at bottom (1) and top (2) in Figures 3 a) and b) showed that the lead content was higher at the bottom compared to the top but the difference was small. In a macro perspective it was concluded that the microstructure and chemistry was homogeneous. Solidification studies that were conducted in the OPTIBRASS project showed that the physical parameters are different to some extent, but fluidity was similar. The solidification experiments showed that lead-free alloys (0.10% Pb) needed shorter time to solidify, and the melt was thus warmer during solidification, compared to a standard CW772S alloy with 1% lead. The interpretation of the experimental results was that the lead in the melt need to be transported away from the solidification front (diffusion in the melt) for the solidification to proceed. The diffusion of lead will be the rate controlling mechanism and slows down the solidification process. As the cooling constantly continues, the under-cooling of the melt will increase. With increased under-cooling the driving force for nucleation increases. This results in a higher nucleation rate and in the end a more fine-grained microstructure. Another theory is that, in brass alloys

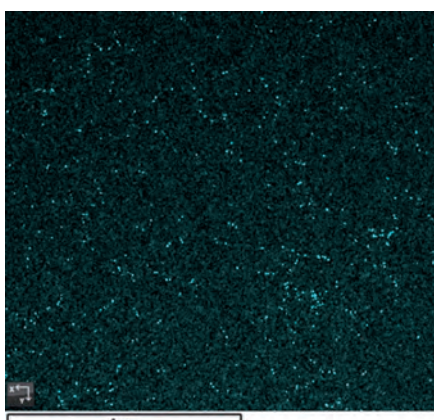


Fig. 4a. EDS analysis showing the lead particles in the 0.54% Pb alloy

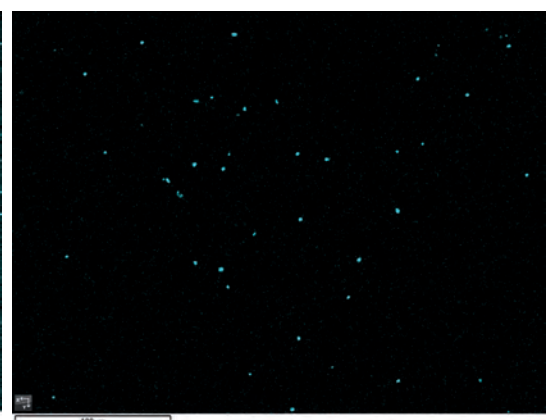


Fig. 4b. EDS analysis showing the lead particles in the 0.10% Pb alloy. Observe the different length scale in the two images.

containing lead, the melt is separated before solidification starts in a monotectic reaction so that one lead rich melt is formed and one without lead. Small liquid lead particles then interact with the solidification and slows down the solidification process. Some experimental observations (not published) support this theory. A set

of rapid solidification experiments is planned to try to verify this mechanism, these results will be published later.

vation programme for Metallic material, Vinnova 2019-02933, march 2022.

References

- [1] Improved lead-free brass products by optimization along the value chain (Opti-Brass), project within The strategic inno-

(1) Joacim Hagström, Swerim AB,

(2) Mats Nordin, FM Mattsson AB

(3) Per-Eric Persson, Nordic Brass Gusum AB

CuSn4Zn2PS – Lead Free Gunmetal for drinking water applications

Haake, M. (1); Hansen, A. (2)

Especially in Europe Gunmetal is a well-known material for drinking water installations. The gunmetal alloy predominantly used has been CuSn5Zn5Pb2 (CC499K) [1]. Indeed this alloy has a significant amount of lead in its composition.

On account of a continuous strengthening of the legislations concerning the heavy metal content in drinking water and consequently in the alloys in contact with drinking water, lead has come under pressure over the last years. In particular, the European Drinking Water directive [2] and the REACH regulations [3] are the main driving forces. Therefore, there had been a great necessity to find and finally develop a copper alloy, which fulfills the necessary future hygienic and toxic aspects whilst at the same time retaining all current material properties. The solution for this challenging task can be CuSn4Zn2PS [4].

This new lead free alloy was developed, based on the gunmetal alloy CuSn5Zn5Pb2. The focus of the new alloy CuSn4Zn2PS was on the ease of manufacturing fittings, suitable for the heating and plumbing industry and of course, on achieving an excellent corrosion resistance. This was realized by substituting lead with sulfur [5].

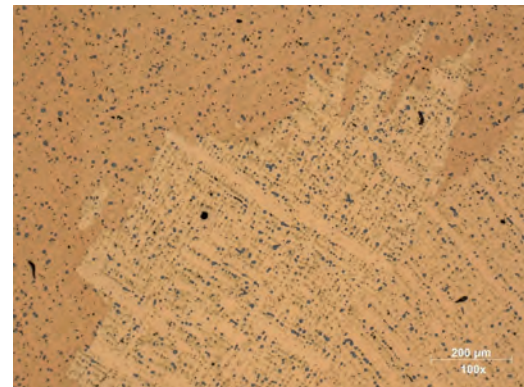
The sulfur forms copper- and zinc-sulfides in the shape of the lead partic-

les, with an amount of sulfur to reach the same volume fraction as with lead. These particles function as chip breakers and no additional phase, which can negatively affect the corrosion properties, is necessary.

This substitution allows an almost identical chemical composition for the main alloy elements like copper, tin and zinc resulting in retaining all the well-known superior properties compared to the old CuSn5Zn5Pb2 alloy. It could be shown, that already well-established production technology can be utilized and the corrosion characteristics have been preserved. In summary, the new developed alloy can be an adequate alternative for the CuSn5Zn5Pb2 in the existing plumbing applications, because all the required properties on the durability of the final parts made from CuSn4Zn2PS can be fulfilled easily.

References

- [1] Deutsches Kupferinstitut (DKI): Kupfer-Zinn- und Kupfer-Zinn-Zink-Gusslegierungen (Zinnbronzen); Published in DKI Informationsdruck; (2004).
- [2] European Parliament: DIRECTIVE (EU) 2020/2184 OF THE EUROPEAN PARLIA-



Microscopic Image of CuSn4Zn2PS

- MENT AND OF THE COUNCIL of 16 December 2020 on the quality of water intended for human consumption (recast); Published by European Parliament, Council of the European Union
- [3] ECHA: Consultation on draft recommendation for inclusion in the Authorisation List; Published by European Chemicals Agency (ECHA); (2018).
- [4] Deutsches Institut für Normung (DIN): DIN SPEC 2701: Unleaded copper alloys — Ingots and castings made of CuSn-4Zn2PS, (2018).
- [5] Hansen, A.: Bleifreier Rotguss als Armaturen- und Installationswerkstoff in der Trinkwasserinstallation; Published in Metall 73, P. 286-289; (2019).

- (1) Martin Haake, REHAU SE & Co. KG, Ytterbium 4, 91056 Erlangen, Germany
- (2) A. Hansen, Gebr. Kemper GmbH + Co KG, Harkotstraße 5, 57462 Olpe, Germany

			Cu	Sn	Zn	Pb	Fe	P	Ni	S
Klassischer Rotguss	CuSn5Zn5Pb2 (DIN EN 1982)	Min.	84,0	4,0	4,0	0,2	-	-	0,1	-
		Max.	88,0	6,0	6,0	3,0	0,30	0,04	0,60	0,04
Bleifreier Rotguss	CuSn4Zn2PS (DIN SPEC 2701)	Min.	90,0	3,0	1,0	-	-	0,01	-	0,20
		Max.	96,0	5,0	3,0	0,10	0,3	0,10	0,3	0,6

Table 1: Comparison of material composition of classic gunmetal to lead-free gunmetal

Efficient processing of copper and its alloys with blue diode laser

Heine, L.-M.; Schlett, M.; Ocylok, S.; Rütering, M. (1)

Laser welding is the manufacturing process of choice for high quality welds realizing complex welding geometries while minimizing the overall heat input. Thereby, diode lasers belong to the most energy-efficient lasers for industrial use and are characterized by a high-power density homogenously distributed over the spot size. However, in the case of copper, these advantages are rarely accessible with conventional infrared lasers as the energy absorption is less than 10 %. Thus, a blue diode laser was specifically developed by Laserline raising the absorption level to almost 70 %.

Starting with 500 W in 2018, increasing the available laser power has been a steady goal. Meanwhile, a power of 3 kW is achieved. One of the most common exercises is welding. But the blue diode laser can also be used for additive manufacturing or large-area heating.

Starting with a technical introduction, it is the paper's purpose to illustrate the broad variety of applications that are now accessible with the blue diode laser. Thereby, practical examples from different markets will be shown and the corresponding optical solutions will be described. At the end, the advantages of the blue diode laser for copper manufacturing will be summarized and a brief outlook to future developments will be given.

Within the last years, we have observed a significant increase in the demand of copper components pushed by e.g. e-mobility, digitalisation or energy transition. These copper components pass through a broad range of production steps. Thereby, copper joints that require mechanical strength as well as electrical conductivity are often welded. Here, laser welding enables complex welding geometries while minimizing the overall heat input due to the high intensity of the laser radiation.

There exist different principles for generating laser radiation, e.g. by light diodes. These so-called diode lasers belong to the most energy-efficient lasers for industrial use. They are characterized by a high-power density homogenously distributed over the spot size. In large part, lasers of this working principle emit laser light in the infrared wavelength spectrum where they originally were designed for.

However, in the case of copper, these advantages are rarely accessible with conventional infrared lasers. Figure 1 illustrates the absorptivity of different

metals at room temperature over the wavelength. Here, the infrared range is highlighted red in between 900 and 1100 nm. As can be seen, the absorption level of Cu-ETP is below 10 %, for CuSn6 it is just slightly higher.

Thus, Laserline started to develop a blue diode laser emitting laser light at

a wavelength of 445 ± 20 nm. The corresponding area is highlighted blue in Figure 1. Here, the absorptivity of Cu-ETP and CuSn6 measures approx. 70 % and is significantly higher than the one of the infrared wavelength. An important advantage when processing copper, as the initial energy injections is facilitated enabling a smooth and well controllable welding process.

Blue diode lasers

The word laser stands for "light amplification by stimulated emission of radiation". This radiation can be emitted in different ways, e.g. by light diodes, also known as single emitter. In case of the diode lasers discussed here, approx. 50 single emitters are necessary to build a bar. Several bars, in turn, build a stack as can be seen in Figure 2. The laser light emitted by this stack is stepwise transformed by optical elements into a "laserline". It is characterized by a specific wavelength and polarisation. This, in return, is

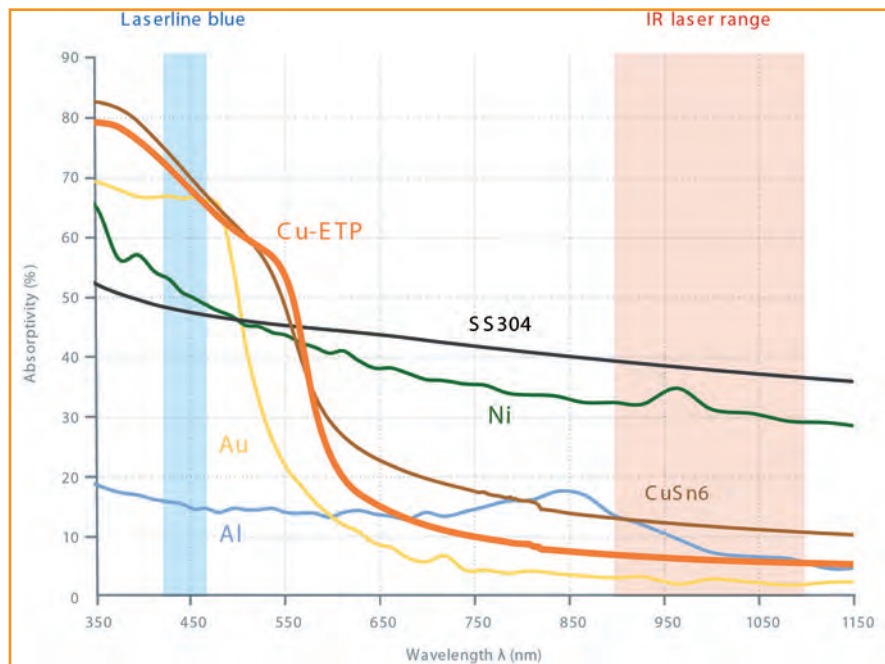


Fig. 1: Absorptivity over wavelength for different metals at room temperature [1, 2]

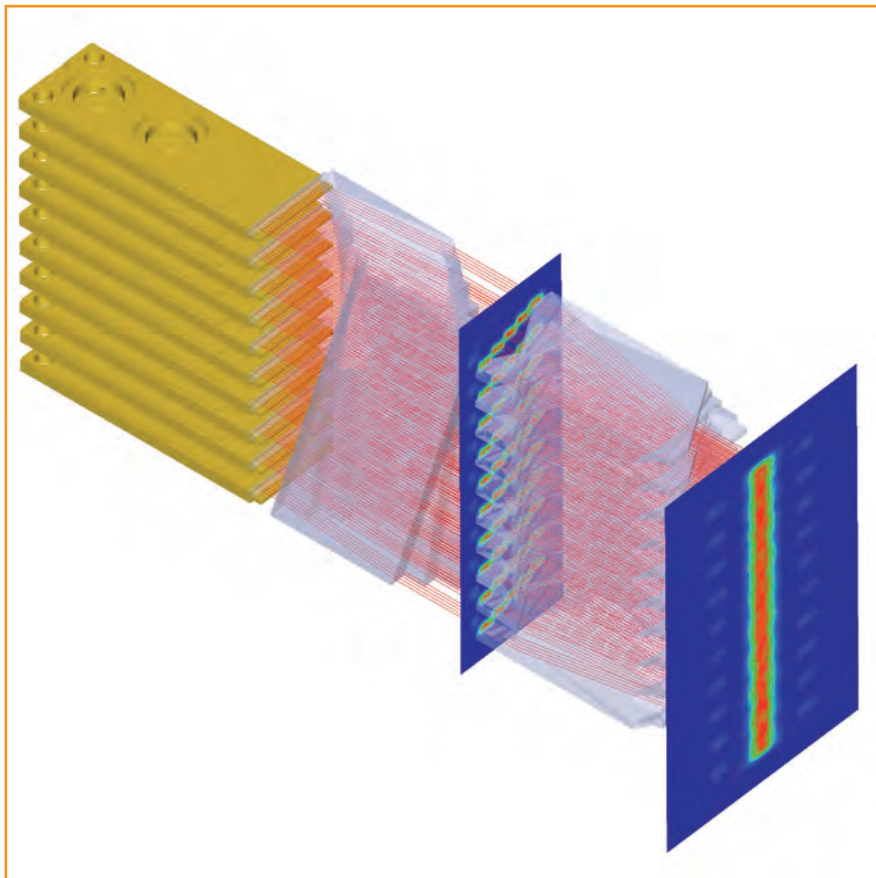


Fig. 2: Arrangement of several bars (yellow blocks on the left) within one stack and transformation of laser light by optical elements into a “laserline”

used to increase the final laser power by combining different polarisations and wavelengths. The resulting beam is shaped by further optical elements and most often transported through a fibre to the final processing optic. This general working principle was developed first for infrared lasers. But in 2018, Laserline launched its first blue diode laser with a power of 0.5 kW emitting at a wavelength of 445 ± 20 nm. Over the last years, increasing the available laser power has been a steady goal: 1.5 kW were achieved in 2019, 2 kW were reached

in 2020. Simultaneously, appropriate optical solutions were introduced, like e.g. different fixed optics or a scanner for remote welding. Here, in the first case, the optic must be attached to a motion system, like a robot, defining the process speed. In the second case, the optic does not have to be moved to cover a certain working area as mirrors within the optic deflect the spot, allowing complex welding geometries and very fast processes of several meters per second. Then, in 2022 a total power of 3 kW was achieved making accessible now an even bro-

ader variety of applications which will be discussed in the following chapter.

Fields of applications

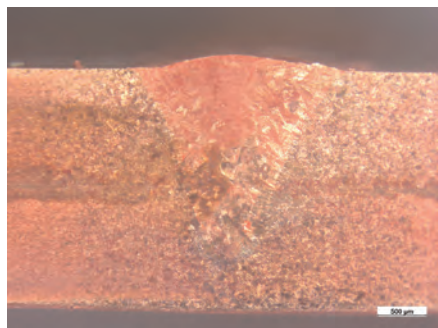
Practical examples of copper that can be processed with a blue laser can be found in numerous markets, e.g. in the field of e-mobility, digitalisation or energy transition. However, in the following, the applications will be grouped according to three processes: welding, additive manufacturing, and brazing/soldering.

Welding

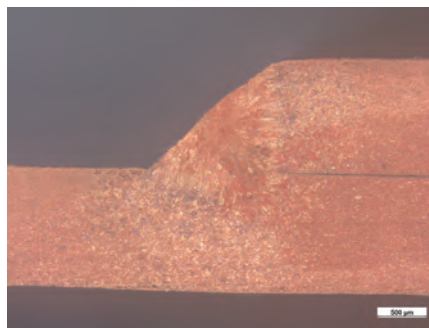
One of the most common exercises for the blue laser is welding. There exist numerous sheet configurations varying in sheet thickness or sheets’ orientation to each other. Figure 3 gives a first impression of different welding configurations that can also include material mixtures, like e.g. copper and steel.

Next to sheet metal, welding of pin configurations is also a common task. However, this application is not limited to hairpin welding. It can also include wire to pin, pin through hole or stranded wire welding. Figure 4 shows another few examples and highlights the robustness of the blue process. Several hairpin configurations are shown before and after welding. Here, an arbitrary spot size – from 0.25 up to 1 mm or higher – allows easily to overcome production tolerances, like gaps, height differences or side mismatches.

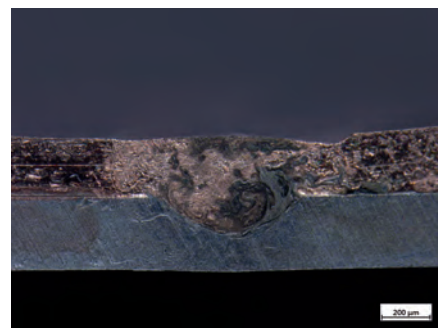
In both cases, the high absorption level of the blue wavelength – for highly reflective materials, like e.g. copper or gold, but also for steel or nickel (see Figure 1) – facilitates the initial energy



Overlap weld (1.2 on 1.2 mm)



Fillet weld (1.2 to 1.2 mm)



Material mixture: 0.2 mm copper on 0.3 mm nickel-plated steel

Fig. 3: Examples for sheet welding – different welding configurations and material mixtures

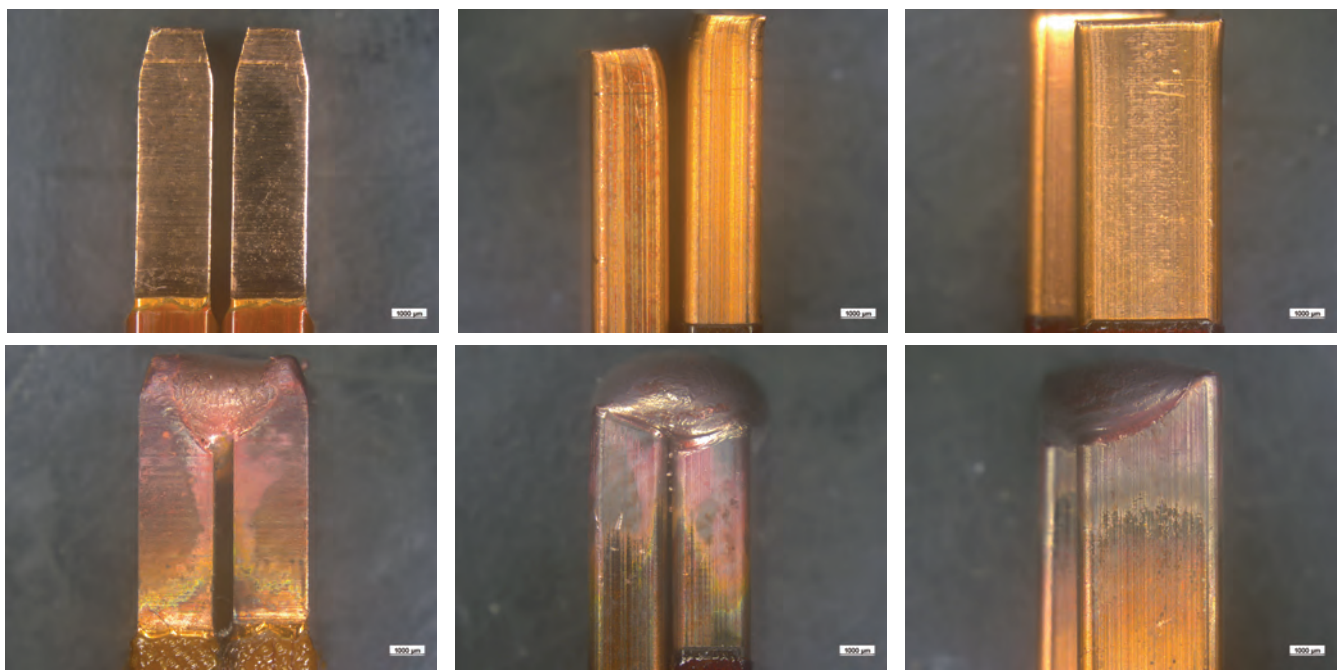
Gap of 600 μm Height difference of $\sim 1 \text{ mm}$ Side mismatch of $\sim 1.5 \text{ mm}$

Fig. 4: Examples for pin-welding – overcoming production tolerances
(top row: before welding, bottom row: after welding, single pin cross-section 10 mm^2)

input and enables an almost spatter-free process. The power of 3 kW allows to manufacture a broad range of cross-sections – from thin to thick: minimizing the overall heat input in case of thin cross-sections and allowing to manufacture thick ones, too. Thereby, the optical setup can easily be adap-

ted to the welding task. The spot size can be chosen according to the requirements, using e.g. a smaller spot to achieve a deeper penetration depth or using a larger spot to compensate production tolerances. Further, a scanner – specifically designed for the blue wavelength – can be used in case of complex welding geometries.

turn, ensures a homogenous warm up of the sample without burning wholes due to local intensity peaks. Further, the spot geometry can individually be adapted to the part's geometry. This is achieved by using Laserline's special homogenizing optics transforming the circular spot to e.g. a rectangular one.

A similar process example is shown in Figure 6, however the operating temperatures are below 450°C in case of soldering. It is a typical task in the area of electronics when parts have to be joined with a PCB. In comparison to brazing, this process is characterized by less power, a shorter process time and often also a smaller spot size. Next to a fixed optic with circular, rectangular or line spot, also a scanner with a circular spot can be chosen as optical solution. Comparable to brazing, solder is usually used to fill gaps, like e.g. tin as demonstrated in Figure 6.

Brazing/soldering

However, the application of the blue laser is not limited to welding tasks. As can be seen in Figure 5, it is also well suitable to join parts successfully by brazing which is defined by a working temperature higher than 450°C. Here, the copper parts warm up efficiently due to the good absorption of the blue wavelength. The heat is then transferred to the solder which subsequently melts down and joins both parts. Thereby, the solder itself can be exposed to laser light, too. The process usually takes a few seconds.

Concerning the optical setup, it is beneficial to use a large spot size in the range of several millimetres. Here, one big advantage of the diode laser is the top-hat profile. This means that there is a homogenous intensity distribution over the whole spot cross section (with square edges at its flanks). This, in

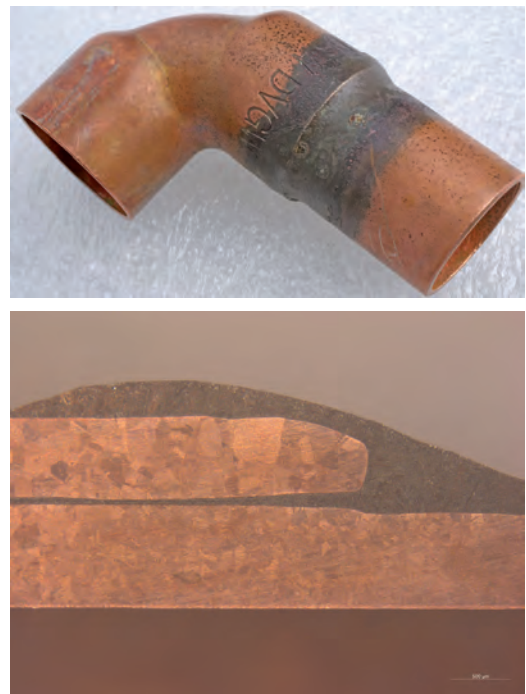


Fig. 5: Brazing of copper tubes with Cu-Ag-P-solder
(top: exemplary sample, bottom: corresponding cross-section)

Additive manufacturing

Furthermore, the blue wavelength becomes more and more attractive for additive manufacturing of e.g. hollow structures or heat conductive laminates, realizing a highly economic use of the valuable copper material. Figure 7 shows an example of such a thin-

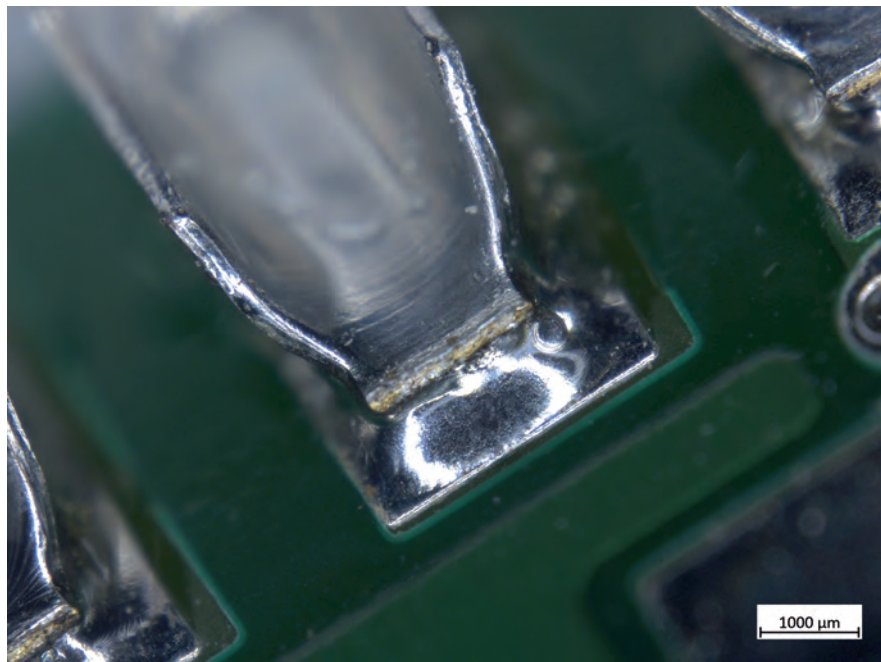


Fig. 6: Example for soldering of electronics with tin-solder

walled hollow structure measuring 70 mm in height, 30 mm in diameter and with a wall-thickness of less than 1.5 mm. Again, the significant higher absorption of the blue wavelength – in comparison to infrared – is beneficial: approx. 5 times larger deposition rates and a powder efficiency above 70 % can be achieved with the blue diode laser. Even for stainless steel as well as nickel and cobalt alloys the process is about 20 % more efficient than with infrared. Further, it is characterized by less energy input and high process stability, so there is no need for power control during the build-up of thin-walled structures to compensate heat accumulation.

Conclusion and outlook

In 2022, Laserline launched its first 3 kW blue diode laser, specifically designed to manufacture efficiently materials that are highly reflective at the

infrared wavelength. This next power level enables an even broader variety of applications for which several examples were given, including welding of sheet metal or pin-configurations, brazing, soldering and additive manufacturing.

One important advantage of the blue wavelength – in comparison to infrared – is the increase in absorptivity measuring e.g. around 60 % for Cu-ETP. This facilitates the initial energy injection, enables a smooth and almost spatter-free process, and significantly increases the process efficiency. The new power level of the blue diode laser allows to manufacture thicker material cross-sections. Further, it enables to speed up processes and to minimize the overall heat input. Thereby, a large range of optical solutions – ranging from scanners over conventional circular spots up to variable rectangular ones – allow an individual adaption to the sample geometry and the welding task.

In future, it will be a steady goal to increase further the available laser power and to enlarge the corresponding optical solutions.

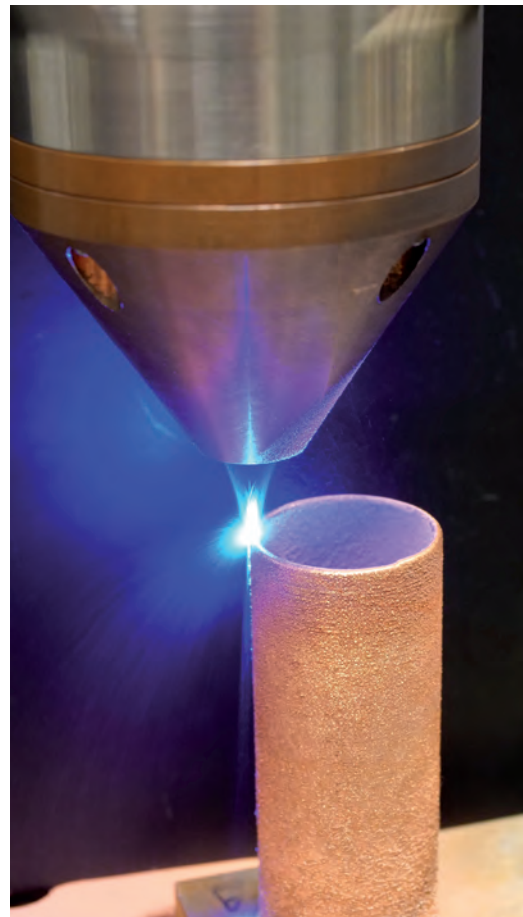


Fig. 7: Additive manufacturing of a 3D-body made of copper powder

References

- [1] Fraunhofer ILT, Hummel et.al. Journal of Adv. J. Proc., 2020
- [2] Nasa, E. Spiesz et al., Nasa Technical Note TN-5353, 1969

(1) Dr. Luisa-Marie Heine, Mathias Schlett, Dr. Sörn Ocylok, Markus Rütering, Laserline GmbH, Fraunhofer-Straße 5, 56218 Mülheim-Kärlich, Germany

Phase Transformations and Kinetic Simulations of Cu-based Alloys

Jansson, Å.; Tang, Y.; Jin, S.; Ghasemi, M.; Lancelot, C. M.; Grundy, N.; Chen, Q.; Bratberg, J. (1)

This paper presents the development and application of thermodynamic and kinetic databases for Cu-based alloys using the so-called CALPHAD (CALculation of PHase Diagram) approach. The thermodynamic database, TCCU, and the atomic mobility database, MOBCU, are developed in a 32-element framework: Cu-Ag-Al-Au-As-B-Be-Bi-C-Ca-Cd-Ce-Co-Cr-Fe-Ge-La-Mg-Mn-Mo-Nb-Ni-O-P-Pb-Pt-Se-Si-Sn-Ti-Zn-Zr. TCCU can be used to predict the phase equilibrium, phase formation, and various thermodynamic properties for Cu-based alloys. Thermophysical properties such as density, thermal expansion coefficient, viscosity of liquid, surface tension of liquid etc. can be calculated as well. By combining TCCU with the mobility database MOBCU, kinetics of diffusion-controlled phase transformations in Cu-based alloys can be simulated. Selected application examples on the kinetic reactions during solidification and subsequent heat treatment processes for typical industrial copper alloys are demonstrated. For example, the non-equilibrium solidification behaviour and micro-segregation during solidification for Cu-Pb-Sn and Cu-Pb-Sn-Zn alloys are investigated using the Diffusion Module (DICTRA) in the Thermo-Calc software package; the nucleation, growth, and coarsening of precipitates in Cu-Ni-Si is studied using the Precipitation Module (TC-PRISMA) in Thermo-Calc.

The usefulness of accurate thermodynamic and kinetic databases for Cu-based alloys need not be stated in the context of these conference proceedings. The established way of producing such databases is by the CALPHAD method (1,2) which is based upon the description of Gibbs free energy and atomic mobility for each phase in a multi-component system as function of temperature, composition and pressure, fitted to real experimental data and supplemented with ab-initio calculations.

In later years the CALPHAD method has been extended to include also properties which cannot be derived from thermodynamics or mobilities alone. For the Copper database these properties are density, thermal expansion coefficient and viscosity and surface tension of the liquid phase.

Various software is necessary for building the databases and especially for calculating results in multicomponent alloy systems and presenting these results in the form of diagrams or tables. For thermodynamic and diffusion calculations the software packages Thermo-Calc (3) and DICTRA (now formally known as Diffu-

sion Module, 3) have been used for decades and are being continuously developed. They are also the software for which the database format was designed. A more recently introduced software package for precipitation simulation, TC-Prisma (now formally known as Precipitation Module, 4), is also used with these databases.

Databases

Our development of copper-based alloy databases has been ongoing for at least eight years, and has resulted in several versions of both thermodynamic and kinetic databases, each version more comprehensive than the previous one.

The latest version of the thermodynamic database, TCCU5 (5) was released earlier this year and contains data for 315 solution and intermetallic phases made up from 32 elements: Cu-Ag-Al-Au-As-B-Be-Bi-C-Ca-Cd-Ce-Co-Cr-Fe-Ge-La-Mg-Mn-Mo-Nb-Ni-O-P-Pb-Pt-Se-Si-Sn-Ti-Zn-Zr

Not all subsystems can be evaluated in detail and included in a database of this size. The CALPHAD method relies on the accepted fact that it allows extrapolation from assessed unary, binary and ternary systems in order to describe higher-order systems with good accuracy. There are 148 binary and 64 ternary systems assessed in TCCU5.

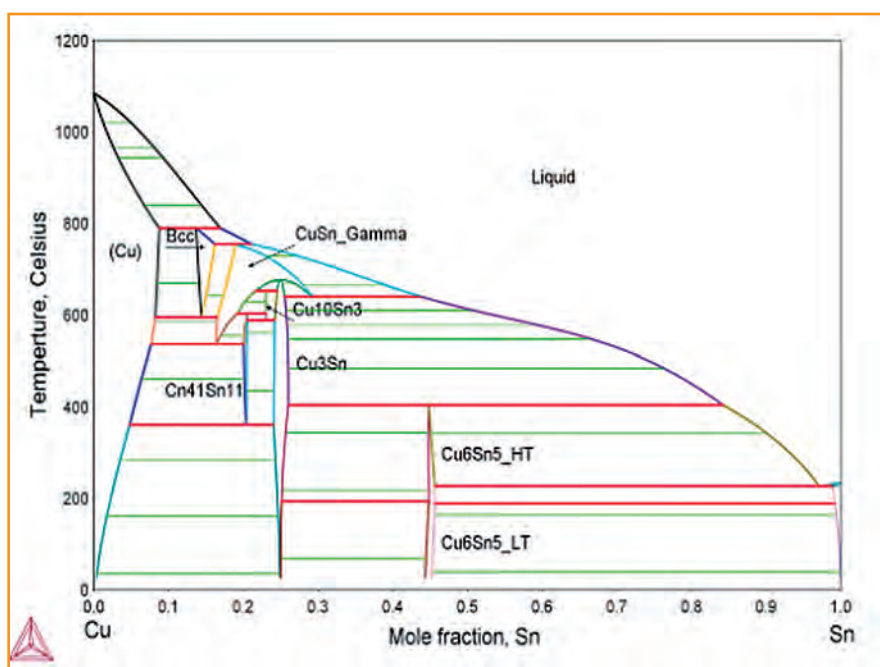


Fig. 1: Calculated binary Cu – Sn Phase Diagram

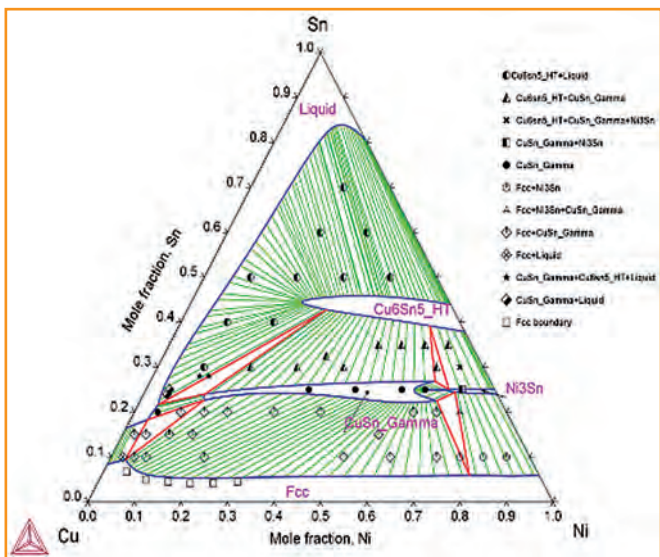


Fig. 2: Calculated isothermal section at 800 °C in Cu - Ni - Sn

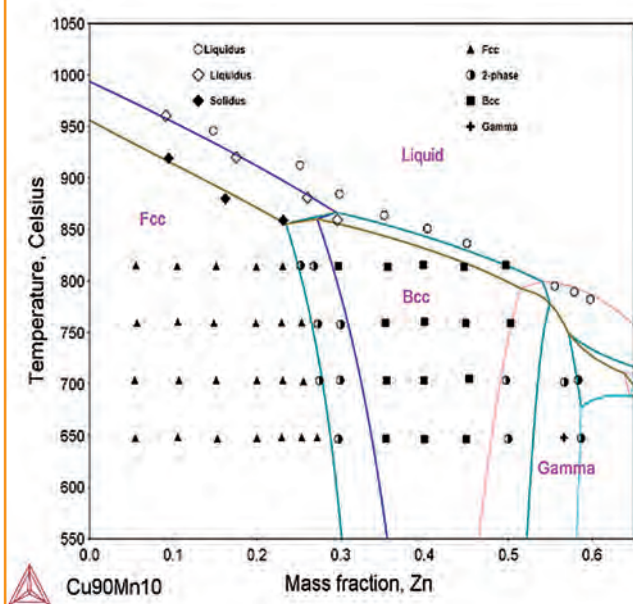


Fig. 3: Calculate vertical section in ternary Cu - Mn - Zn at 10 wt-% Mn

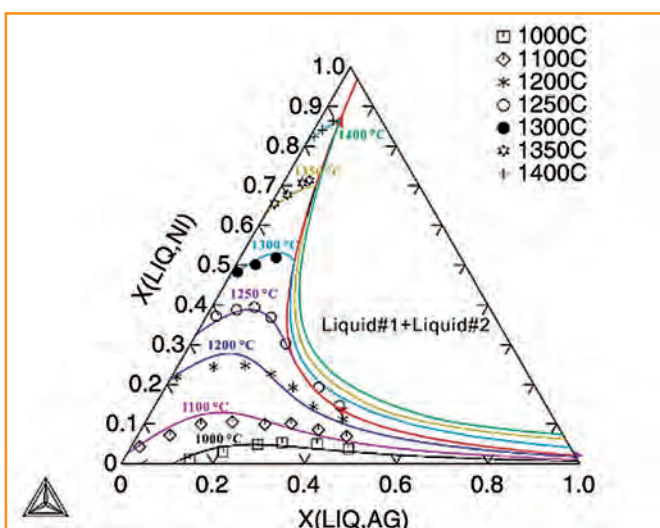


Fig. 4: Calculated Liquidus projection with isotherms in Cu - Ag - Ni

The latest version of the kinetic database, MOBCU5 (6), was also released in 2022 and includes the same 32 elements as TCCU5, but much fewer phases – only the most common matrix phases where diffusion has been studied are included. This is typical for all mobility databases. In MOBCU5 these phases are LIQUID and FCC.

The models used for describing the Gibbs free Energy and Atomic Mobility of the individual phases in these databases come from Compound Energy Formalism (7), which is very much standard for modern CALPHAD databases. Description of these models is outside the scope of this paper. Discussion on how the models were applied to our copper-alloy databases can be found in (8), (9).

Applications

There are numerous applications for the TCCU database and for the combination of TCCU and MOBCU. A few will be shown here in Figs. 1 – 9, in most cases compared with experimental data.

Phase diagrams

One obvious type of calculation is phase diagrams. In Figs. 1 – 4 some recent phase diagram calculations using TCCU5 are shown. Fig. 1 shows the important binary Cu - Sn phase diagram (10). Fig. 2 shows a calculated ternary isothermal section in Cu-Sn-Ni at 800 °C compared with experi-

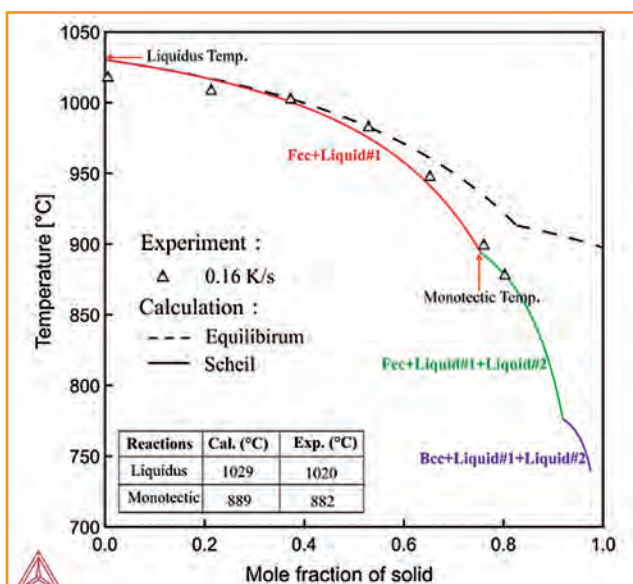


Fig. 5: Calculated Scheil solidification path for Cu - 5.4Sn - 4.7Pb (wt-%)

mental data from (11). The self-consistency of the database ascertains that the Cu-Sn edge of this diagram is consistent with the diagram in fig. 1. In Fig. 3 a calculated vertical section at 10 wt-% Mn in Cu-Fe-Mn showing good agreement with experimental data from (12,13,14) is displayed. Fig. 4 shows a liquidus projection in Cu-Ag-Ni compared with experimental data (15). This diagram is calculated with three axes, but the third (temperature) axis is projected onto the plane of the paper. The diagram also contains 7 more calculations, iso-

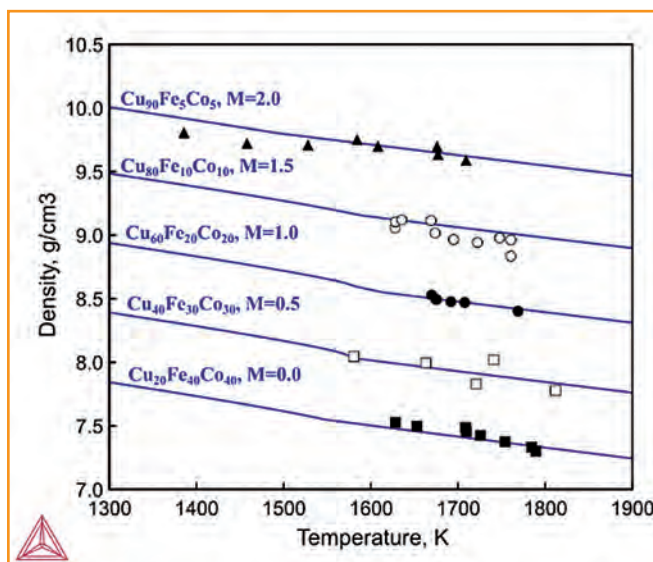


Fig. 6: Calculated Density as function of temperature for 5 different Cu - Fe - Co alloys

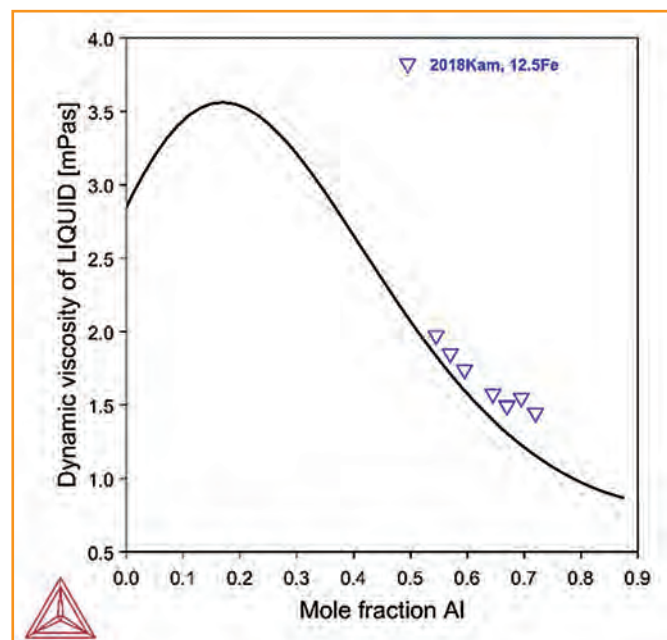


Fig. 7: Calculated viscosity of Liquid in Cu - Al - 12.5 at-% Fe at 1400 °C

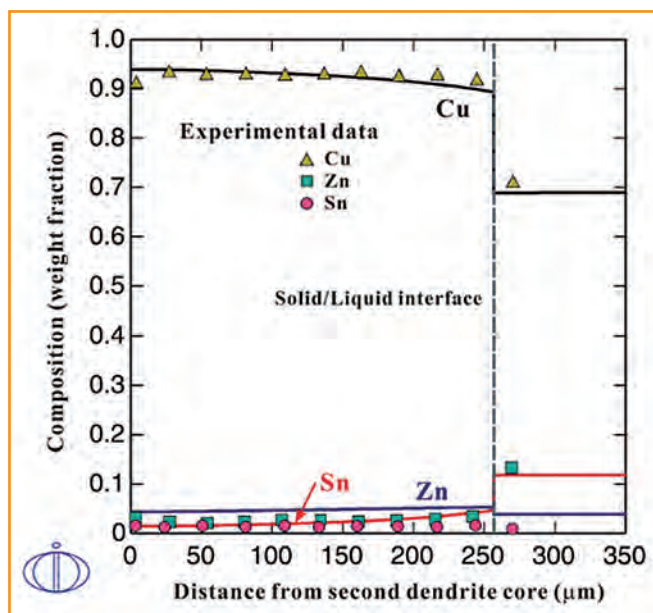


Fig. 8: DICTRA simulation of solidification in Cu - 5.2Sn - 4.9Pb - 4.5Zn (wt-%)

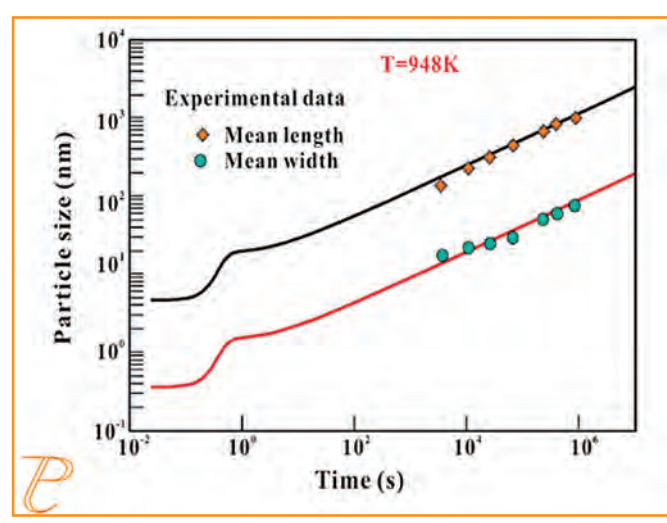


Fig. 9: TC-Prisma simulation of particle growth in Cu - 1.86Ni - 0.45Si (wt-%) at 675 °C

thermal sections at different temperatures. All 8 calculations can be made simultaneously using an automated routine in Thermo-Calc. The agreement with experimental data is very good.

Solidification

The Scheil simulation is not an equilibrium calculation, but one where the solid phases formed are not allowed to change their composition at all during the entire cooling. This often is a much more realistic way of describing solidification behaviour, when compared to for instance continuous cooling

processes, than equilibrium calculation is. The calculated solidification path for an alloy Cu - 5.4Sn - 4.7Pb (wt-%) is shown in Fig. 5 compared with the calculated equilibrium curve (dashed) and experimental data from (16). The Scheil simulation can also predict micro-segregation, but this is instead shown for a different kind of simulation (see Fig. 8).

Property diagrams

Description of molar volume for all phases plus viscosity and surface tension for the Liquid phase is included as an addition to the Gibbs free energy

functions in the TCCU5 database. This allows for calculation of density in Fig. 6 and Viscosity in Fig. 7. Fig. 6 shows the calculated density as function of temperature for 5 different compositions in the Cu-Fe-Co ternary system. Note that each curve has been shifted (added with) a constant "M" in order to separate them in the diagram. The curves would otherwise be very similar and hide each other.

Fig. 7 shows the calculated viscosity of Liquid Cu - Al - 12.5 at-% Fe at 1400°C as function of the Al content compared with experimental data from (18), showing reasonable agreement.

Diffusion and Precipitation Calculations

These calculations require the combination of thermodynamic and mobility data, in this case both TCCU5 and MOBCU5. Fig. 8 shows the result of a solidification simulation using DICTRA for an alloy similar to the alloy in Fig. 5, but in this case quaternary Cu - 5.2Sn - 4.9Pb - 4.5Zn (wt-%). A moderate cooling rate of 0.16 °C/s was used and the diagram shows the result before end of solidification, the composition profile through half a dendrite arm is shown in Fig. 8 compared with experimental data from (16).

TC-Prisma was used to obtain the calculation presented in Fig. 9 which shows the growth of particles in a Cu - 1.86Ni - 0.45Si (wt-%) alloy. The particles are δ-Ni₂Si growing in a Cu-matrix at 675 °C. These particles are rod shaped and both average length and width are shown as a function of time. The agreement with experimental data from (19) is very good.

References

- [1] H. L. Lukas, S. G. Fries and B. Sundman, "Computational Thermodynamics: The Calphad Method", Cambridge University Press, Cambridge, United Kingdom, (2007)
- [2] N. Saunders and A. P. Miodownik, "CALPHAD – A Comprehensive Guide", Oxford, Pergamon, (1998)
- [3] J.O. Andersson, T. Helander, L. Höglund., P.F. Shi and B. Sundman, "Thermo-Calc and DICTRA, Computational tools for materials science". Calphad 26 (2002) 273-312.
- [4] The Precipitation Module (TC-PRISMA) User Guide 2022b, <https://thermocalc.com/support/documentation> (accessed Oct. 12, 2022).
- [5] Thermo-Calc Software TCCU5 Cu-alloys Database <https://thermocalc.com/products/databases/copper-based-alloys/> (accessed Oct. 12, 2022).
- [6] Thermo-Calc Software MOBCU5 Cu-alloys Mobility Database <https://thermocalc.com/products/databases/copper-based-alloys/> (accessed Oct. 12, 2022).
- [7] M. Hillert, "The compound energy formalism", Journal of Alloys and Compounds 320 (2001) 161-176.
- [8] Y. Tang, Q. Chen and A. Engström, Journal of Japan Institute of Copper 59 (2020) 7-12.
- [9] Y. Tang, Q. Chen and A. Engström, Diffusion Foundations 15 (2018) 1–22.
- [10] M. Li, Z. Du, C. Guo, C. Li, J. Alloys Compd. 477 (2009) 104-117.
- [11] C.-H. Wang, S.-W. Chen, Metall. Mater. Trans. A. 34 (2003) 2281–2287.
- [12] O. Heusler, Zeitschrift für Anorg. und Allg. Chemie. 159 (1927) 37–54.
- [13] T. R. Graham, J. R. Long, C. E. Aramantrout, A. H. Roberson, Trans. Am. Inst. Min. Met. Pet. Eng. 185 (1949) 675–682.
- [14] H. Watanabe, N. Kono, M. Gonda, J. Japan Inst. Met. 36 (1972) 297–305.
- [15] O. Kubaschewski, Silver-Copper-Nickel in "Ternary Alloy Phase Diagrams", G. Petzow, G. Effenberg, Eds., (1998) 596–604.
- [16] B. Korrojy, L. Ekbom, H. Fredriksson, Adv. Mater. Sci. Eng. 2009, 1–9.
- [17] J. Brillo, I. Egry, T. Matsushita, Int. J. Mater. Res. 97 (2006) 1526–1532.
- [18] L. V. Kamaeva, A. Y. Korepanov, V. I. Lady'yanov, High Temp. 56 (2018) 514–518.
- [19] C. Watanabe, R. Monzen, J. Mater. Sci. 46 (2011) 4327–4335.

(1) Thermo-Calc Software AB, Råsun-davägen 18, SE-169 67 Solna, Sweden

Corrosion resistance of lead-free brass alloys in contact with drinking water

Klein, T. (1)

Within the past seven years three research projects at IKS aimed to investigate the corrosion behavior of lead-free copper zinc alloys in contact with drinking water.

In 2018, first tests results on the corrosion resistance of lead-free brass alloys in contact with cold drinking waters with different concentration levels ($c(\text{Cl}^-)$, $K_{\text{S}_{4,3}}$, $c(\text{SO}_4^{2-})$) were presented at the Copper Alloys Conference in Milan [1]. The project aimed to generate realistic information on the corrosion behavior of the novel lead-free brass alloys CuZn21Si3P and CuZn38As in order to develop a user-friendly tool for the estimation of the expected corrosion resistance in contact with corrosion promoting waters. The tests were performed in a complex test rig, consisting of three test rigs with four test lines each, which enables different concentration levels by dosing salt solutions in the test lines individually (s. Figure 1).

While the test results with the reference material CuZn40Pb2 correlated well with the Turner diagram [2], the lead-free alloys did not comply with the curve for dezincification resistant copper zinc alloys [3]. In addition, the two lead-free alloys exhibited different corrosion behavior in terms of differing mechanisms and a suspected detachment of corroded grains from the surface (s. Figure 2).

In order to further investigate the corrosion behavior of these lead-free alloys, another research project was submitted and is now in progress. It includes further tests of lead-free brass alloys in contact with cold drinking water in the complex test rig (s. Figure 1). During the experiments of the current project, metal migration is measured. Furthermore, depths of corrosive attacks of test specimens are measured after 3, 6 and 12 months in the test rig and a novel approach aims to examine the laminar corrosion of the specimens, using computed tomography.

Within the next two years, the data of the long-term tests will be used for correlations with different approaches to develop a short-term lab test which is intended to help evaluate the corrosion behavior of lead-free brass alloys, as the existing tests according to DIN EN ISO 6509-1 were found not to give reliable results for these new alloys in comparison to the common leaded ($\alpha+\beta$) brass.

Furthermore, the corrosion behavior of lead-free brass alloys in contact with hot drinking water under realistic conditions (long circulation/stagnation and short flushing events) was investigated in two test rigs in Dresden and Lübbenau within the scope of a completed project [4]. These tests with different copper zinc alloys under circulating hot water (60 °C) and stagnating warm water (no heating in stagnation lines) conditions showed that especially the lead-free copper zinc alloy CuZn21Si3P exhibited comparable average depths of corrosive attack to the leaded CuZn40Pb2 in contact with the harmless Dresden water and also comparable or even worse average depths of corrosive attacks in

contact with the corrosion promoting water in Lübbenau, while the alloys CuZn38As and CuZn33Pb1AlSiAs performed better than both the leaded alloy CuZn40Pb2 and the lead-free alloy CuZn21Si3P in both test rigs (s. Figure 3). The circulating warm water conditions always lead to higher corrosive attacks for all tested alloys. As these data were obtained after a testing period of only 26 weeks, further tests should be performed with the lead-free alloys with testing periods of 52 weeks or more in order to assess the long-term corrosion behavior of these alloys in contact with heated drinking water.

Another project dealt with the influence of heat treatment on the corrosion resistance of low-leaded and lead-free copper zinc alloys in contact with the harmless drinking water in Dresden and the corrosion promoting water in Lübbenau. For this purpose, brass rods were heat treated with different parameters, then processed to test specimens according to DIN EN 15664-1 and used for the following short-term lab tests:

- dezincification resistance according to DIN EN ISO 6509-1,
- measurements of the hardness (HV0,1) and

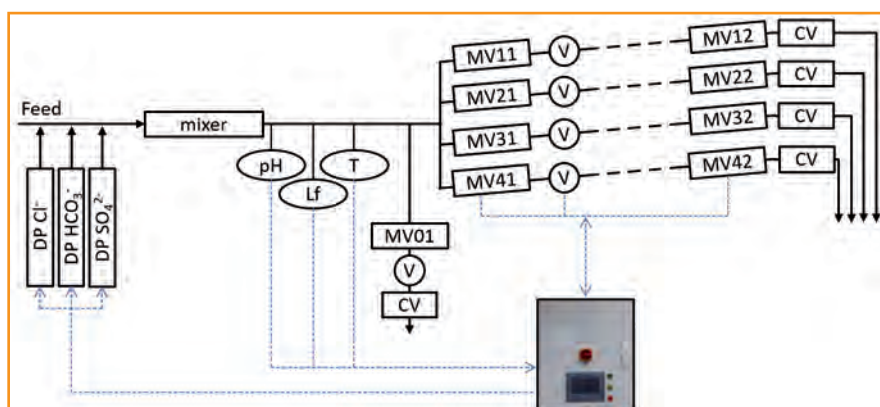


Fig. 1: Scheme of one test rig with salt dosing via the dosing pumps (DP) with pH, temperature and conductivity sensors and magnetic valves (MV) and flow metes (V) and manual control valves (CV) for flow control and regulation

- the microstructure was analyzed in metallographic cuts.

Proper heat treatment is a known method for the improvement of the corrosion resistance of brass alloys in terms of lowering the risk of stress corrosion by releasing stress induced by processing and lowering the risk of dezincification by reducing the fraction of the less corrosion resistant β -phase and homogenizing the microstructure. The alloys CuZn-33Pb1AlSiAs, CuZn35Pb1.5AlAs and CuZn35Pb1.5AlAs exhibited a higher dezincification resistance with more intense heat treatment following the results of the estimation of the dezincification resistance according to DIN EN ISO 6509-1 [5]. However, during the long-term tests of one year in contact with the corrosion promoting water in Lübbenau in a test rig according to DIN EN 15664-1, the test lines with specimens with more intense heat treatment showed higher copper migration than the less intense heat-treated specimens, also suggesting a detachment of grains from the surfaces in contact with the water.

This again demonstrates the need for a method to quantify the total depth of corrosive attack including a possible surface detachment, which cannot be

measured with existing methods in metallographic cuts.

This layer detachment supposedly has individual reasons for the two lead-free alloys. CuZn38As, on the one hand, has a tendency towards intercrystalline corrosion, which weakens the mechanic stability of these products. On the other hand, dezincification of all phases was observed in several specimens of alloy CuZn21Si3P, as also Choucri et al. [6] described. Both mechanisms weaken the microstructure and could lead to layer detachment at high flow rates. Therefore, without fully understanding the corrosion mechanisms of these lead-free alloys, only depths of corrosive attacks may not be enough to assess the corrosion resistance of lead-free alloys in contact with drinking water. The results of the current project, which includes the quantification of the total depth of corrosive attack, will provide important knowledge and understanding of the corrosion mechanisms of lead-free copper-zinc-alloys.

Acknowledgement

All four mentioned research projects at IKS were financially supported by the Federal Ministry for Economic

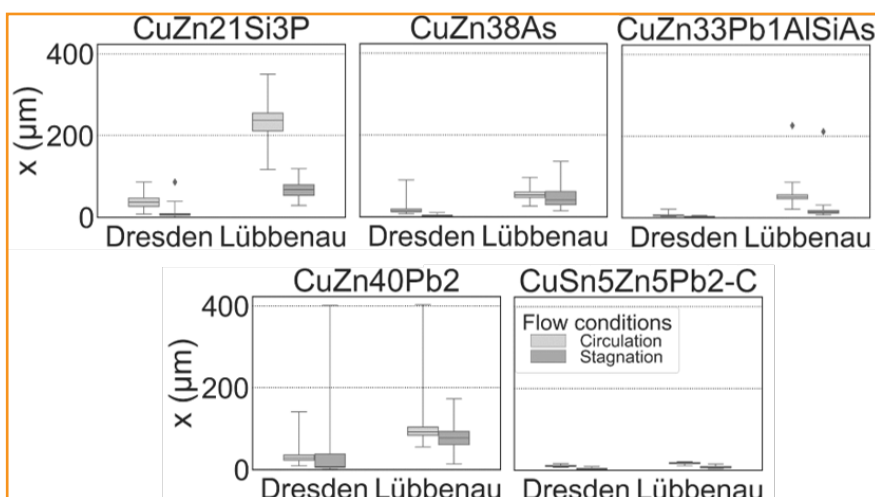


Fig. 3: Depths off corrosive attack of the test specimens of the alloys CuZn21Si3P, CuZn38As, CuZn33Pb1AlSiAs, CuZn40Pb2 and CuSn5Zn5Pb2-C (left to right, row-wise) after 26 weeks under circulating (heated) and stagnating (non-heated) conditions in the test rigs in Dresden and Lübbenau; plotted as boxplots (whiskers = 15 x box length)

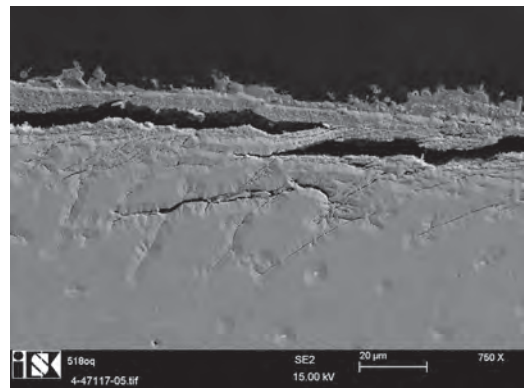


Fig. 2: SEM image of an ion beam milled specimen of alloy CuZn38As after 8 months in the test rig with dosed drinking water

Affairs and Climate Action on the basis of a resolution of the German Bundestag within the scope of the funding program INNO-KOM.

References

- [1] Klein, T.: "Development of a procedure to prevent dezincification of brass components in drinking water installations". Presentation at the Copper Alloys 2018 Conference in Milan. April 11th – 12th, 2018.
- [2] Turner, M.E.D.: "The Influence of Water Composition on the Dezincification of Duplex Brass Fittings". Proceedings of the Society for Water Treatment and Examination 10. S. 162 – 179, 1961
- [3] Krebs, P.: "Grundlagen der Siedlungswasserwirtschaft - Kap. 3 Wasserversorgung". URL: https://tu-dresden.de/bu/umwelt/hydro/isi/sww/ressourcen/dateien/lehre/dateien/grdl_swv_bauing/vorlesung_bauing_swv_ws1011/SWW_Bauing_04_Wasserversorgung.pdf?lang=de [18.10.2022], 2008
- [4] Klein, T.: „Warmwasserbeständigkeit neuartiger Kupfer-Zink-Legierungen“. Presentation at GfKORR working group „Corrosion and corrosion protection of copper alloys“, November 11th, 2021.
- [5] Klein, T.: "Short-term versus long-term tests of lead-free and low-leaded brass alloys in contact with drinking water". Presentation at CEOCOR 2019 in Copenhagen. May 22nd – 23rd, 2019.
- [6] Choucri, J. et al.: "Corrosion Behavior of Different Brass Alloys for Drinking Water Distribution Systems" Metals 2019, 9, 649. doi:10.3390/met9060649.

(1) Theresa Klein, Institut für Korrosionsschutz Dresden GmbH, Gostritzer Str. 65, D-01217 Dresden

Effect of Heat Treatment on Transformation Temperatures, Microstructure, and Deformation Behavior of a High Temperature Copper-based Shape Memory Alloy

Kranner, C.; Schelnberger, B.; Hoffmann, F.; Keßler, R.; Krieg, R.; Theiß, R.; Dültgen, P. (1)

The effect of different heat treatment conditions on a pseudoplastic polycrystalline Cu-Al-Mn-Ni shape memory alloy before further forming processes was studied. To this end, a Cu-based shape memory alloy was fabricated and analyzed. The transformation temperatures were investigated by DSC. Furthermore, the microstructural evolution was observed with an optical microscope and compression tests at a quasi-static loading rate were performed. An applicable Cu-based shape memory alloy with moderate cold workability was identified for use in elevated temperature environments. The investigation proves the influence of the homogenization time and cooling media on the transformation temperatures, microstructure, and deformation behavior.

Shape memory alloys (SMAs) undergo a reversible martensitic phase transformation in the solid state, resulting in a macroscopic shape change. The phase transformation is subject to a defined stress-temperature relationship. The characteristic material behavior is, at this time, mainly used with the Ni-Ti alloy system in the fields of medical engineering, aerospace, and automotive industry. These binary alloys have already been extensively investigated both mechanically and microstructurally and are characterized by good shape memory properties and a long lifetime. However, their use is restricted by limited operating temperatures, cost-intensive base materials, and the required complex melting technology. Slight changes in the process conditions can influence the chemical composition and lead to significant variations in the shape memory properties [1, 2, 3, 4, 5].

Current developments are mainly driven by the aerospace industry and the automotive sector, where the high working density of high-temperature-SMA actuators is particularly advantageous for lightweight actuation. Therefore, ternary Ni-Ti-X-SMAs ($X = \text{Pt, Au, Pd, Hf}$) are used in adaptive

nozzles of gas turbines for acoustic damping or in pressure relief valves in car gearboxes. Cu-based SMAs could offer a lower-cost alternative to Ni-Ti-X alloys and are expected to have high application potential in similar elevated-temperature applications. Cu-based SMAs can expand the application window concerning the phase transformation temperatures of binary Ni-Ti alloy systems [6, 7, 8].

In recent years, researchers have become increasingly interested in the Cu-Al-Ni alloy system with good mechanical properties, especially high strengths, and high transformation temperatures, depending on Al- and Ni-content, as well as the Cu-Al-Mn alloy system with high ductility under tensile and compressive load conditions [9, 10, 11].

Studies on Cu-Al-Mn-Ni alloy systems showed the advantageous combination of both material properties. These quaternary alloys are noted for high strain recovery of up to 6 % and pseudoplasticity in the range of 3 % to 5 % as well as increased deformation behavior compared to Cu-Al-Ni alloys. The martensitic phase transformation in the polycrystalline state and transformation temperatures are significantly influenced by the chemi-

cal composition. Several studies have examined the effects of the used alloy elements and the effects on phase transformation and microstructure. Studies on quaternary alloys of the Cu-Al-Mn-Ni system showed an increase in transformation temperatures with increasing Ni content. Furthermore, the addition of Ni results in the formation of the martensitic phase β'_1 (18R structure) at room temperature. γ'_1 martensite (2H structure) was observed in Cu-Al-Mn alloyed with Ni [12, 13, 14, 15, 16, 17, 18].

However, previous research activities have disregarded the role of mechanical and microstructural properties ahead of further forming processes and the importance of controlling and influencing casting and especially heat treatment parameters. In particular, the influence of homogenization strategies deserves more research attention. Kranner et al. found a slight effect of the homogenization heat treatment on the transformation temperatures of pseudoelastic Cu-Al-Mn-Ni SMAs, while significant microstructural changes already occur after a short homogenization time [19]. Canbay et al. noted a significant effect of different cooling media on phase transformation temperatures and thermal hysteresis for Cu-Al-Fe-Mn SMAs [20].

The aim of the research project is to comprehensively characterize Cu-Al-Mn-Ni-based SMAs to make them usable for SMEs (small and medium-sized enterprises). The focus is on the development of new or further improvement of existing alloys of this quaternary Cu-based system, with a focus on the casting process, the heat treatment strategies, and the mechan-

ical, microstructural, as well as thermal material characterization. A wide transformation temperature window in the range of -100 °C to 250 °C will be considered for further examinations and later utilization.

The aim of this study is to produce a homogeneous pseudoplastic Cu-Al-Mn-Ni SMA by a permanent mold casting process, considering the effect of homogenization time and cooling media before subsequent forming processes. For this purpose, the transformation temperatures are determined by DSC. The microstructure is analyzed by an optical microscope. In addition, quasi-static compression tests were carried out to evaluate the deformation behavior. The intention is to improve the knowledge of the influence of heat treatment strategies on material behavior before further forming processes of Cu-Al-Mn-Ni SMAs and achieving high cold workability.

Materials and Methods

Casting Process and Heat Treatment

A pseudoplastic quaternary SMA with a chemical composition according to Table 1 was produced for the

Cu	Al	Mn	Ni
82.0	11.5	2.5	4.0

Table 1: Chemical composition of a Cu-Al-Mn-Ni SMA

investigations.

The alloy was molten from the pure elements (purity \geq 99.9 %) with an Indutherm VTC 200 V-Ti vacuum induction tilting furnace in a graphite crucible. The total mass of a cast was approximately 550 g. Melting was performed under vacuum to minimize oxide formation, after two purges with argon prior to heating. The material was first heated to 1480 °C (25 K above the melting temperature of nickel) and was then reduced to 1135 °C (about 100 K above liquidus temperature). This was followed by reheating to the casting temperature (1190 °C). The molten alloy was then poured directly into a preheated permanent steel mold (400 °C). After solidification, the cast-

ing was cut into bars with a length of 135 mm. These cast ingots were subsequently homogenized in a tube furnace for 0.5 h, 1 h, 2 h, 4 h, and 8 h at 850 °C under standard atmosphere. The homogenized specimens were quenched with oil or cooled with compressed air (comp. air).

Material characterization

The chemical composition of the cast ingots was determined using an Ametek SPECTROMAXx optical emission spectrometry analyzer. The transformation temperatures of the non-heat-treated and heat-treated ingots were investigated by DSC on a Netzsch DSC 214 Polyma according to DIN 51007 [21] with a heating and cooling rate of 10 K/min in a temperature range of 100 °C to 250 °C. For this purpose, 0.6 mm to 1.0 mm thick slices were cut from the bars with a diamond wire saw and these were brought to a weight, through a radial surface reduction, in the range of 15 mg to 25 mg by wet grinding. The DSC curves were evaluated using the tangent method with the "Protheus - Thermal Analysis" software from Netzsch. Metallographic specimens were examined to study microstructure evolution depending on the used heat treatment conditions and correlated with transformation temperatures and deformation behavior. Therefore, the samples were mounted, ground, and polished up to 0.25 µm. Contrasting was provided by the final mechanical polishing step with silica suspension and the additives ammonia and hydrogen peroxide. Compression tests in accordance with DIN 50106 [22] were performed on a TIRA Test 2820 universal

testing machine up to 20 kN at room temperature (20 °C) with a loading rate of 0.01 s⁻¹. For the tests, cylindrical specimens were turned from the cast ingots with a diameter of 4 mm and a height of 6 mm. σ_s (stress for initiation of martensitic reorientation) and σ_f (stress for completion of martensitic reorientation) were determined by fitting tangents to the compressive stress-strain curve and determining their intersection points.

Results and discussion

Transformation Temperatures

The transformation temperatures depending on the homogenization time are shown in Figure 1. The influence of homogenization time is evident. The martensitic transformation occurs above room temperature at elevated temperatures in a range of 130 °C and 220 °C. This behavior is characteristic of pseudoplastic SMAs and is therefore suitable for high-temperature applications, e.g., in the automotive or aerospace industry. For both cooling conditions (oil and compressed air), the transformation temperatures change significantly within 1 h. Further homogenization treatment resulted in a plateau where the transformation temperatures stabilize and remain at a constant level. In the plateau range, the transformation temperatures after cooling with compressed air (Figure 1a) are minimally below (about 3 K) the values of the oil quenching (Figure 1b). The temperature difference ΔT is in the range of 40 K to 50 K for all homogenization states. The analysis of the as-cast material showed no measurable

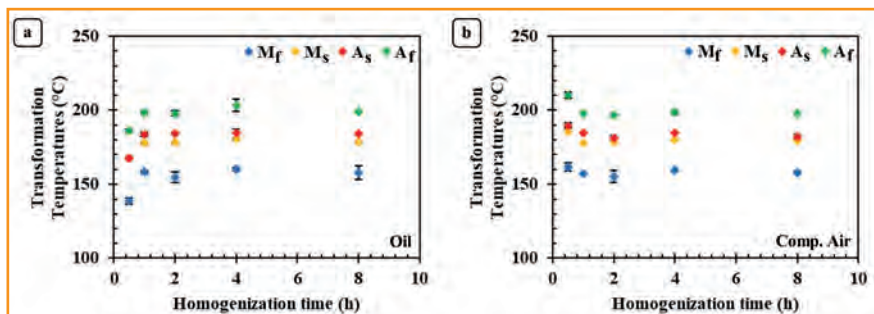


Fig. 1: Transformation temperatures depending on the homogenization time of the Cu-Al-Mn-Ni SMA: a) Quenched in Oil b) Cooled with compressed air.
 A_f (austenite-finish temperature), A_s (austenite-start temperature),
 M_s (martensite-start temperature), M_f (martensite-finish tmeperature)

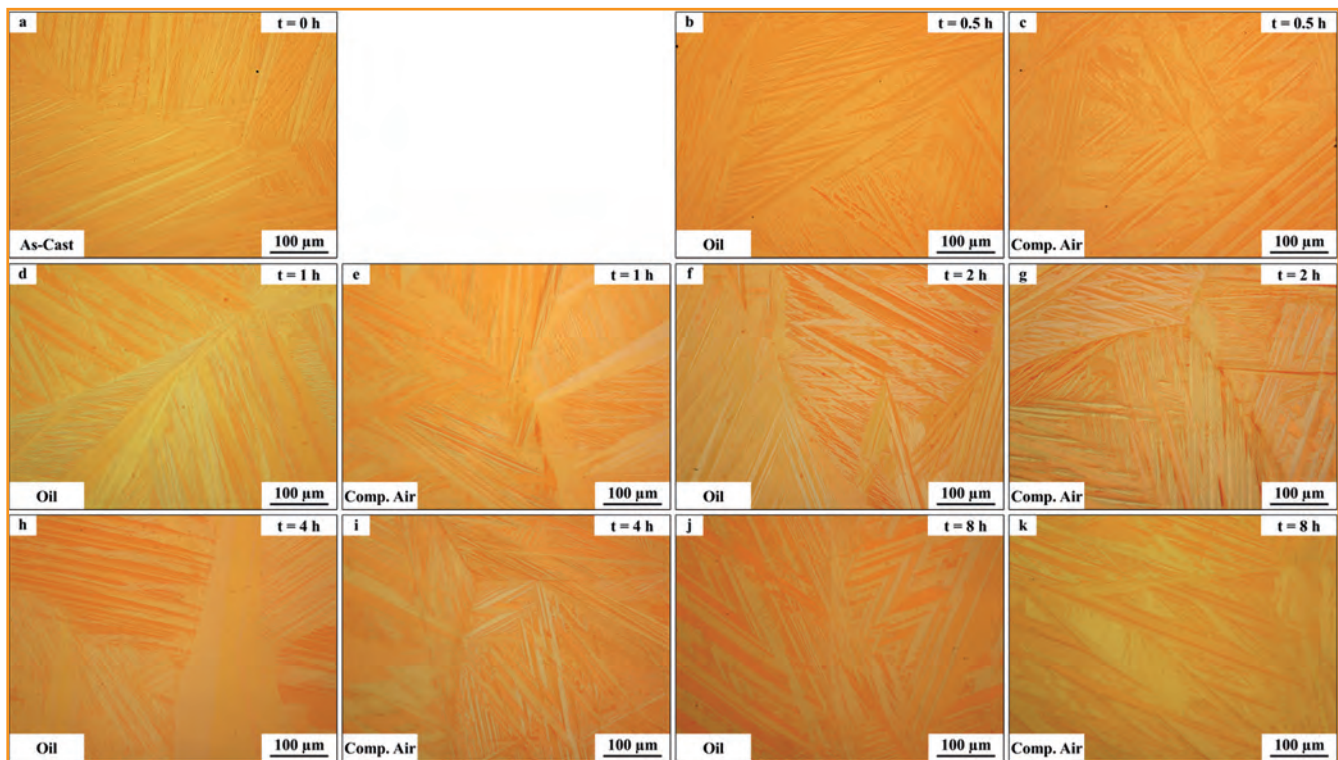


Fig. 2: Optical micrographs of the microstructure depending on the homogenization time: a) Initial microstructure in the as-cast state b) Microstructure after 30 min at 850 °C and quenching in oil c) Microstructure after 30 min at 850 °C and cooled with compressed air d) Microstructure after 1 h at 850 °C and quenching in oil e) Microstructure after 1 h at 850 °C and cooled with compressed air f) Microstructure after 2 h at 850 °C and quenching in oil g) Microstructure after 2 h at 850 °C and cooled with compressed air h) Microstructure after 4 h at 850 °C and quenching in oil i) Microstructure after 4 h at 850 °C and cooled with compressed air j) Microstructure after 8 h at 850 °C and quenching in oil k) Microstructure after 8 h at 850 °C and cooled with compressed air.

peaks in the DSC signal for the used temperature window. Nevertheless, the investigations at different specimen positions and between different casts show only slight variations in the transformation temperatures. The maximum deviations are below 5 K. This demonstrates the adequate homogeneity of the melt and solidification. A reason for this is the process-related electromagnetic stirring of the bath agitation and the use of inert gas and vacuum for purification of the melt. The effect of chemical composition on transformation temperatures is less pronounced for the present Cu-Al-Mn-Ni SMA than for Ni-Ti alloys. Therefore, controlled handling of the alloy during fabrication is simpler to achieve, including for SMEs.

Microstructural evolution

Figure 2 shows the optical micrographs of the Cu-Al-Mn-Ni samples depending on the homogenization time. Figure 2a shows the initial structure in the as-cast state. A homogene-

ously distributed microstructure with straight-aligned martensite plates is visible. The absence of the transformation peaks in the DSC measurement cannot be attributed to the optical micrographs. As a possible cause, internal stress states due to solidification can be considered. Future studies will have to investigate the role of residual stresses. For all homogenized conditions (Figure 2b-k), a “zig-zag” morphology is shown in addition to straight-oriented martensite plates. No significant changes in micro-

structural appearance depending on homogenization time are observed. Nevertheless, it was possible to produce a homogeneous alloy with minimal casting defects.

Deformation Behavior

Figure 3 shows the typical compressive stress-compression curves as a function of the homogenization time. The mechanical material behavior depends on the homogenization time and the cooling conditions. It is evident

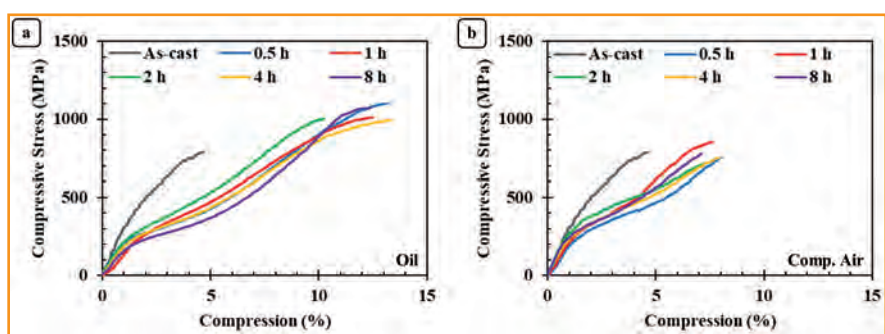


Fig. 3: Typical compressive stress-compression curve of Cu-Al-Mn-Ni SMA specimens at room temperature depending on the homogenization time: a) Quenched in Oil b) Cooled with compressed air.

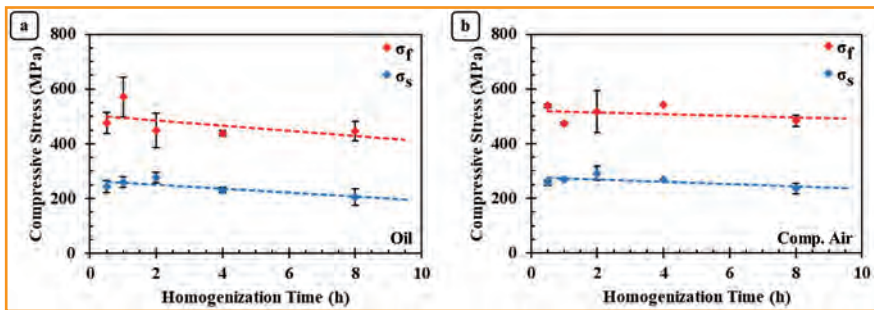


Fig. 4: Transformation stresses depending on the homogenization time under compressive stress: a) Quenched with Oil b) Cooled with compressed air.

that all present material conditions cannot withstand the maximum test load of 20 kN (about 1600 MPa related to the specimen cross-sectional area). The as-cast specimens show no pseudoplastic behavior, i. e. the material state shows a typical elastic-plastic deformation, but up to now, it is not clear, if this means that the samples

time for both cooling conditions (Figure 4). The decrease in transformation stresses σ_s and σ_f with increasing homogenization time is more pronounced when quenching in oil (Figure 4a) than when cooling with compressed air (Figure 4b).

Table 2 summarizes the mechanical shape memory properties. The

plateau region during the mechanical tests proves the absence of the transformation peaks in the DSC signal. It can be summarized that a brief homogenization heat treatment can already significantly improve the mechanical material properties.

Conclusion

The investigated Cu-Al-Mn-Ni alloy has the potential to be an applicable SMA and can compete with binary Ni-Ti and ternary Cu-based alloys, especially due to its use in elevated temperature applications. The high transformation temperatures in the unprocessed state indicate that the processed material will exhibit pseudoplastic shape memory properties. Homogenization leads to a shift in transformation temperatures and

Homogenization time (h)	Quenching with oil				Cooling with compressed air			
	σ_s (MPa)	σ_f (MPa)	$\Delta\epsilon_{plateau}$ (h)	$\epsilon_{fracture}$ (%)	σ_s (MPa)	σ_f (MPa)	$\Delta\epsilon_{plateau}$ (h)	$\epsilon_{fracture}$ (%)
0	-	-	-	4.1 ± 0.4	-	-	-	4.1 ± 0.4
0.5	243.4 ± 21.5	475.4 ± 38.1	4.1 ± 0.4	11.0 ± 2.2	256.4 ± 8.5	538.9 ± 6.9	4.8 ± 0.4	8.9 ± 0.8
1	259.7 ± 19.8	570.6 ± 73.3	4.2 ± 0.7	11.0 ± 1.3	269.2 ± 3.9	473.7 ± 4.7	2.8 ± 0.2	7.3 ± 0.3
2	276.9 ± 18.3	447.9 ± 62.6	2.4 ± 1.1	10.6 ± 1.2	291.2 ± 26.8	517.4 ± 77.3	3.9 ± 0.8	6.3 ± 1.1
4	230.9 ± 10.2	438.7 ± 9.7	3.9 ± 0.6	11.7 ± 2.0	269.7 ± 0.0	541.0 ± 0.0	4.3 ± 0.0	7.9 ± 0.0
8	205.9 ± 29.4	446.0 ± 36.7	4.8 ± 0.8	11.2 ± 1.3	235.8 ± 18.4	483.9 ± 20.5	4.1 ± 1.1	8.0 ± 1.7

Table 2: Mechanical Properties of Cu-Al-Mn-Ni SMA (σ_s - stress for initiation of martensitic reorientation; σ_f - stress for completion of martensitic reorientation; $\Delta\epsilon_{plateau}$ - plateau compression (difference between ϵ_f (compression for completion of martensitic reorientation) and ϵ_s (compression for initiation of martensitic reorientation)); $\epsilon_{fracture}$ - compression until failure).

do not show a pseudoplastic behavior at all. In contrast, the homogenized samples after quenching in oil (Figure 3a) already show a plateau region after a homogenization time of 0.5 h, in which the stress increases slightly and continuously. The specimens cooled with compressed air (Figure 3b) show a shorter plateau area. The possible detwinning of the martensitic phase needs to be considered during further processing by cold-forming processes. This is followed by plastic deformation of the material. Specimens cooled with compressed air are inferior to those quenched with oil concerning compression to fracture.

The level of the stress plateau decreases with increasing homogenization

investigated Cu-Al-Mn-Ni SMA shows good shape memory properties for the homogenized states. The martensitic phase transformation initiates at high compressive stresses in a range of 200 MPa to 300 MPa and a pseudoplastic compression up to 4.8 %. The stress change in the plateau area is around 250 MPa. Fracture of the homogenized specimens after oil quenching occurred in the range of 10 % to 12 % compression and for compressed air cooling between 4 % and 9 % compression. The specimens in the non-heat-treated condition (as-cast condition) did not show pseudoplastic behavior and failure occurred after about 4 % compression. Therefore, the absence of the characteristic pla-

teau region during the mechanical tests proves the absence of the transformation peaks in the DSC signal. It can be summarized that a brief homogenization heat treatment can already significantly improve the mechanical material properties.

Outlook

Based on the results of this study, it was shown that the investigated Cu-Al-Mn-Ni alloy provides the potential to be an applicable shape memory alloy in the elevated temperature range for the non-processed state. The alloy can compete with existing binary NiTi and Cu-based shape memory alloys due to its pseudoplastic material behavior at elevated temperatures. Further mechanical and microstructural investigations are planned to evaluate the material behavior. The focus of additional investigations is on the development and optimization of a forming process route to a suitable semi-finished product. For this purpose, standard industrial processes such as rotary swaging, hot rolling, and wire drawing will be used. Experiments concerning thermal and electrical properties as well as thermal stability and corrosion resistance will also be carried out.

Acknowledgments

The research project 49VF210023 "Ertüchtigung von Cu-FGL" from the Research Association Forschungsgemeinschaft Werkzeuge und Werkstoffe e.V. (FGW), Papenberger Straße 49, 42859 Remscheid, Germany, was supported by the Federal Ministry for Economic Affairs and Climate Action. The authors thank Mr. M. Mehrbakhsh for his support during the mechanical tests.

References

[1] Shape Memory Materials, Cambridge University Press, 2002.

- [2] J. M. Jani, M. Leary, A. Subic and M. A. Gibson, "A review of shape memory alloy research, applications and opportunities," *Materials & Design* (1980-2015), vol. 56, p. 1078–1113, April 2014.
- [3] K. K. Alaneme and E. A. Okotete, "Reconciling viability and cost-effective shape memory alloy options – A review of copper and iron based shape memory metallic systems," *Engineering Science and Technology, an International Journal*, vol. 19, p. 1582–1592, September 2016.
- [4] D. Hodgson and S. Russell, "Nitinol melting, manufacture and fabrication," *Minimally Invasive Therapy & Allied Technologies*, vol. 9, p. 61–65, January 2000.
- [5] R. J. Wasilewski, S. R. Butler, J. E. Hanlon and D. Worden, "Homogeneity range and the martensitic transformation in TiNi," *Metallurgical Transactions*, vol. 2, p. 229–238, December 1971.
- [6] J. M. Jani, M. Leary and A. Subic, "Shape Memory Alloys in Automotive Applications," *Applied Mechanics and Materials*, vol. 663, p. 248–253, October 2014.
- [7] D. Stoeckel, "Shape memory actuators for automotive applications," *Materials & Design*, vol. 11, p. 302–307, December 1990.
- [8] J. Webster, "High integrity adaptive SMA components for gas turbine applications," in *Smart Structures and Materials 2006: Industrial and Commercial Applications of Smart Structures Technologies*, 2006.
- [9] U. Sarı and T. Kirındı, "Effects of deformation on microstructure and mechanical properties of a Cu-Al-Ni shape memory alloy," vol. 59, p. 920–929, July 2008.
- [10] V. Recarte, R. B. Pérez-Sáez, J. S. Juan, E. H. Bocanegra and M. L. Nó, "Influence of Al and Ni concentration on the Martensitic transformation in Cu-Al-Ni shape-memory alloys," *Metallurgical and Materials Transactions A*, vol. 33, p. 2581–2591, August 2002.
- [11] R. Kainuma, S. Takahashi and K. Ishida, "Thermoelastic martensite and shape memory effect in ductile Cu-Al-Mn alloys," *Metallurgical and Materials Transactions A*, vol. 27, p. 2187–2195, August 1996.
- [12] S. N. Saud, E. Hamzah, T. A. A. Bakar and R. Hosseiniyan, "A Review on Influence of Alloying Elements on the Microstructure and Mechanical Properties of Cu-Al-Ni Shape Memory Alloys," *Jurnal Teknologi*, vol. 64, September 2013.
- [13] T. Manzoor, M. Zafar, M. Ali, M. Saleem and W. Y. Kim, "Effect of microstructural phases on thermo-mechanical analysis of ductile Cu-Al-Mn-Ni memory alloys for structural applications," *Materials Express*, vol. 10, p. 1337–1345, August 2020.
- [14] S. Karthick, S. Shalini, S. S. M. Prabu, K. Suhel, A. Vandana, C. Puneet, S. M. Kumar, R. Venkatesh and I. A. Palani, "Influence of quaternary alloying addition on transformation temperatures and shape memory properties of Cu-Al-Mn shape memory alloy coated optical fiber," vol. 153, p. 107379, March 2020.
- [15] C. A. K. S. U. Canbay and V. Sampath, "Microstructural and Thermal Investigations of Cu-Al-Mn-Ni Shape Memory Alloys," *Materials Today: Proceedings*, vol. 4, p. 10682–10689, 2017.
- [16] U. S. Mallik and V. Sampath, "Influence of aluminum and manganese concentration on the shape memory characteristics of Cu-Al-Mn shape memory alloys," *Journal of Alloys and Compounds*, vol. 459, p. 142–147, July 2008.
- [17] U. Sarı, "Influences of 2.5wt% Mn addition on the microstructure and mechanical properties of Cu-Al-Ni shape memory alloys," *International Journal of Minerals, Metallurgy, and Materials*, vol. 17, p. 192–198, April 2010.
- [18] Y. Sutou, R. Kainuma and K. Ishida, "Effect of alloying elements on the shape memory properties of ductile Cu-Al-Mn alloys," Vols. 273–275, p. 375–379, December 1999.
- [19] C. Krancher, B. Schelnberger, F. Hoffmann, R. Krieg, R. Theiß and P. Dültgen, "Investigation of transformation temperatures, microstructure, and deformation behavior of a pseudoelastic Cu-based shape memory alloy," [not yet published], 2022.
- [20] C. A. Canbay, O. Karaduman, N. Ünlü, S. A. Baiz and İ. Özkul, "Heat treatment and quenching media effects on the thermodynamical, thermoelastical and structural characteristics of a new Cu-based quaternary shape memory alloy," *Composites Part B: Engineering*, vol. 174, p. 106940, October 2019.
- [21] DIN 51007:2019-04, "Thermal analysis - Differential thermal analysis (DTA) and differential scanning calorimetry (DSC) - General Principles".
- [22] DIN 50106:2016-11, "Testing of metallic materials - Compression test at room temperature".

(1) Christian Krancher, Benjamin Schelnberger, Fabian Hoffmann, Ralph Keßler, Romina Krieg, Ralf Theiß, Peter Dültgen, Forschungsgemeinschaft Werkzeuge und Werkstoffe e. V.

Copper Wave Springs for Electromechanical Applications

Philipp, J. (1); Frehn, A. (2); Seeger, S. (1), Aust, M. (1); Hertweck, B. (1)

Wave springs are typically used in applications and products where a comparatively high spring force is required in a small installation space. For purely mechanical applications, these springs are made from classic spring materials such as austenitic stainless steel 1.4310 or high-carbon steels. The basic material is flat wire, which is produced from round wire by rolling.

The current trend shows that the springs are used in electromechanical or mechatronic applications. Due to the poor electrical conductivity of the classic spring materials, conductive materials such as copper and aluminium are needed. The behaviour of conventional spring materials and spring types under mechanical load is very well described. However, there is a lack of knowledge about the electromechanical behaviour of modern spring types. In this work, alternative materials are investigated that meet the above-mentioned applications in terms of both mechanical and electrical properties.

A copper-beryllium alloy and a beryllium-free alloy were investigated as substitutes for 1.4310. For this purpose, wave springs were manufactured from these different materials and compared with regard to their mechanical and electrical properties. The results were evaluated for a practical use in combined electro-mechanical applications. Furthermore, it was investigated to what extent a silver coating applied by a plasma coating process can improve the electrical contact of the springs. The results revealed a good formability of the copper materials which allows rolling into flat wire and a subsequent forming into wave springs.

Despite of the 50 % lower tensile strength, the CuBe wave springs show similar spring properties in comparison to the springs made of 1.4310. The electrical characterisation showed the expected better electrical conductivity of the copper springs. Coating the ends of the springs with silver proved to be practical and demonstrates, that a reduction in contact resistance as well as a higher corrosion resistance can be achieved.

In summary, this project showed that copper materials can be used as a substitute for 1.4310 stainless steel in electro-mechanical wave spring applications. This can lead to reduced power losses in application due to the better electrical conductivity and a reduction of material demand by removing the need for an additional electrical conductor. Furthermore, it has been shown that beryllium-free copper alloys can also be used in the course of sustainability and environmental aspects in this area.



Copper Wave Springs

(1) KERN-LIEBERS Group of Companies
(2) Materion Corporation

Innovative Laser Technologies for Copper Applications in e-Mobility

Möller, M.; Papastathopoulos, E.; Bocksrocker, O. (1)

The global transformation of automotive powertrain technologies has accelerated significantly in recent years from the conventional internal combustion engines to e-Mobility. The demand for components for electric cars and alternative drives is continuously increasing. Many production approaches are taking advantage of laser technology. It connects battery cells to create modules and battery packs.

The ongoing development in electromobility and especially in power electronics is leading to increasing production numbers of inverters and more efficient control units. New manufacturing technologies using lasers support higher performance in the production of power electronics and control units in large quantities. Laser welding technology makes it possible to connect internal or external copper contacts cleanly and without mechanical contact. The latter enables the design of more compact modules and faster switching of inverters.

The paper will provide further details on the huge variety of laser applications in electrically conductive connections like busbars (see Fig. 0) compared to traditional bolted connections used in automotive applications today.

Copper – Laser technologies for processing high reflective materials

The major advantage of processing copper with green wavelength, arises from the fact that the absorption of the green wavelength is much higher (e.g. 8 times at room temperature) compared to standard NIR laser wavelengths around 1030 nm (see Fig. 1). The higher absorption facilitates a significant enhancement of efficiency and reproducibility of the welding process. Thereby copper parts can be welded with unsurpassed seam quality. This makes green high-power lasers an extremely versatile and easy-to-use tool for a range of applications, for

example in the context of e-Mobility and power storage.

Utilizing green wavelength with high power and outstanding beam quality

Advances in TruDisk laser technology have enabled the commercial introduction of industrial CW laser sources with green wavelength 515 nm at a power range of 3 kW and beam parameter product (BPP) of 6-8 mm²mrad. The superb beam quality of this laser enables remote welding of copper by means of laser scanners with a working distance in the range of 340 mm and a scan field size of 240 x 140 mm. The welding performance of this arrangement is demonstrated in Fig. 2 in trials involving bead-on-plate welding of a 5 mm thick copper (Cu-ETP) plate. The insets show

the quality ratings of the seams from decent (yellow) over good (light green) to excellent (dark green). The results marked with dark-green symbols are associated to welding in the heat conduction regime. The curves shown in Fig. 2 correspond to welding at different defocus settings and thereby to different beam diameters (BD) on the workpiece. With a beam diameter 0.632 mm heat conduction welding is facilitated in a broad process window ranging in welding speeds from 1 to >35 m/min, while the maximum welding depth is limited to <1.5 mm. To increase the welding depth, a smaller beam diameter is implemented e.g. by BD 0.447 mm welding depths above 3 mm are possible. However, the welding results with high seam quality, corresponding to the heat conduction regime, are then limited in a process window >7 m/min and a welding depth of <1.3 mm. At welding speeds in the range of 1 m/min the process is taking place in the keyhole welding regime, thereby only decent seam quality is achieved (orange symbols in Fig. 2). Between the keyhole and the heat conduction regimes we find a range of

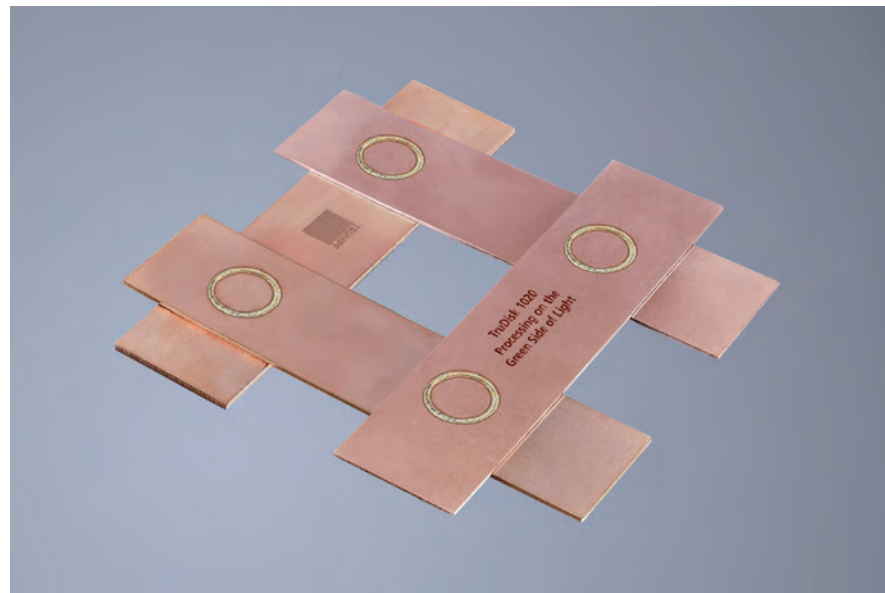


Fig. 0: Copper busbars, welded with green laser

process parameters that relate to the so-called transition mode. The results associated to this parameter range, are marked with the light green symbols, and correspond to seam qualities that are rated as good for industrial application.

Beam Shaping with dynamic change of power distribution

The high versatility of BrightLine Weld by flexibly distributing the laser power into the core and the ring of a dual-core LLK can be further exploit-

technology has the potential to significantly improve motor performance, while at the same time reducing the size of the stator. Major challenges to be address in this context involve the short process times required for high throughput production. Additionally, one of the key issues in laser welding of copper hairpins are the spatters emerging out of the welding process, which can contaminate the surrounding components. Furthermore, the formation of pores within the weld, reduces the connection area between the paired parts, thereby limits the

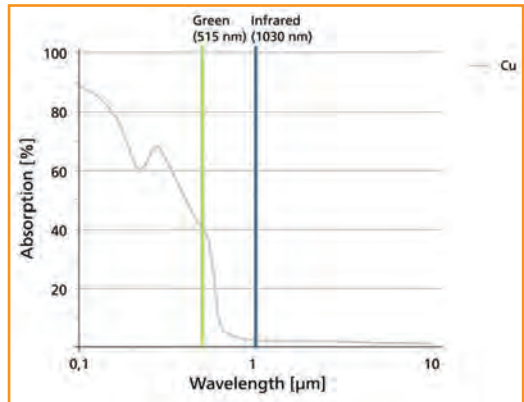


Fig. 1: Absorption of laser power at different wavelengths

visible wavelength and the dynamical adaptation of the power distribution during the welding process. We demonstrated application trials related to automotive electronics as well as hair pins of electric vehicle stators. The high flexibility of the method, the optimal utilization of the available laser power, as well as the combination with exchangeable LLKs and multiple beam outputs at unsurpassed beam quality and power, constitute BrightLine Weld a unique tool for optimizing the quality and productivity of laser welding processes.

(1) Dr. Mauritz Möller, Dr. Evangelos Papastathopoulos, Oliver Bocksrocker, TRUMPF Laser- und Systemtechnik GmbH, Johann-Maus-Straße 2, 71254 Ditzingen

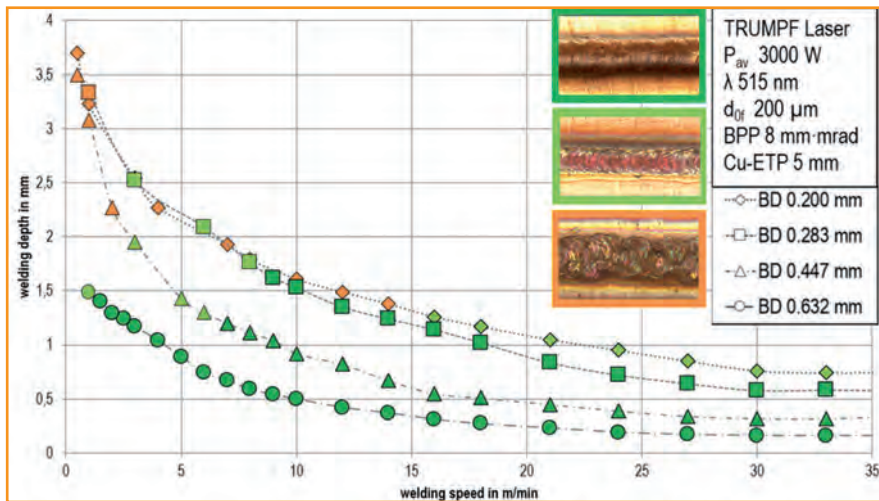


Fig. 2: Bead-on-plate welding results on a copper (Cu-ETP) plate of 5 mm thickness, with a 3 kW TruDisk at 515 nm wavelength, using single-spot beam at different beam diameter (BD)

ed by means of dynamically changing the power distribution during the welding process. Since the optimal power distribution may vary, depending on the state at which the melt pool instantaneously undergoes, dynamically shaping the beam profile while utilizing the full available power of the laser source constitutes a unique property that can be exploited to enhance process quality and productivity. We demonstrate this property in trials involving hair-pin welding (see Fig. 3) of the stator of an electric vehicle. In the production of vehicle stators, manufacturers are moving to copper hairpin technology instead of conventional copper winding. The hairpin

bond strength and electric conductivity of the connection. We have previously reported how the use of BrightLine Weld can significantly reduce the formation of spatters and pores during hair pin welding, resulting in consistently high-tensile connections with an excellent level of conductivity.

Summary

BrightLine Weld is a versatile tool enabling unique possibilities for optimization of welding processes. In the present paper, various novelties of BrightLine Weld technology were presented, involving the application of the method in high-power CW lasers with

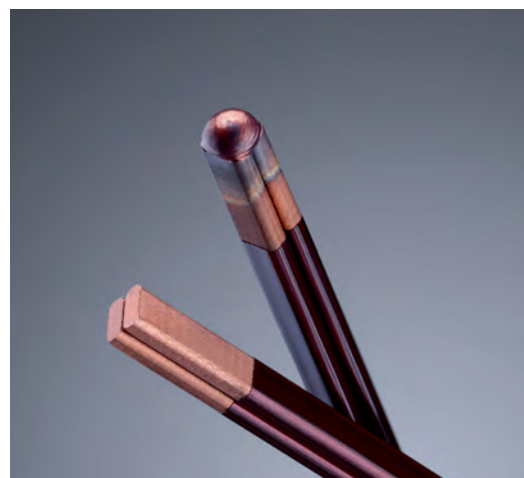


Fig. 3: Hair-pin welding in e-Drive production

Investigation of heat treatment to improve the machinability of lead-free brass alloy CW511L

Müller, M. S. (1); Tomovic Petrovic, S. (2); Sørby, K. (1)

Machinability of brass is important in the manufacturing of couplings for drinking water supply systems. The reduction or elimination of lead in brass alloys affects both the cutting forces and the chip formation. Lead-free brasses that consist only of α -phase tend to form snarled and unbroken chips and show increased cutting forces. There are studies showing that the machinability of single α -phase alloys could be improved by modification of the microstructure by means of heat treatment conducted prior to machining, aiming to induce a certain amount of β -phase.

In this study, lead-free CW511L alloy was heat treated and water quenched to induce β -phase prior to machining. A subsequent heat treatment with slow cooling was applied to change the microstructure back to α -phase.

Lead-free brass alloys can be single α -phase or duplex α/β -phase materials. Both phases are associated with different properties. The α -phase is known for being soft and ductile, while the β -phase is known to be more brittle and harder [1]. The alloy CW511L consists mainly of α -phase. According to the literature, more brittle β -phase improves machinability, and a duplex structure exhibits better chip breakage than a pure α -structure [1], [2]. The amount of β -phase can be increased by appropriate heat treatment. However, a higher β -content also increases the sensitivity of the alloy to dezincification [3]. Therefore, it is advisable to perform another heat treatment after the machining process to reduce the amount of β -phase.

In this paper, the effect of a heat treatment process, which led to an increase in β -phase content, on machining properties of CW511L alloy, has been investigated. This heat treatment process was based on a study by Toulfatzis et al. [2]. In addition to cutting forces, the shape of the chips, the microstruc-

ture, tensile properties, and dezincification properties have been determined. Furthermore, the influence of subsequent β -annealing on the microstructure, tensile properties, and dezincification has been investigated.

Materials and Methods

In this study, the machining behavior during turning of as-received and heat treated CW511L alloy is compared. In addition, the microstructure, mechanical properties, and the dezincification behavior after different heat treatments were analyzed. The applied heat treatments are listed in Table 1. The material was supplied as an extruded and β -annealed rod with a diameter of 32 mm.

The first heat treatment was performed according to Toulfatzis et al. [2] and Toulfatzis et al. [4] aiming to increase the amount of β -phase and thereby to improve the machinability of CW511L compared to the as-received (AR) condition. The brass was heat-treated at 850°C for 120 min in a preheated Nabtherm N 41/H

chamber furnace and rapidly water quenched. This step was called HT1. HT1 was followed by the subsequent heat treatment (HT2), at 540°C for 180 min followed by slow cooling in air. HT2 was performed to gain back the mainly α -phase microstructure.

For all three conditions, AR, HT1 and HT2 microstructural analysis was performed. Samples were wet ground with SiC foil #320, followed by diamond and OP-S polishing. To perform analysis in a light microscope the samples were etched with a solution of ammonium peroxydisulfate. Additionally, samples were analyzed by means of a scanning electron microscope (SEM) with electron backscatter diffraction (EBSD) techniques to measure the amount of the β -phase.

Tensile tests were performed for all three temper conditions according to NS EN ISO 6892 1. The hardness was measured using a Brinell hardness tester according to ISO 6506-1. Dezincification resistance was investigated according to NS EN ISO 6509.

In the AR and HT1 temper conditions, machining tests were performed. The tests were performed using a Weiler Commodor 230 VDC lathe and a N123H2-0520-0002-BG H10F cutting insert by Sandvik Coromant. Disk-shaped, 2 mm thick specimen were cut by a face-turning operation at a constant cutting speed of $v = 150$ m/min and at different feeds of $f = 0.05; 0.10; 0.16; 0.20$ m/min in dry conditions. The chips were collected after each cut and the cutting forces were measured with a Kistler 9257B dynamometer.

Results and Discussion

The microstructure of the alloy in the three temper conditions is shown in Figure 1, upper row. An overview of alteration in grain size is given in Fig-

Heat treatment	Temperature	Duration	Cooling
HT1	850°C	120 min	Water quenching
HT2	540°C	180 min	Slow cooling in air

Table 1: Heat treatments performed on CW511L

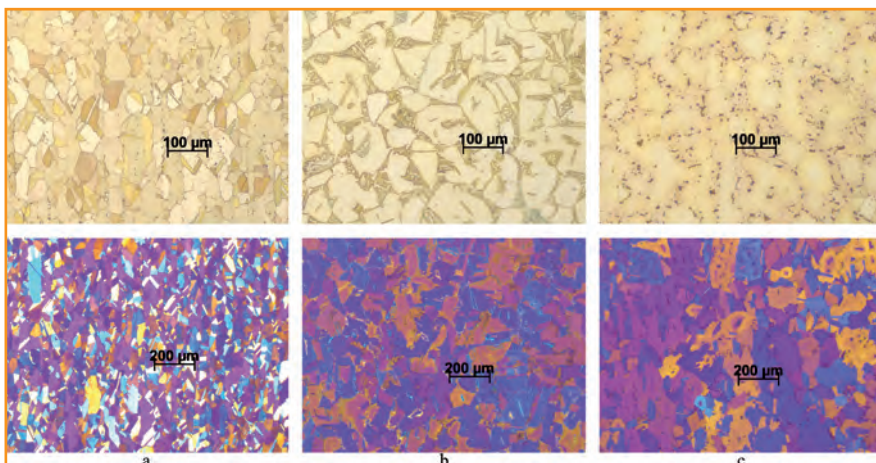


Fig. 1: Microstructure of CW511L in as-received condition (a), after heat treatment HT1 (b), and after heat treatment HT2 (c). Upper row: bright field, bottom row: polarized field pictures.

ure 1, bottom row. The grains in the AR condition are the smallest of all three temper conditions and 3.5% was pre-

hardness of HBW96, the Brinell hardness decreased to HBW67 and HBW62 after heat treatments HT1 and HT2,

Material's temper condition	HBW/2,5/62,5/11			
	1	2	3	Average
AR	96	92	95	94
HT1	66	68	68	67
HT2	61	63	63	62

Table 2: Brinell-hardness measurements of the different conditions

	As-Received AR	Heat Treat- ment HT1	Heat Treat- ment HT2
Tensile strength Rm [MPa]	343	380	318
0,2% proof strength R _{p0,2} [MPa]	315	317	243
Elongation A [%]	47	59	68

Table 3: Tensile test results for the different temper conditions

sent as β -phase in the alloy, see Figure 1a. After heat treatment HT1, 12.6% of the microstructure was presented as β -phase and the grain size increased. After heat treatment HT2, the proportion of β -phase was decreased to 4.8%, while the grains were still larger than in AR condition. Toufatzis et al. [2] reported an increase in β -phase content, in CW511L alloy, from 5% measured in the as received condition to 35% measured after a heat treatment similar to HT1, while grain growth in the α -phase was also noticed.

Changes in grain size and phase-composition influenced the measured hardness, see Table 2. While the material in AR condition shows a

respectively. This can be explained by a larger grain size. The HT1-condition shows a slightly higher hardness due to the presence of a higher amount of β -phase. The minimum value for the Brinell hardness given in NS-EN12164 standard is HBW70, which was not met by HT1 and HT2.

Results of the tensile testing in the three temper conditions are presented in Table 3. While for HT1 the tensile strength and the proof strength were increased compared to the AR condition, they were decreased for HT2. The increased values for HT1 can be explained by the presence of stronger β -phase, while the decreased values for HT2 can be explained by the coarser and mainly α -phase grain structure and thereby more ductile material behavior. The NS-EN12164 standard gives a minimum value of 320 MPa for tensile strength, which is not met by HT2 condition. The fracture elongation increased for HT1 and HT2 compared to the AR condition. This might be caused by the coarser grains. All three conditions showed ductile fracture and necking during the testing, which was most pronounced for the AR condition. The fracture surfaces are shown in Figure 2. All three temper conditions show similar fracture mechanisms with pronounced ductile dimple fracture.

The main cutting force in CW511L in AR and HT1 conditions is almost equal. In HT1 condition, the main cutting force was decreased by 4% compared to the AR condition, see Figure 3. Also, the force ratio, which

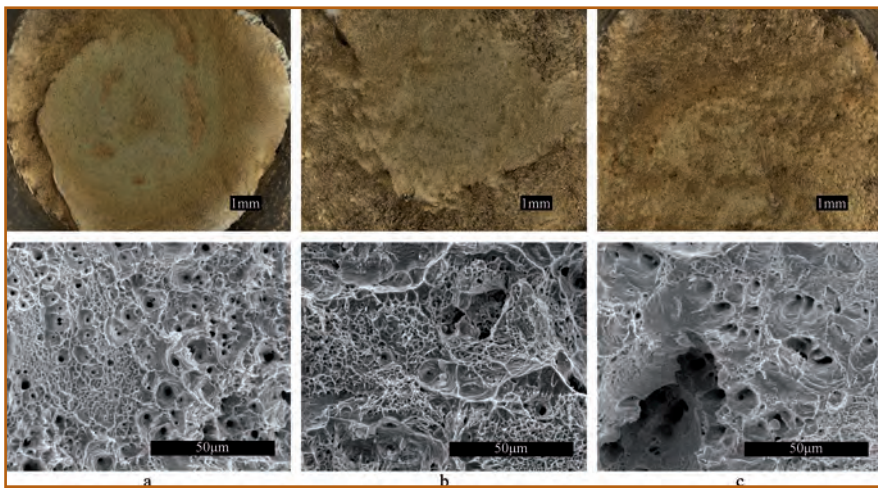


Fig. 2: Fracture surfaces on tensile test bars captured with digital microscope (upper row) and scanning electron microscope (bottom row). a - as extruded, b - heat treatment HT1, c - heat treatment HT2.

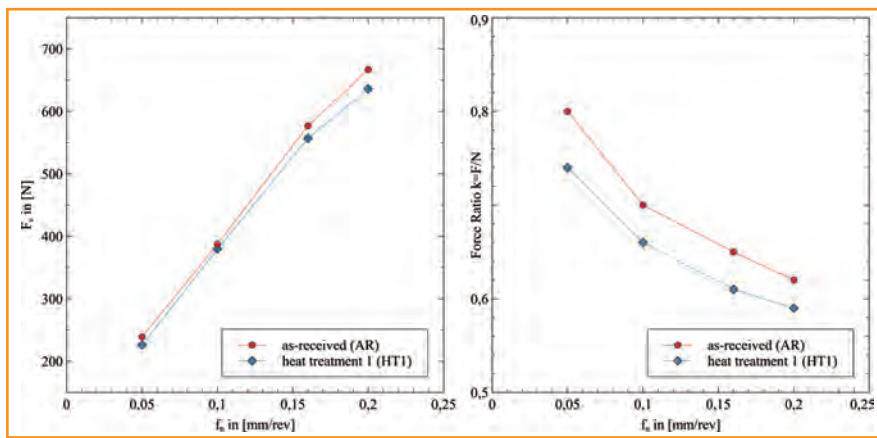


Fig. 3: Main cutting force and force ratio plotted over the feed for CW511L in as-received condition and after heat treatment HT1.

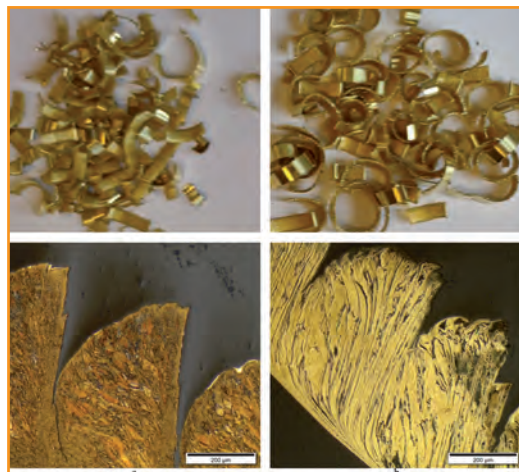


Fig. 4: Comparison between the chips in AR and HT1 condition on macro (top row) and micro scale (bottom row). Chips used in these pictures were produced while cutting with a feed of 0.16 m/min.

is an indicator of the friction in the cutting zone [4], was decreased by 6%. Toulfatzis et al. [5] measured a force reduction of around 3% in a dry turning process using different cutting parameters. Although the β -content was lower compared to Toulfatzis et al. [5] the reduction in cutting forces was slightly higher. This might be due to measurement insecurities or the different cutting conditions, but also to the variance in β content. Toulfatzis et al. [5] additionally measured the power consumption and detected a decrease by 11,25%. Power consumption was not measured in this study, but similar values can be expected. The chip shape and length were equal at macroscopic scale in both conditions. Differences are visible at the microscale, see Figure 4. While the AR condition shows small grains inside

the chips as it is typical for nonhomogeneous chips, the HT1 condition shows elongated grains almost forming lamella, which is typical for discontinuous chips. These changes are similar to those reported by Toulfatzis et al. [5], who additionally noticed a change in chip length on macroscopic scale, where chips were shorter in the heat treated condition. This difference

increased average dezincification depth in transversal direction the alloy is not dezincification resistant after HT1 according to ISO 6509-2, so HT2 is necessary to gain dezincification resistance back. Yet, the dezincification attack was on average twice as deep after HT2 as compared to the AR condition, but it is still considered dezincification resistant according to ISO 6509, see Table 4. This might be due to the increased grain size as discussed by Moriarty et al. [3]. Figure 5 shows micrographs of randomly chosen dezincification attacks in the three different conditions. It is visible, that in the HT1-condition the β -phase is attacked almost exclusively.

Conclusion

Regarding the main cutting force, the heat treatment was not very beneficial, since compared to AR condition only a reduction by 4% was achieved. When evaluating the microstructure of the chips it was visible, that after

Sample ID	No. of Measurements					Average	Max
	1	2	3	4	5		
AR_L*	9	-	-	-	-	<9	
AR_T*	9	-	-	-	-	<9	
HT1_L	132	114	152	144	142	137	152
HT1_T	176	164	116	118	77	130	176
HT2_L	Less than 20					<20	
HT2_T	44	26	29	9	9	23	44

Table 4: Depth of the dezincification attack in the three different conditions of alloy CW511L [μm]

might be caused by different machining parameters used in the study. The dezincification tests showed, the alloy is dezincification resistant in the AR condition and after HT2, see Figure 5 and Table 4. Due to the

HT1 the chips turned from nonhomogeneous chips into discontinuous chips. On the macroscopic scale the length of the chips was not affected. With HT2 the dezincification resistance according to ISO 6509 was

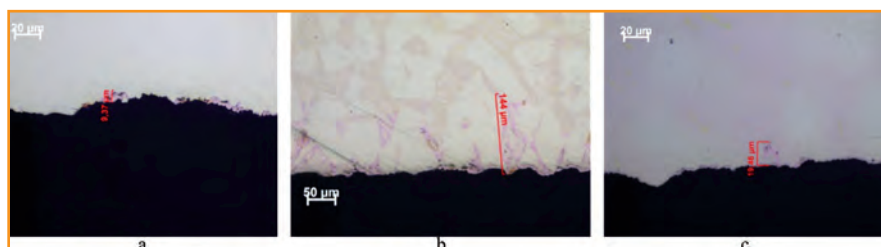


Fig. 5: Dezincification attack in CW511L in the three conditions (a) as-received, (b) after heat treatment HT1, (c) after heat treatment HT2.

retained, but the corrosion attack was slightly deeper compared to the AR condition. Neither HT1 nor HT2 fulfilled the hardness requirement given by NS-EN 12164 standard. HT2 additionally failed to fulfill the tensile strength requirement. A shorter heat treatment before cutting might be more beneficial to both machining, mechanical properties, and dezincification if grain growth would be less significant.

Acknowledgement

The authors thank the Research Council of Norway for supporting this work through the research project LOBUS – Low Lead Brass for Sustainable Com-

munity Development, (RCN Project. No. 296054).

References

- [1] J. R. Davis and ASM International Handbook Committee, *Copper and copper alloys*. ASM International, 2001.
- [2] A. I. Toulfatzis, G. A. Pantazopoulos, and A. S. Paipetis, "Microstructure and properties of lead-free brasses using post-processing heat treatment cycles," *Mater. Sci. Technol. (United Kingdom)*, vol. 32, no. 17, pp. 1771–1781, Nov. 2016, doi: 10.1080/02670836.2016.1221493.
- [3] M. Moriarty, Y. Wu, T. Murray, and C. Hutchinson, "The effect of phase fraction, size and shape on the dezincification of duplex brasses," *Corros. Sci.*, vol. 184, p. 109366, May 2021, doi: 10.1016/j.corsci.2021.109366.
- [4] P. Albrecht, "New developments in the theory of the metal-cutting process: Part I. the ploughing process in metal cutting," *J. Manuf. Sci. Eng. Trans. ASME*, vol. 82, no. 4, pp. 348–356, Nov. 1960, doi: 10.1115/1.3664242.
- [5] A. Toulfatzis, G. Pantazopoulos, C. David, D. Sagris, and A. Paipetis, "Final Heat Treatment as a Possible Solution for the Improvement of Machinability of Pb-Free Brass Alloys," *Metals (Basel)*, vol. 8, no. 8, p. 575, Jul. 2018, doi: 10.3390/met8080575.

(1) *Magdalena S. Müller, Knut Sørby, Department of Mechanical and Industrial Engineering, Norwegian University of Science and Technology, 7491 Trondheim, Norway*

(2) *Stanka Tomovic Petrovic, Department of Materials Technology, SINTEF Manufacturing AS, 2831 Røa, Norway*

Distribution of alloying elements and measurable shape memory effect of continuous cast copper aluminum alloy

Schelnberger, B.; Kranner, C.; Krieg, R.; Theiß, R.; Dültgen, P. (1)

Cu-based shape memory alloys (SMA) can exhibit excellent shape memory properties, e.g. strain recovery. Combining that with high phase stability up to 200 °C, CuAlNi alloys have been investigated as an alternative to NiTi alloys as an actuator material. However, most CuAl SMA tend toward intergranular cracking and brittle material behavior when in a polycrystalline state, limiting their industrial utilization so far.

Continuous casting is widely used in copper alloy manufacturing. With modifications to machine design and casting parameters, it enables the fabrication of a specific microstructure in CuAl alloys, with improved mechanical properties under cyclic stress, during casting.

To achieve this, additional knowledge about the thermochemical state of the alloy during casting and its influence on the resulting grain structure should be sought. This work represents a first step, concerning the chemical composition of the cast material, which is the dominant factor in controlling the phase composition and transformation temperatures of the SMA.

State of the Art

CuAl-based SMA are prone to intergranular cracking due to a combination of elastic anisotropy of the parent β phase and transformation strain due to stress-induced martensite, with the latter being magnitudes greater in effect.[RPRB04, SaSh86]. This phenomenon results in reduced ductility and brittle behavior, limiting mechanical processing, as well as greatly reduced shape recovery (of less than 5 %) and cyclic stability of the shape memory effect [SBLT14]. The effect of transformation incompatibility during martensite formation has been repeatedly demonstrated in other Cu-based SMA, like Cu-Zn-Al, as well [UeSc12, UeSc13]

Research on microstructure optimization of Cu-based SMA has focused on a decrease in grain boundary density and a specific alignment of grain boundaries, as well as grain orientation, with load direction [SOKI02, SOYO05]. While texture reorientation through thermomechanical processing has produced significant increases in shape memory strains [SLRB12], the highest recoverable strains when dis-

regarding single-crystals, have been reported for bamboo-like grain structure and columnar-grained structure with [001] oriented grains, reaching up to 10 % [XiLH15, XKXH19]. While the former structure has been achieved by continuous [TQRS15, UeSc12] or cyclic heat treatment [OKKO13], by local remelting and by fiber casting [TuSc16], the latter is mainly formed through unidirectional solidification in continuous casting, utilizing an adapted Ohno Continuous Casting (OCC) process [Ohno86, WaHX11, FSZZ16, LCHX17]. Columnar-grained

CuAlMn has also proven to be suitable for hot-rolling, retaining superelastic strains of up to 7 % after heat treatment while displaying a strong texture orientation [LCHX17].

Extending the OCC process to industrial-scale casting of Cu-based SMA, the aim of this and subsequent work is to identify process parameters for the reliable fabrication of unidirectionally solidified CuAlNi with consistently high shape recovery.

Methods

Fabrication

Casting materials were prepared from pure elements, except when remelting the material from a prior casting, where noted. Casting was performed on a TOPCAST TCC15-1400cc continuous casting machine with a vacuum induction furnace and induction-heated graphite die with an inner diameter of 15 mm. The different compositions are an adjustment in reaction to the high overall aluminum content in castings A.1 to A.3. The stacking of the alloying elements in the crucible follows the configurations in Figure 1. Due to the unavoidable reduced heating

Casting No.	Composition (weighed)	T _{hom} [°C]	t _{hom} [s]	T _{cast} [°C]	v _{cast} [mm/s]	Element stacking (bottom-top)
A.1	Cu _{82.35} Al _{13.65} Ni ₄	1480	3000	1300	3.3	Al-Cu-Ni
A.2	Cu _{82.35} Al _{13.65} Ni ₄	1450	600	1400	2.5	Al-Cu-Ni
A.3	Cu _{82.35} Al _{13.65} Ni ₄	1480/1300	300/300	1300	2.5	Al-Cu-Ni
B.1	Cu _{82.6} Al _{13.3} Ni _{4.1}	1480	900	1300	5.45*	Cu-Al-Ni
B.2	Cu _{82.6} Al _{13.3} Ni _{4.1}	1480	1800	1200	2.5	Cu-Al-Ni
B.3	Cu _{82.6} Al _{13.3} Ni _{4.1}	1480	1800	1200	3	Cu-Al-Ni

Table 1: Crucible loading and casting parameters; *Noticeable heating of strand below rolling unit

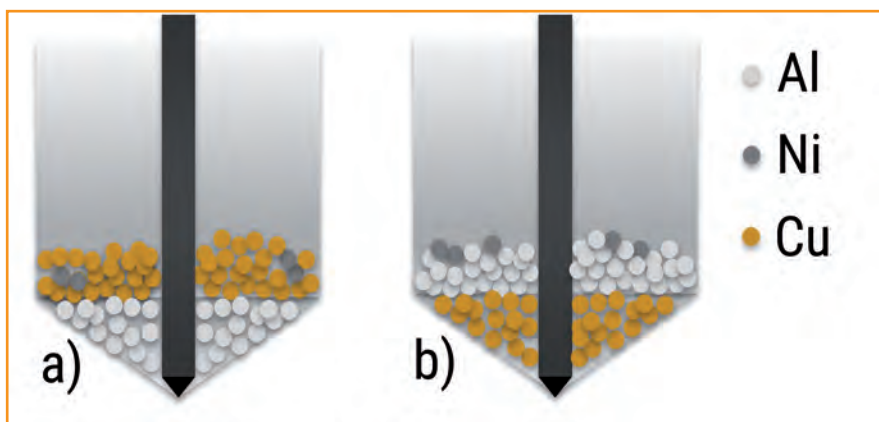


Fig. 1: Element stacking in the crucible, castings A.1 to A.3 (a) and B. to B.3 (b), resp.



Fig. 2: Colour difference in initial casting

in the lowest part of the crucible, the nickel granules were placed on top of the other elements to maximize their heating before the remaining metals melt. The melting process was started with 4 cycles of evacuation to 100 mbar and subsequent washing with argon gas to minimize atmospheric

oxygen in the furnace. After holding for t_{hom} at the homogenization temperature T_{hom} , the temperature was decreased to the casting temperature T_{cast} (Table 1) and casting started with stepwise pulling at an effective velocity v_{cast} . The cast strand was cooled with a water spray approximately

100 mm below the opening of the die. It should be noted that casting A.2 was performed by remelting the cast material from casting A.1, to increase the homogeneity. Casting A.3 is fabricated from remelted cast material in the same way. Intermittent removal of the cast strand was performed by cutoff grinding.

Preparation & Analysis

Samples were prepared by wet cutting, in 50 mm steps for [x].1-samples and approx. 1100 mm for the sample groups 1-5, and ground before EDX measurements (see Figure 15). Metallographic samples were ground, and polished (to 1 μm), followed by etching polishing with OP-S (0.25 μm) mixed with H_2O_2 and HN_3 . Heat treatment consisted of homogenization at 850 °C for 30 mins in a tube furnace, followed by ice-water quenching. DSC samples were prepared from heat-treated material by diamond wire-cutting to thin plates and manual grinding to reduce samples to a suitable size for the DSC crucibles. The final sample weight varied between 10 and 30 mg.

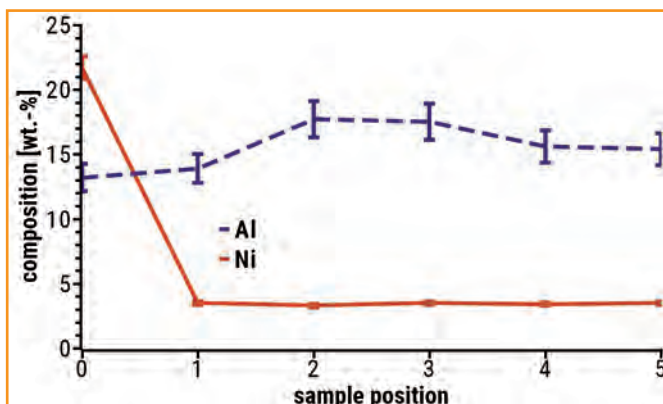


Fig. 3: Casting A.1, averaged composition, sample positions 0 - 5

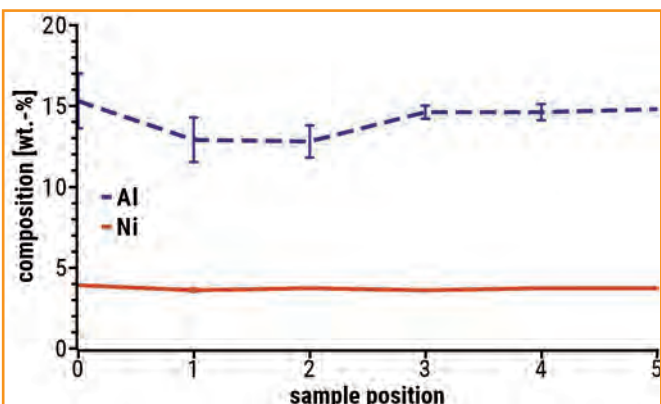


Fig. 4: Casting A.2, averaged composition, sample positions 0 - 5

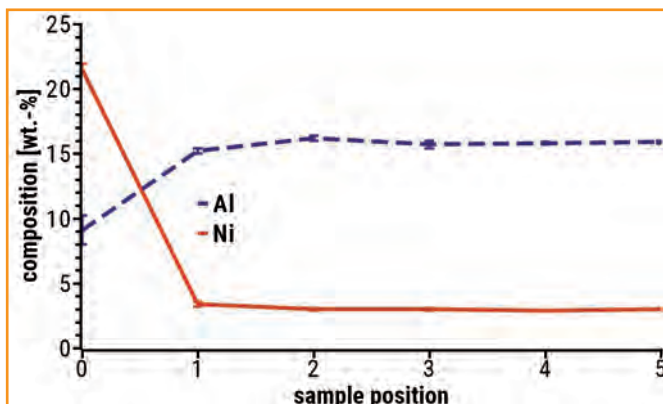


Fig. 5: Casting A.3, averaged composition, sample positions 0 - 5

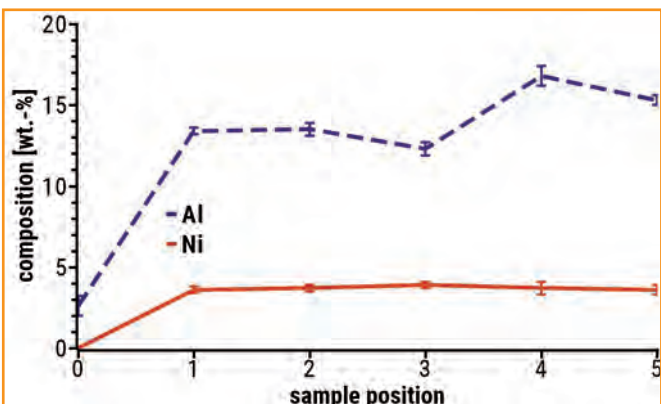


Fig. 6: Casting B.1, averaged composition, sample positions 0 - 5

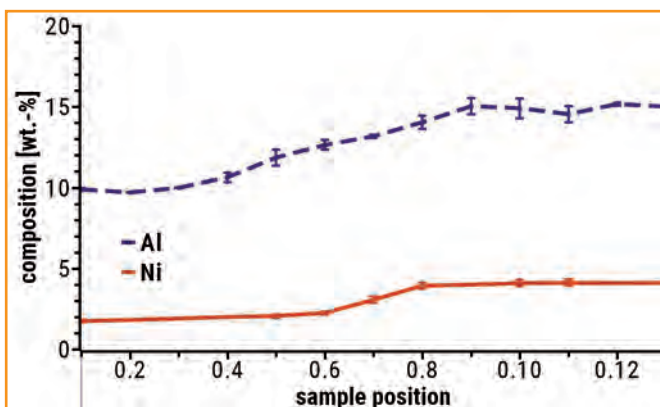


Fig. 7: Casting B.2 averaged composition, sample positions 0.1-0.13 (0-60 mm)

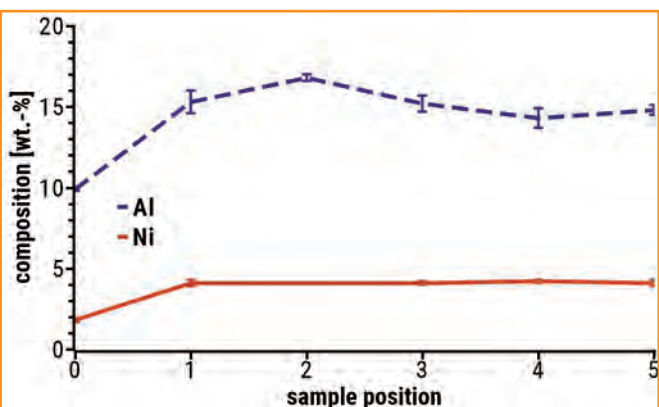


Fig. 8: Casting B.2 averaged composition, sample positions 0-5 (0-60 mm)

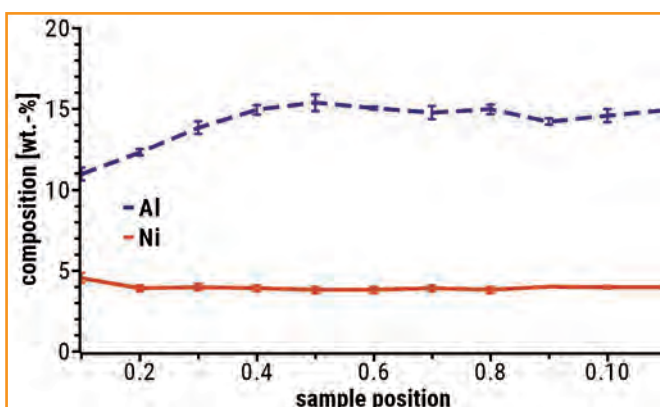


Fig. 9: Casting B.3 averaged composition, sample positions 0.1-0.13 (0-600 mm)

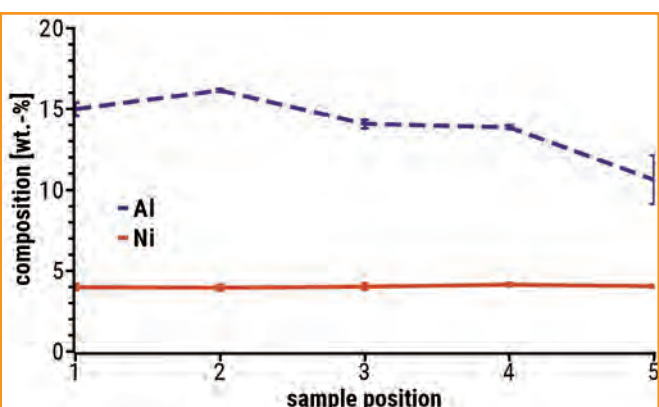


Fig. 10: Casting B.3 averaged composition, sample positions 0-5 (0-600 mm)

EDX measurements for composition were performed on a scanning electron microscope at 20 kV, a working distance of 22 mm and a magnification of 200.

DSC measurements were performed on a Netzsch 214 Polyma differential scanning calorimeter with Argon as a protective gas, a heating and cooling rate 10 K/min and maximum temperatures of 180 °C for quenched samples.

Results

Castings developed excessive cavities depending on casting parameters, as shown in Figure 17. These appear as pores that are distorted toward the casting direction and the middle of the strand. To achieve cavity-free castings, casting temperatures of 1250 °C or less and casting velocities of 2,5 mm/s or more have been chosen for castings B.2 and B.3. At the same time, casting velocity should be kept at 3.5 mm/s or less, with close monitoring of the cooling zone, due to insufficient heat removal through the spray cooling at higher velocities.

EDX measurements show the stacking order of the pure elements as having a great influence. The EDX measurements on the castings of A.1 and A.3 confirm the optical impression of very high Ni content in the initial part of the casting (up to 22 %) when compared to the intended composition (Figure 2). The Ni content is homogeneous for castings B.2 and B.3 only. At the same time, the initial sample of casting A.3 contains 9 % Al, whereas the other samples show a more uniform Al content of 15 % - 16 %. The effect is detectable, but much reduced in casting A.1, with initially 13 % compared to 15 % - 18 % in the remaining casting. Casting A.2 displays a noticeably opposite relationship, with an initial Al content of 15.5 % dropping below 13 % in the next sample position (Figure 3 to Figure 5).

In castings B.1 to B.3, Ni and Al content in samples from the beginning of the casting are generally lower than in the remaining material. The detailed

analysis of castings B.2 and B.3 shows a gradual increase of the Al content from 10 % to 15 % and 11 % to 15 %, respectively, and a decrease toward the final sample position. Ni reaches a plateau of approximately 4 % after 400 mm and 5 mm respectively, without further decrease. Casting B.1 confirms these findings largely but shows very low levels of both Al and Ni content at the first sample position. Additionally, in the case of casting B.2, there appears to be a noticeably divergent melt composition present in samples 0.1 to 0.6, which was found in several measurements at the edge of the cut samples (Figure 11).

DSC analysis confirms a martensite-austenite transformation in the heat-treated material. The peak shapes generally conform to those of CuAlNi of the same composition and preparation from earlier works by the same authors (Figure 16) [SRTD21]. The presence of β_1' - and γ_1' -martensite in the metallographic analysis supports this (Figure 12, the DSC results show a low variation of martensite

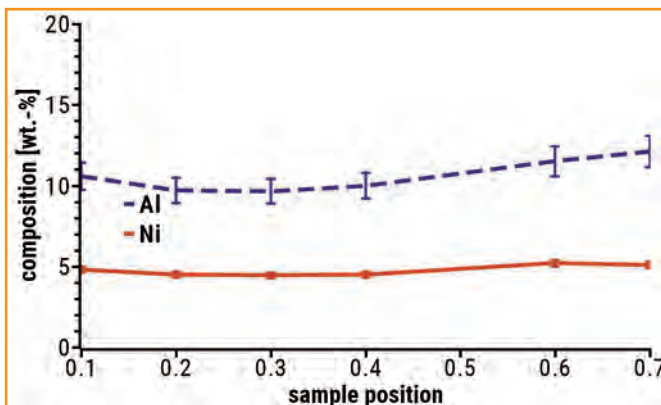


Fig. 11: Casting B.2 composition of residual material, sample positions 0-70 mm

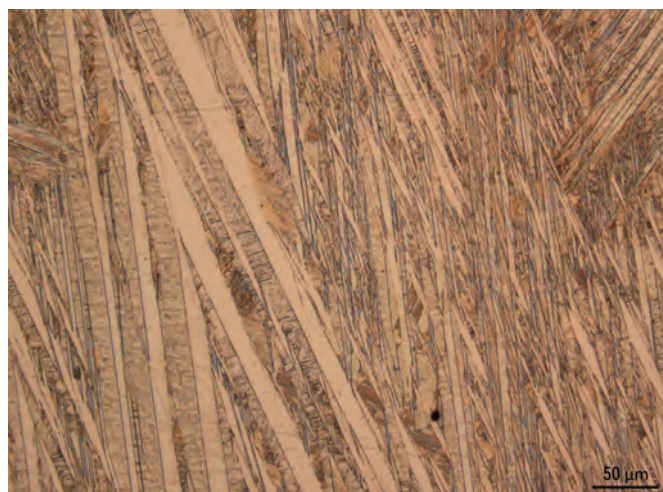


Fig. 12: Optical micrograph of casting B.3, sample position 2, 200x magnification

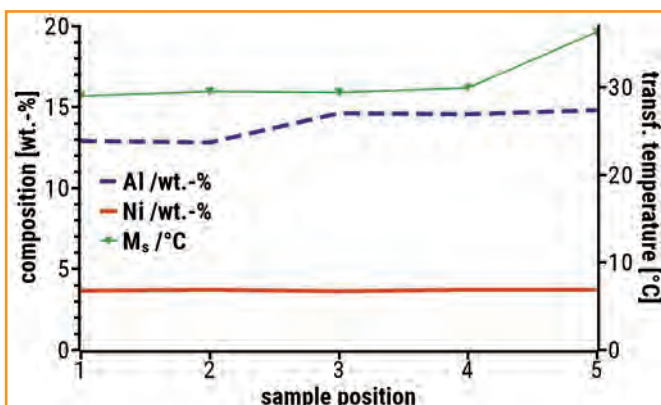


Fig. 13: Casting B.2 composition of residual material, sample positions 0-70 mm

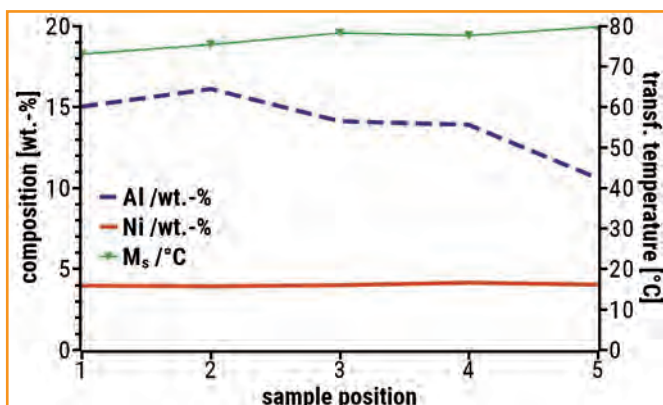


Fig. 14: Casting B.3, comparison of martensite-start temperature and composition along the casting

start temperature, M_s , for castings B.2 and B.3, with casting A.1 displaying a moderate 10 K maximum difference between all samples.

Discussion

The morphology of the observed pores in some castings is alike to the common shape of the “mushy” zone in continuous casting. Lowering the temperature casting temperature and increasing the casting velocity decreases the solidification time, while simultaneously increasing the local temperature gradient, thus modifying the solidification morphology and reducing the formation of pores.

The DSC results indicate a significant effect of both the stacking order of the alloying elements and the holding time during homogenization. Comparison of castings A.1, A.2, and A.3 confirms the latter, with A.3 having

an increased Ni content and reduced Al content in the initial sample, to a greater extent than observed in A.1. This is most likely caused by density segregation of the elements when melting, which is diminished over time through the convection and gradual solution of the alloying elements in copper. Notably, the same inhomogeneities were not observed in a different casting machine with higher power to melt volume ratio, at significantly lower melting times. While remelting was effective in reducing the inhomogeneities, most noticeably those of the Ni content, comparison of A.2 and A.3 suggests that the homogenization time is the main influence factor.

The casting machine may retain small amounts of solidified metal in the die after the casting process, which is melted and removed with the first portion of the next casting. In the case of

casting B.1, there had been a prior casting of pure copper. It seems plausible that residual metal has melted and flowed into the die before the stopper was released to let the new melt into the die.

Sufficient homogenization times should be applied, to ensure that mixing and solution of the alloying elements takes place above the respective melting temperatures. This also avoids process safety issues, as preliminary work revealed considerable risk of machine blockage due to unexpectedly high melting points for Ni-enriched melt.

However, reasonable holding times may not be sufficient to guarantee homogeneous conditions in the initial section of the casting. Therefore, at least 400 mm should be removed for separate analysis. Further, additional improvements to the vacuum level and reduction of residual oxygen are

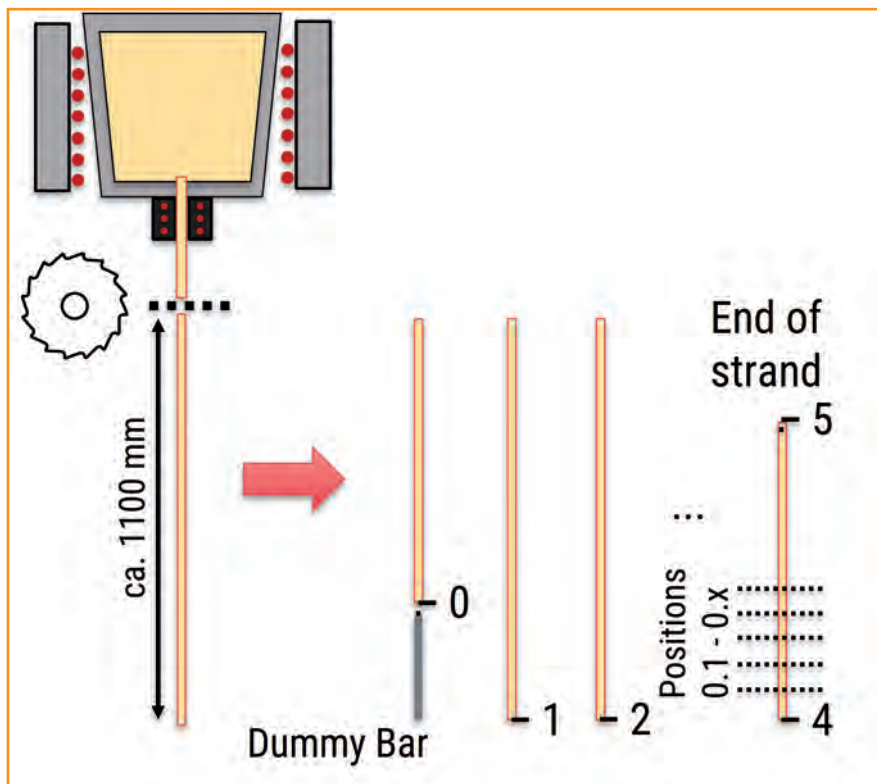


Fig. 15: Sample positions as determined by the length and cutting of the cast strand

technically feasible. This would greatly reduce the loss of Al and Cu to slag components and the subsequent deviation from the initial composition. Nevertheless, both effects (density segregation and loss by atmosphere or crucible reactions) should be quantified in a model for the expected deviation of the overall composition and an appropriate correction of the weighed-in amounts of alloying elements applied.

Conclusion

Dependencies between the stacking of the alloying elements, the casting parameters and the quality and homogeneity of continuous cast CuAlNi have been found, with the homogenization prior to casting having the greatest effect on overall

homogeneity. Disregarding deviations in the initial part of the cast, the composition was sufficiently homogeneous to result in less than 10 K of differences in transformation temperatures. These could be improved upon by an order of magnitude in the future, given additional resources to employ high-vacuum processing. This is a strong argument for Cu-based SMA over NiTi SMA, due to the latter's transformation temperatures being much more sensitive to composition. Lowered demands on precise composition control make Cu-based SMA a much more accessible material for manufacturers and users alike.

Further work will assess the effect of a reducing gas atmosphere, e.g., forming gas, to decrease the influence of oxidization on the material homogeneity. Following that, adjustments to the cooling system could increase the range of viable casting parameters and allow an analysis of the effect of higher temperature gradients along the strand on the microstructure of the casting.

Acknowledgements

This research was supported by the Federal Ministry for Economic Affairs

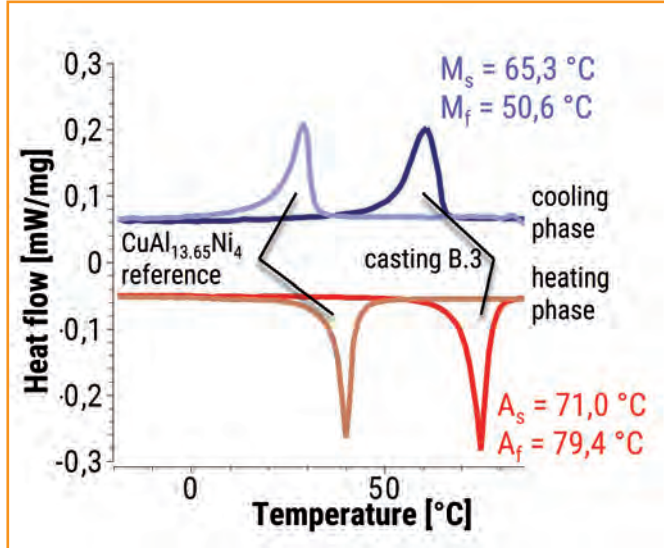


Fig. 16: Casting B.3sample position 4, analysis of DSC measurement

Fig. 17: 17 porosity, cut in casting direction (A.1), center axis marked by dotted red line

and Climate Action. The authors thank Mr. Holm and Mr. Horn for their assistance in metallographic procedures.

References

- [FSZZ16] FU, HUADONG ; SONG, SHILEI ; ZHUO, LONGCHAO ; ZHANG, ZHIHAO ; XIE, JIANXIN: Enhanced mechanical properties of polycrystalline Cu-Al-Ni alloy through grain boundary orientation and composition control. In: Materials Science and Engineering: A Bd. 650 (2016), S. 218–224
- [LCHX17] LIU, JI-LI ; CHEN, ZHI HONG ; HUANG, HAI-YOU ; XIE, JIAN-XIN: Microstructure and superelasticity control by rolling and heat treatment in columnar-grained Cu-Al-Mn shape memory alloy. In: Materials Science and Engineering: A Bd. 696 (2017), S. 315–322
- [Ohno86] OHNO, A.: Continuous Casting of Single Crystal Ingots by the O.C.C. Process. In: JOURNAL OF METALS (1986)
- [OKKO13] OMORI, TOSHIHIRO ; KUSAMA, TOMOE ; KAWATA, SHINGO ; OHNUMA, IKUO ; SUTOU, YUJI ; ARAKI, YOSHIKAZU ; ISHIDA, KIYOHITO ; KAINUMA, RYOSUKE: Abnormal Grain Growth Induced by Cyclic Heat Treatment. In: Science Bd. 341 (2013), Nr. 6153, S. 1500–1502
- [RPRB04] RECARTE, V ; PÉREZ-LANDAZÁBAL, J.I ; RODRÍGUEZ, P.P ; BOCANEGRAS, E.H ; NÓ, M.L ; SAN JUAN, J: Thermodynamics of thermally induced martensitic transformations in Cu-Al-Ni shape memory alloys. In: Acta Materialia Bd. 52 (2004), Nr. 13, S. 3941–3948
- [SaSh86] SAKAMOTO, HIDEKAZU ; SHIMIZU, KEN&RSQUO;ICHI: Analytical Investigation on Cyclic Deformation and Fatigue Behavior of Polycrystalline Cu-Al-Ni Shape Memory Alloys above M_{s} . In: Transactions of the Japan Institute of Metals Bd. 27 (1986), Nr. 8, S. 601–607
- [SBLT14] SADE, MARCOS ; BUBANI, FRAN ; LOVEY, FRANCISCO ; TORRA, VICENÇ: Effect of grain size on stress induced martensitic transformations in a Cu-Al-Be polycrystalline shape-memory alloy. Pseudoelastic cycling effects and microstructural modifications. In: Materials Science and Engineering: A Bd. 609 (2014), S. 300–309
- [SLRB12] SOBRERO, C.E ; LA ROCA, P. ; ROATTA, A. ; BOLMARÓ, R.E ; MALARÍA, J.: Shape memory properties of highly textured Cu-Al-Ni-(Ti) alloys. In: Materials Science and Engineering: A Bd. 536 (2012), S. 207–215
- [SOKI02] SUTOU, Y. ; OMORI, T. ; KAINUMA, R. ; ISHIDA, K. ; ONO, N.: Enhancement of superelasticity in Cu-Al-Mn-Ni shape-memory alloys by texture control. In: Metallurgical and Materials Transactions A Bd. 33 (2002), Nr. 9, S. 2817–2824
- [SOYO05] SUTOU, Y. ; OMORI, T. ; YAMAUCHI, K. ; ONO, N. ; KAINUMA, R. ; ISHIDA, K.: Effect of grain size and texture on pseudoelasticity in Cu-Al-Mn-based shape memory wire. In: Acta Materialia Bd. 53 (2005), Nr. 15, S. 4121–4133
- [SRD21] SCHELNBERGER, BENJAMIN ; ROJ, ROBIN ; THEISS, RALF ; DÜLTGEN, PETER ; GHOLAMI-KERMANSHAH, MOZHGAN: Effects of abnormal grain growth on shape memory characteristics of Cu-Al-Mn alloys. In: International Conference and Exhibition on New Actuator Systems and Applications GMM Conference, February 17–19, 2021,, 2021
- [TQRS15] TUNCER, NIHAN ; QIAO, LEI ; RADOVITZKY, RAUL ; SCHÜH, CHRISTOPHER A.: Thermally induced martensitic transformations in Cu-based shape memory alloy microwires. In: Journal of Materials Science Bd. 50 (2015), Nr. 22, S. 7473–7487
- [TuSc16] TUNCER, NIHAN ; SCHÜH, CHRISTOPHER A.: Melt-cast microfibers of Cu-based shape memory alloy adopt a favorable texture for superelasticity. In: Scripta Materialia Bd. 117 (2016), S. 46–50
- [UeSc12] UELAND, STIAN ; SCHÜH, CHRISTOPHER: Superelasticity and fatigue in oligocrystalline shape memory alloy microwires. In: Acta Materialia Bd. 60 (2012), S. 282–292
- [UeSc13] UELAND, STIAN M. ; SCHÜH, CHRISTOPHER A.: Grain boundary and triple junction constraints during martensitic transformation in shape memory alloys. In: Journal of Applied Physics Bd. 114 (2013), Nr. 5, S. 053503
- [WaHX11] WANG, YU ; HUANG, HAI-YOU ; XIE, JIAN-XIN: Texture evolution and flow stress of columnar-grained polycrystalline copper during intense plastic deformation process at room temperature. In: Materials Science and Engineering: A Bd. 530 (2011), S. 418–425
- [XiLH15] XIE, JIAN-XIN ; LIU, JI-LI ; HUANG, HAI-YOU: Structure design of high-performance Cu-based shape memory alloys. In: Rare Metals Bd. 34 (2015), Nr. 9, S. 607–624
- [XKXH19] XU, SHENG ; KUSAMA, TOMOE ; XU, XIAO' ; HUANG, HAIYOU ; OMORI, TOSHIHIRO ; XIE, JIANXIN ; KAINUMA, RYOSUKE: Large [001] single crystals via abnormal grain growth from columnar polycrystal. In: Materialia Bd. 6 (2019), S. 100336
- (1) Schelnberger, B.; Kranner, C.; Krieg, R.; Theiß, R.; Dültgen, P., Forschungsgemeinschaft Werkzeuge und Werkstoffe e.V., Paperberger Str. 49 | 42859 Remscheid | Germany

Corrosion susceptibility of the CuZn35Pb1,5AlAs (CW625N) brass alloy in various environments

Tomovic-Petrovic, S. (1); Gulbrandsen-Dahl, S. (1); Wenner, S. (2)

Corrosion sensitivity of the CW625 brass alloy during exposition to the sea water (field test) and to drinking water (rig test with cooled water circle), over a time span of six and two years respectively, has been evaluated. Forged and machined couplings were selected to be exposed to the sea water while tubes manufactured through an extrusion/machining processing route were applied in the rig test. Evaluation is based on a systematic measuring of the depth of corrosion observed in the test articles. The tests have revealed dezincification as the dominating corrosion form in couplings, but intergranular corrosion (IGC) was a main corrosion form in the tubes. To understand the mechanism behind the IGC observed in the beta annealed alloy, a systematic investigation of the corrosion products and chemistry that occurred along the grain boundaries has been performed by scanning/transmission electron microscopes (STEM).

Brass is a material which, due to its superior workability, mechanical strength, and good general corrosion resistance, has been traditionally used in applications, which assume contact with water. Corrosion resistance of brass is to some extent explained by nobility of copper. [1] In spite of a good general corrosion resistance, brass alloys may suffer from certain degradation when they are exposed to a specific environment. Dezincification and IGC are the two most often met degradation/corrosion forms in leaded, 2-phase (α/β) brass alloys in contact with water. Optimisation of the alloy's chemical composition and microstructure is a common strategy for improvement of its corrosion resistance. Elements such as arsenic, phosphorous or antimony are known for their corrosion-inhibiting effect in brass. [2] However, these elements are soluble only in the α -phase and not in the β -phase. In such a way, they protect the α -phase from dezincification while the β -phase, prone to corrosion, remains as a potential corrosion initiation point. Therefore, the imperative in production of 2-phase brass is to reduce the volume fraction of the beta phase and form a non-continuous β -phase network in the microstruc-

ture. This is possible to obtain either through a balanced thermomechanical production process or in a dezincification resisting (DZR) treatment as a last step in the production process. [3] Environment is an important factor that affects the corrosion behaviour of brass alloys. Literature data show that a presence of clean water and/or moisture should be enough for the initiation of corrosion of some brass alloys [4,5]. Furthermore, a low concentration of ammonium [6,7], chlorides [8], fluorides [9] and molibdates [10] significantly increase water corrosivity. In this regard, investigation of effect of different environments on corrosion resistance of brass is high valuable in assessing suitability of a material for an application.

Intention with this paper is to present results of two long-term corrosion tests, field test and rig test, performed on CW625 brass alloy including the

results of investigation of grain-boundary phenomena occurred in the samples applied in the mentioned tests by use of (SEM/TEM).

Experimental procedures

Characterisation of the materials as delivered, prior to the corrosion test

The test articles for the field test were brass couplings of different geometry, produced through the processing route extrusion/forging/machining (Figure 1 a-c). In the rig test the test articles were tubes of 17 mm diameter and 50 mm length, produced from an extruded and DZR treated rod, through the processing route extrusion/machining (Figure 1 d).

Forgings selected out from the batch applied in the field test as well as the extruded rod supplied for manufacturing of the tubes examined in the rig test have been characterized prior to corrosion tests start.

The chemical composition of the forgings has been analysed by optical emission spectrometry, while the chemical composition of the tubes' material is based on certificate delivered by supplier of the extruded rod. Metallographic preparation including etching in Amoniumperoxodisulphate was applied on representative samples of each test article for characterisation of the microstructure by optical microscopy.

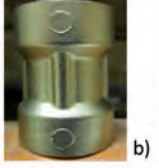
ID	Field test			Rig test
	28	14	35	
Test article	 a)	 b)	 c)	 d)

Fig. 1: Test articles with assigned ID

		Cu	Zn	Pb	As	Fe	Ni	Sn	Al	Mn	Si	P
Spec.	Min	63,0	Rem	1,2	0,04				0,50			
	Max	64,0	Rem	1,6	0,08	0,10	0,2	0,3	0,60	0,10		
Forgings	28	63,3	34,4	1,4	0,08	0,09	0,03	0,09	0,51	0,00	0,01	0,003
	14	63,9	33,9	1,3	0,05	0,09	0,03	0,05	0,54	0,00	0,01	0,009
	35	63,5	34,3	1,4	0,07	0,09	0,02	0,09	0,53	0,00	0,01	0,003
Tube		63,80	34,2	1,3	0,04	0,08	0,02	0,09	0,52	0,01	0,01	-

Table 1: Chemical composition, [wt. %]. The CW625 specification limits are given in the top rows.

A part of the initial characterisation was dezincification test according to ISO 6509-1.

Evaluation of the corrosion sensitivity

Two long-term corrosion tests have been conducted in order to follow behaviour of the CW625 alloy concerning corrosion sensitivity when exposed to different environments. The first one is a field test, organized by ISIFLO AS, Norway, where the selected test articles have been immersed in the sea water at three different locations along the Norwegian coast. The test went on over a time span of six years. A certain number of the test articles were picked out from each location once per year and examined for corrosion.

The second test was a two years long test performed in the test rig of Dessau-Ost waterworks with a cooled water circle. The drinking water applied in the test was analysed every two weeks for pH (7,7), electrical conductivity (739 [$\mu\text{S}/\text{cm}$]) as well as concentration of chloride (53 [mg/L]) and sulphate (158 [mg/L]), with numbers in parentheses being the mean values. Twice per year, a certain number of the tubes were dismantled from the system and examined for corrosion.

Corrosion depth has been measured on the polished, longitudinal sections through the exposed surface, covering the entire length of the test article. One section has been prepared per coupling and two sections per tube (along the upper and the lower tube half). Measuring was performed at SINTEF Manufacturing's laboratory, Norway by using an optical microscope. Measuring step was

2 mm along the coupling sections and 1 mm along the tube sections.

A FEI Helios G4 UX SEM/focused ion beam (FIB) instrument was used for surface imaging and TEM sample extraction from the tube after 6 months of drinking water exposure. Scanning transmission electron microscopy (STEM) and energy-dispersive X-ray spectroscopy (EDS) mapping was conducted using a JEOL JEM-2100F microscope. Compositional quantification of the EDS spectra was done using the Cliff-Lorimer method with absorption corrections.

Results and discussion

Chemical composition

Chemical composition of the test materials is given in Table 1.

Microstructure and dezincification test

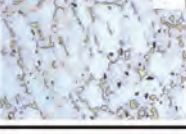
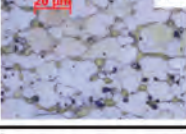
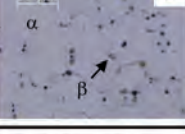
Microstructure in the couplings is shown in Figure 2 a-c. An α/β microstructure was found in each article. A certain variation in the β volume fraction was observed, which is usually associated to the thermomechanical processing history combined with different article geometry. Microstructure in the extruded rod is shown

in Figure 2 d. This consists of mainly α -phase with a small amount of well distributed β -grains. The spherical dark particles are lead inclusions.

A part of the initial characterisation was dezincification test according to ISO 6509-1. Average and max corrosion depth measured both across and along the axes are given in Figure 2.

Evaluation of the corrosion sensitivity

The batch of the test articles picked up from one location, after 6 years being immersed into the sea water is shown in Figure 3 a). Figure 3b) shows the tube after 2 years being assembled in the Dessau Ost waterworks, split into the upper and lower halves. A visual inspection of the overall surface of the couplings and the inner surface of the tubes revealed homogeneous light to dark brown surface layer with bulky greenish-blue corrosion products. A combination of dezincification (reddish corrosion product) and intergranular corrosion (cracks along the grain boundary) have been observed by means of a light microscope in both articles, see Figure 4 a) and b). However, dezincification was found as the dominating corrosion form in the couplings while the tubes were more prone to IGC. Different patterns

ID	Field test			Rig test
	28	14	35	
Microstructure				
DZ* [μm]	T-22 (27); L-39 (54)	T-19 (29); L-21 (36)	T-45 (65); L-68 (102)	T-7 (13); L-13 (19)

* Dezincification depth measured across (T) and along (L) the axes

Fig. 2: Microstructure and dezincification depth measured in the test articles

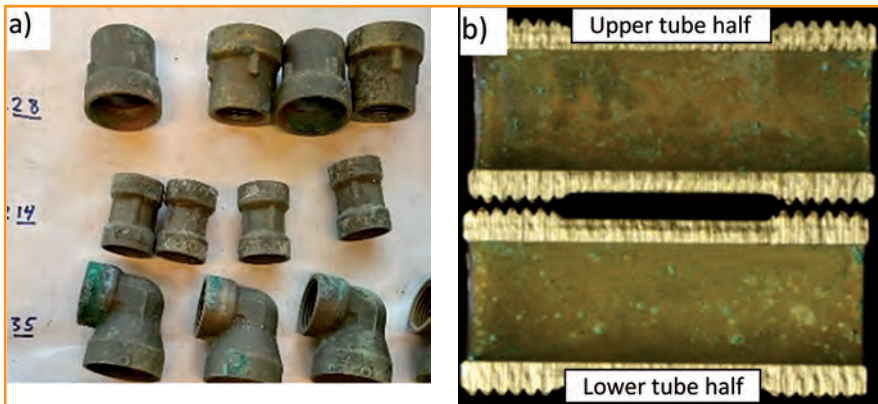


Fig. 3: Test articles after exposing to the sea water (a) and testing in the test rig at Dassau-Ost (b)

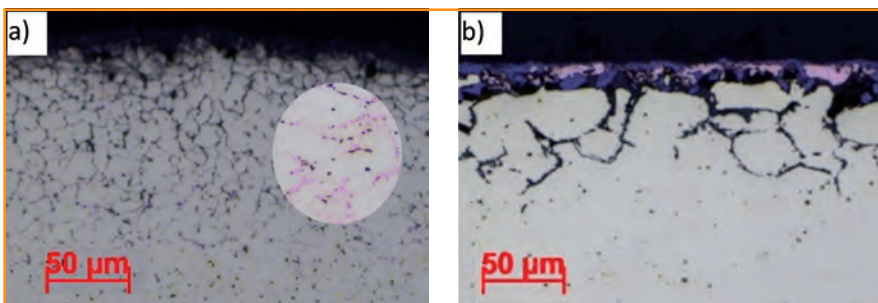


Fig. 4: Corrosion form in the couplings (a) and tubes (b)

of the corrosion observed in couplings and tubes (Figure 4) come from a difference in grain size in the forged coupling (small grains) and extruded/machined tube (large grains).

After six years in the sea water, the general corrosion depth measured in the couplings was up to 150 mm (approx. 25 μm per year) with local peaks up to 730 μm (approx. 120 μm per year), Figure 5. The peaks usually coincided with the bulky green corrosion products area. In addition, the

machined surface seems to be more prone to corrosion initiation than the original, forged surface.

General corrosion depth in the tubes was measured up to 120 μm (approx. 60 μm per year) with some peaks up to 400 μm (approx. 200 μm per year), Figure 6. The peak values were mainly measured toward the ends of the tubes where some erosion was observed. The erosion might point to the water turbulence in the system.

The mechanism behind the corrosion of the tube applied in the rig test

To understand the mechanism behind the corrosion process, which occurs in the tubes applied in the rig test, a part of the tubes, its inner (corroded) surface, was observed with SEM, Figure 7. The surface is covered with two layers oxide. The first one is so called ‘upper’ oxide i.e., patches composed of organic molecules and oxides of Zn, Al, Si, Ca. The second one is called ‘lower’ oxide consisting of pure copper oxide, CuO. The numbers on the right-hand side in the figure show the quantification of the EDS spectrum from a large area of the inner tube surface. In addition, a cross-sectional sample was examined in STEM, Figure 8. The sample has been cut out through the tube wall starting from the inner tube surface. It was found that the grain boundaries between α -grains are attacked and the corrosion proceeds along grain boundaries without forming the amorphous, reddish corrosion product as it happens in the material prone to dezincification [3]. Results of the EDS mapping of the three areas marked in Figure 8 and given in Table 2 illustrate a complex chemistry that undergoes along the grain boundaries. Map 1 has confirmed the existence of upper and lower oxides observed with SEM. Map 2 revealed that the grain boundaries corrosion filaments are filled with Cu particles in a suspension of copper-chloride (CuCl_2) and organics. Map 3 shows that the lead particles encountered along the grain boundaries are completely oxidized and, as shown in Figure 8, broken up into smaller lumps. Additionally, a small amount of pure, dezincified copper was observed along the grain boundaries, but no copper-free (Zn, Al, Sn-rich) oxides. These were found only as the upper oxide on the inner tube surface but could also have been formed associated to grain boundaries but washed out during/after the corrosion process.

Conclusion

Corrosion sensitivity of the CW625 alloy in long-term exposure to sea water (forgings) and drinking water (tubes machined out of the extruded

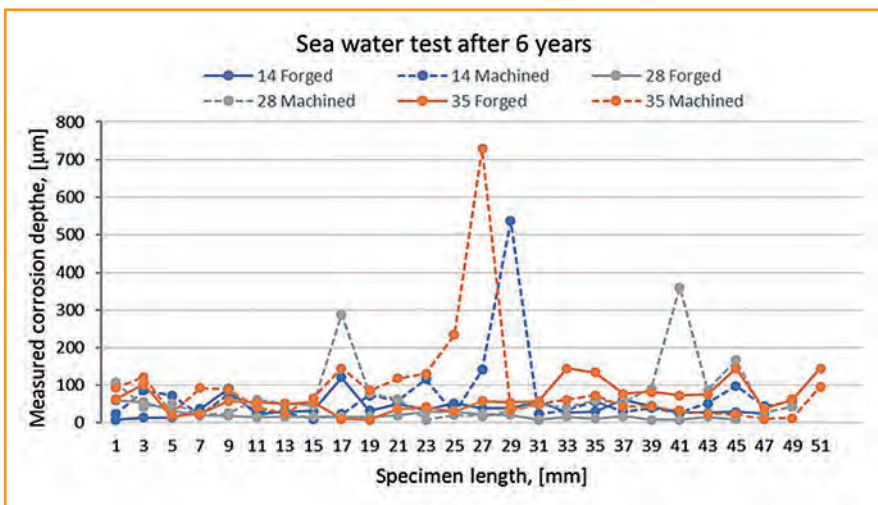


Fig. 5: Corrosion in the CW625 after exposition to the sea water for six years depending on the test article's geometry and surface quality (forged/ machined).

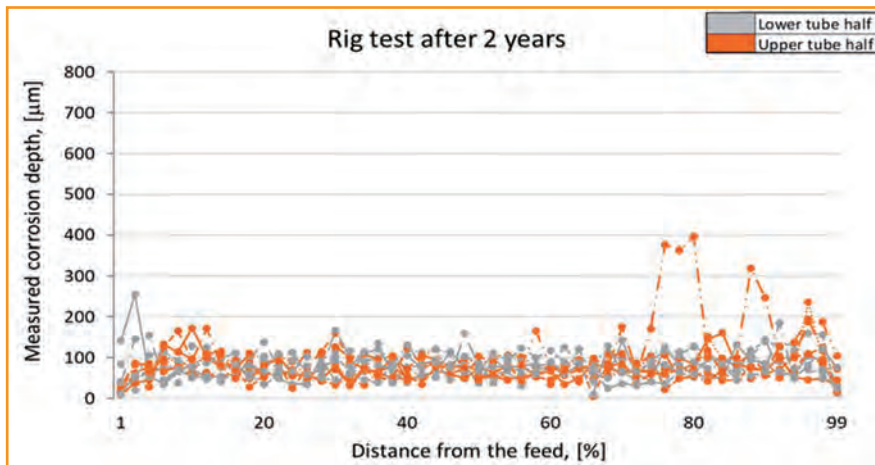


Fig. 6: Corrosion in the CW625 after exposition to the drinking water for 2 years

and DZR treated rod) has been evaluated. Further, corrosion products and chemistry that take place along the grain boundaries (IGC) in the tube material was investigated by use of STEM. The findings can be summarized as follows:

1. Dezinification is the dominating corrosion mechanism in the forgings containing more β -phase, while the intergranular corrosion is more pronounced in the tube material.
2. Based on average corrosion depth measured per year the DZR treated tube material is found more corrosion sensitive than the forgings, in the given circumstances.
3. Corrosion of the DZR treated CW625 starts with dezinification with small beta grains as initiations sites, resulting in amorphous corrosion products consisting of organic molecules and oxides of Zn, Al, Si, Ca built up over a pure copper oxide layer, at the surface in contact with corrosive medium. A complex chemistry proceeds further along the boundaries between α -grains, with chlorides as a main corrosive medium, resulting in the GB corrosion filaments filled

with Cu particles in a suspension of copper-chloride and organics. On the same way the lead particles along the grain boundaries are completely oxidized.

Acknowledgements

This work was carried out with financial support of the Research Council of Norway (NFR) in the framework of the project LOBUS (NFR grant 296054). Acknowledgement goes to NFR for the support to the Norwegian Micro- and Nano-Fabrication Facility, NorFab, project number 245963/F50. The TEM work was carried out on the NORTEM (NFR grant 197405) infrastructure at the TEM Gemini Centre, Trondheim, Norway.

References

- [1] Jacobsson, D., et al., Swerea KIMAB, Stockholm, Sweden, (2010).
- [2] Hutchinson, B., et al., Copper 06, France (2006). 13.
- [3] Tomovic-Petrovic, S., et al. World of Metallurgy - ERZMETALL 72, (2019)
- [4] Brandl, E. et al. Materials and Corrosion 60 (2009).
- [5] Choucri, J. et al. Metals 9 (2019).
- [6] Parthasarathi, A. et al. Metall Mater Trans A 13 (1982).
- [7] Guo, X., et al. Metall Mater Trans A 32 (2001).

- [8] Allam, N.K., et al. Ind. Eng. Chem. Res. 49 (2010).
- [9] Chen, Y. et al. Corrosion Science 47 (2005).
- [10] Allam, N. et al. J Solid State Electrochem 16 (2012).

- (1) Stanka Tomovic-Petrovic PhD, Sverre Gulbrandsen-Dahl, Sigurd Wenner, SINTEF Manufacturing AS, Department for Material technology
(2) Sigurd Wenner, Sintef Industry

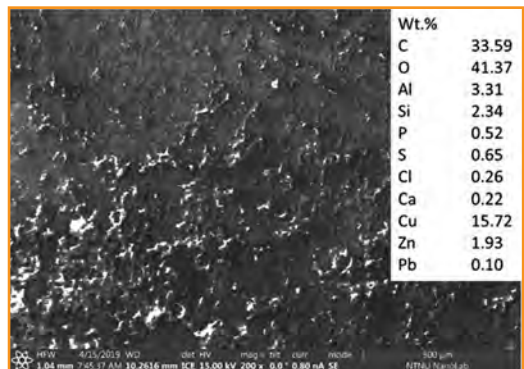


Fig. 7: SEM image of the inner surface of the 6 months corroded tube

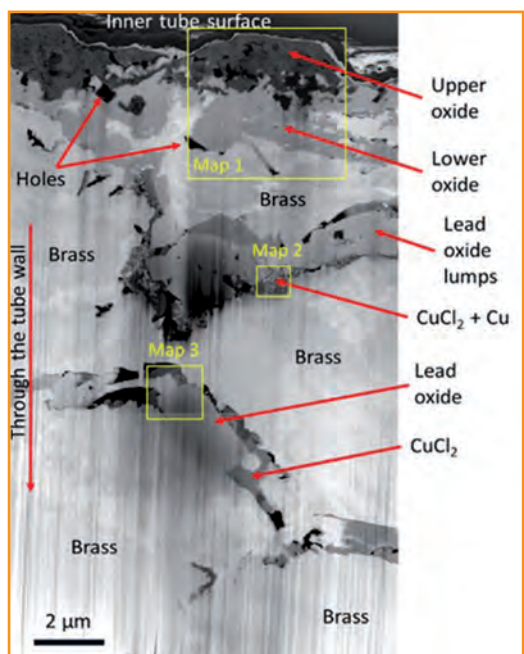


Fig. 8: STEM image of a cross-section through the 6 months corroded tube

at.%		C	O	Al	Si	Cl	Ca	Fe	Cu	Zn	As	Pb
Map 1	Upper oxide	31,79	47,96	5,41	5,37	0,16	0,23	0,08	7,5	1,2	0,01	0,14
	Lower oxide	0,62	41,68	0,30	0,14	0,70	0,00	0,07	55,21	0,89	0,02	0,14
Map 2	Copper	9,23	13,34	0,00	0,65	1,19	0,35	0,00	74,78	0,38	0,00	0,00
	Chloride	24,57	9,54	0,20	0,12	29,50	0,00	0,06	35,22	0,37	0,20	0,12
Map 3	Lead oxide	0,50	85,63	0,28	0,30	0,00	0,02	0,09	1,98	0,43	0,18	10,14

Table 2: Quantified composition of some of the phases marked in Figure 8

Assessment and Comparison of the Machinability of Innovative Copper Alloys

Zachert, C. (1); Brans, K. (1); Schraknepper, D. (1); Bergs, T. (1, 2)

Copper alloys are long-established technical materials that are used in various areas of industry. Examples of the wide range of applications are electrical connectors and components for the sanitary industry. Copper alloys are also used in friction wear application, such as plain bearings and rolling cages, to increase efficiency [GRUM15]. Lead as an alloying element not only has the task of acting as a chip breaker, but also has a technological influence on the entire production chain such as material processing and application properties. Due to the classification of the alloying element lead as toxic to reproduction in certain applications, copper alloys with alternative alloying elements are being developed as substitutes for the element lead. Focused on the machinability of the material, the technological advantages of lead, such as improved machinability and improved sliding and friction behavior, must be compensated by other alloying elements [REET19].

In the context of this work, innovative lead-free copper alloys were compared based on a defined assessment procedure using the four machinability criteria tool wear, surface quality, chip shape, and cutting force. The transparent and objective evaluation procedure allows the rating of the machinability of the investigated copper alloys. In the next step, further copper alloys will be ranked in relation to previous materials in terms of machinability.

to long chips, which have a negative impact on the machining process. The reason for this is the jamming of the chips between the tool and the workpiece, the influence on the quality of the generated workpiece surface and the poor chip removal. In addition to the microstructure, alloying elements also influence the machinability and thus the chip breakage. In the past, lead was often used as an alloying element. The lower shear strength significantly reduces the chip length. In addition, tool wear is drastically reduced by a lead lubricating film between tool and chip [GANE81, DKI10]. Legislation severely restricts the use of lead as an alloying element due to its harmful effects on health and the environment [ZOGH21, UHLM18, SCHU17, NOBE14].

This leads to the adjustment of the composition of copper alloys towards new alloying elements [PAN21]. For this reason, different copper alloys are currently being developed. In this paper, a selection of the alloys are presented and evaluated using a standardized evaluation method. Based on the results, materials for specific

These include bronzes (copper-tin alloy), brass (copper-zinc alloy) and beryllium copper (copper-beryllium alloy). Copper alloys are versatile used in the areas of installation technology, architecture and electrical engineering. Also with regard to renewable energies, copper alloys are increas-

gly required in electrical connectors or in electric motors [STEV22, HOFM18, NOBE14]. Due to this increasing demand, the amount of copper alloys to be machined is also increasing. Pure copper is malleable and tough, but as a ductile material it tends to stick and smear during machining process. The machining of the material leads

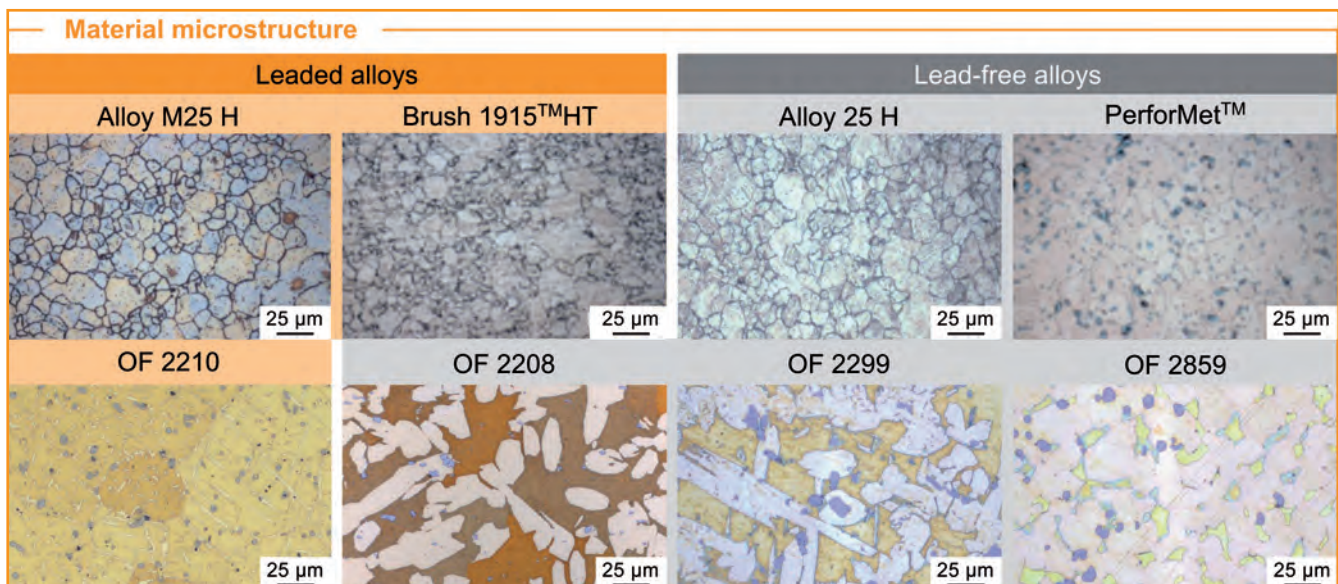


Fig. 1: Microstructure of the investigated copper alloys

Material	Alloy M25 H	Alloy 25 H	PerforMet™	Brush 1915™ HT	OF 2208	OF 2299	OF 2210	OF 2859
	CuBe2Pb	CuBe2	-	CuNiPb1P	CuZn37-Al1MnFe-NiCr	CuZn37-Mn3Al2-PbSi	CuZn30-Al2Mn2-Ni1FeSiSn	CuZn40-Fe2P
Chemical properties								
Be	1.8-2.0	1.8-2.0	-	-	-	-	-	-
Co+Ni	min. 0.2	min. 0.2	No data	No data	-	-	-	-
Co+Ni+Fe	max. 0.6	max. 0.6	No data	No data	-	-	-	-
Pb	0.2-0.6	max. 0.02	-	0.5-1.0	0-0.1	0-0.1	0.2-0.8	max. 0.1
Cu	Remnant	Remnant	Remnant	Remnant	59-61	63-65	57-59	57-59
Ni	No data	No data	6.5-7.5	0.8-1.2	0.3-0.8	0.5-1.2	0-1.0	-
P	-	-	-	0.15-0.35	-	-	-	0.1-0.5
Si	-	-	1.5-2.0	-	-	0.2-1.0	0.3-1.3	-
Cr	-	-	0.75-1.25	-	0.15-0.4	-	-	-
Fe	No data	No data	-	-	0.3-1.0	0.2-1.0	0-1.0	1-2
Mn	-	-	-	-	0.3-1.0	1.8-2.8	1.5-3.0	-
Al	-	-	-	-	0.7-1.2	1.5-2.5	1.3-2.3	-
Sn	-	-	-	-	-	0-0.5	0-0.4	-
Zn	-	-	-	-	Remnant	Remnant	Remnant	Remnant
Other	-	-	-	-	0-0.3	0-0.3	0-0.3	Impurities
Mechanical properties								
Yield strength R _{p0.2%}	678 MPa	691 MPa	827 MPa	567 MPa	171 MPa	230 MPa	320 MPa	128 MPa
Tensile strength R _m	700 MPa	711 MPa	896 MPa	604 MPa	482 MPa	591 MPa	630 MPa	364 MPa
Elongation A	18.7 %	21.1 %	10.5 %	12.0 %	41.6 %	27.2 %	22.0 %	48.3 %

Fig. 2: Chemical and physical copper alloy specification; Data in % by mass

components can be selected due to the determined cutting properties.

Experimental Setup

Copper alloys from Materion Brush GmbH and Otto Fuchs KG with different chemical compositions were the chosen test materials. The materials were used as cylindrical rods with a diameter of d = 40 mm and a length of l = 1,200 mm. Microstructure and compositions of the materials are shown in Figure 1. According to the composition, the alloys can be classified into leaded and lead-free alloys. The lead in Alloy M25 H, Brush 1915TMHT and OF 2210 distributes evenly and appears as fine particles within the matrix grains. In PerforMet™, the microstructure contains a large number of nickel silicide precipitations. In the microstructural sections of alloys OF 2208, OF 2299 and OF 2859, precipitations are visible as well. These are

silicides of manganese, iron or chromium. The type of particles in OF 2859 are iron phosphides.

In addition to the differences in the microstructure due to the chemistry, the copper alloys have different mechanical properties. These are summarized in Table 1. The first four alloys show high yield and tensile strength values in comparison to the other investigated alloys, which are achieved by means of precipitation strengthening.

An external cylindrical turning process was used to evaluate the machinability. The investigations were carried out on a NZX 1500 lathe from DMG MORI. An indexable insert of the type CNMG120408FP from Kennametal was used as cutting tool, which was held with the tool holder PCLNL 2525M-JHP from Iscar. The process was done under flood cooling with Blasomill GT22 cutting fluid from Blaser.

Four machinability criteria, cutting force, surface roughness, tool wear, and chip shape, were used as evaluation parameters. A 9119AA2 piezoelectric force-measuring platform from Kistler was used between the turret and the tool holder to measure the cutting force. The surface roughness was determined tactilely using a MarSurf LD 260 surface measuring device from Mahr in the axial direction along a sample. During the machining process, chips were collected and classified according to ISO 3685 [DIN93]. Tool wear, in particular flank wear, was determined at equidistant intervals and after a defined service life with a VHX 900F digital microscope from Keyence. The four machinability criteria are shown in Figure 2.

A cutting speed v_c = 200 m/min, a cutting depth a_p = 1 mm, and a feed f = 0.1 mm were selected as cutting parameters. For the investigation of tool wear, the feed rate was increased to f = 0.3 mm.

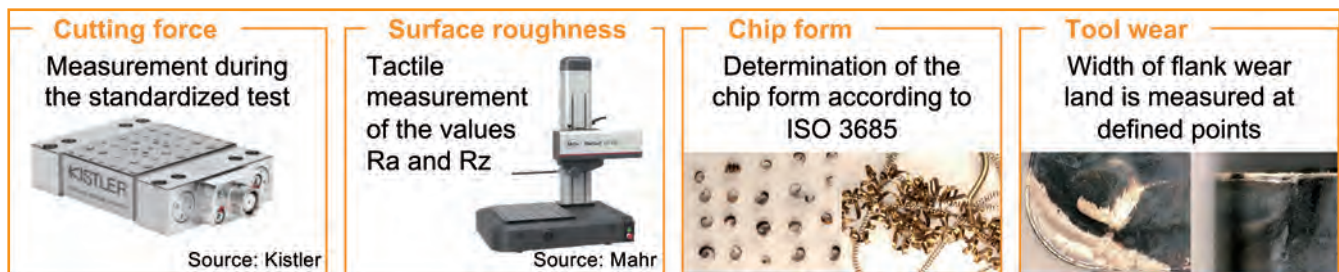


Fig. 2: Assessment criteria of machinability

Each of the four machinability criteria was rated with an index from 0 to 100 points being the better the higher values achieved in the investigation. A higher machinability index corresponds to a better machinability. As a reference, the index of 100 points was defined for the machinability of the leaded copper alloy CuZn39Pb3. The weighted average of the points from the four criteria results in the machinability index. Depending on the priority of individual criteria, different weighting factors can be used to simulate different machining conditions such as finishing or roughing. The calculation and weighting was done according to the methodology from [LUNG13] to ensure comparability.

Results of Investigation

The chip shape is presented in detail. All other results are summarized in an evaluation matrix. The chip shape gives direct conclusions about the machining process and the process stability. Long chips, on the one hand, provide the risk that they will damage the tool, the tool holder or the newly generated surface and thereby worsen the workpiece. Further on, long chips also lead to a poorer chip evacuation. On the other hand, too short chips in

the form of powder lead to pollution inside the machine tool chamber. For this reason, arc-shaped chips or short spiral-shaped chips are preferred. The formation of the chips depends, among other influencing factors, on the friction conditions between the tool and the workpiece and is influenced by the alloying elements. Other contributing factors come from the machining equipment and parameters, such as the tool normal rake angle and the cutting parameters, and were kept constant over the entire investigation.

Figure 3 shows characteristic chip shapes for the investigated materials at defined cutting parameters. It is clear that swirl chips occur with Alloy 25 H, which are to be evaluated as not optimal. Despite similar alloying elements to Alloy M25 H, machining leads to significantly altered chip breaking. Except for the additional alloying element lead, this is the same alloy. The influence of the alloying element lead becomes clear through the different machinability.

The same concerning the positive effect of lead on short chip breaking is observed for the leaded special brass alloy OF 2210. During the machining of the other investigated materials. These short chips can be removed

having no influence on the machining process. During the machining of OF 2210, discontinuous chips occurred. For all other materials in this investigation, flat spiral chips were formed during machining. Figure 4 summarizes the evaluations of all four machinability criteria. A Cu-ETP material and a CuCr1Zr were chosen as a reference for comparison. On the left side of Figure 4 the evaluation with equally weighted criteria for the general comparison of the materials is shown, on the right side the weighting is adapted for the evaluation of a roughing operation.

As shown in Figure 4, the best machinability index was achieved with OF 2210 for leaded materials and for lead-free materials with OF 2208. The alloys Alloy M25 H, Alloy 25 H, PerforMet™, Brush 1915 HTTM showed comparatively low machinability. However, the significantly higher strength level of these alloys must be taken into account here, which results from the different alloying concept combined with defined production parameters. Therefore, the areas of application of the investigated alloys are also different. In any case, the significantly better machinability compared to soft copper materials is clearly visible.

Chip form			Lead-free alloys				
Leaded alloys			Alloy 25 H	PerforMet™	OF 2208	OF 2299	OF 2859
Alloy M25 H	Brush 1915™HT	OF 2210					
Investigation parameter							
Process:	External cylindrical turning	Insert geometry:	CNMG 120408 FP	Cutting speed:	$v_c = 200 \text{ m/min}$		
Machine tool:	DMG MORI NZX 1500	Tool material:	KC5010	Depth of cut:	$a_p = 1 \text{ mm}$		
Cutting fluid:	Blasomill GT 22	Material:	varying	Feed:	$f = 0.1 \text{ mm}$		

Fig. 3: Chip form of the investigated materials

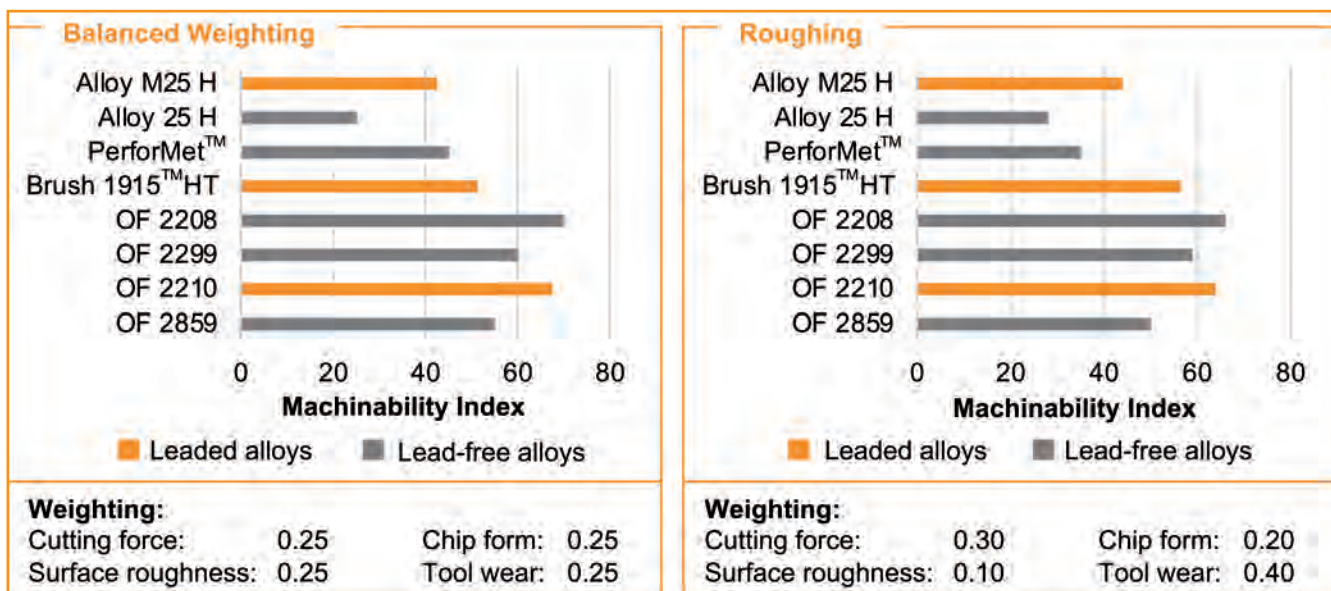


Fig. 4: Machinability of investigated copper alloys with different weightings

Clear relationships between microstructure and alloying elements as well as machinability could not be derived from the investigation results and require further research work. As already stated in other research work, the evaluation with a single index is only possible to a limited extent. For example, in previous investigations, a significantly different machinability index was determined for chemically similar materials such as CuZn38As and CuZn38. For this reason, the evaluation of machinability is currently still subject of research [SCHR21].

Conclusion and Outlook

Different copper alloys were investigated as examples for the assessment of the machinability. The aim was to evaluate different copper alloys that were developed due to substitution of lead as an alloying element. The investigation showed that the evaluation method using machinability indices based on the machinability criteria of cutting force, surface roughness, tool wear, and chip shape is suitable for making an objective statement about the machinability for different types of alloys.

The method can also be used in the future to evaluate newly developed alloys in terms of machinability. Depending on the application or manufacturing process, the machinability properties can be characterized and the material specifically selected.

For a more differentiated evaluation taking into account further material properties, the evaluation method must be extended.

Acknowledgement

The companies Materion Brush GmbH and Otto Fuchs KG supported the research work by providing material together with information about the chemical composition, microstructure and resulting mechanical properties.

References

- [DIN93] Tool-Life Testing with Single-Point Turning Tools, International Standard ISO 3685, 1993
- [DKI10] Richtwerte für die spanende Bearbeitung von Kupfer und Kupferlegierungen, Deutsches Kupferinstitut, Informationsdruck i.18, 2010
- [GANE81] The Effect of Lead on the Friction and Machining of Brass, N. Gane, Philosophical Magazine, Vol. 43, 1981
- [GRUM15] Anwendungsoptimierte Kupfer-Knetlegierungen für Gleit- und Wälzlager, H. Grummert, B. Reetz, Metall, Vol. 69, 2015
- [HOFM18] Über den Einfluss von Werkstoffkennwerten auf das Spanbruchverhalten von bleiarmem Messing, Materialwissenschaft und Werkstofftechnik, Vol. 49, 2018
- [LUNG13] Entwicklung einer Hochleistungszerspanung für schwerzerspanbare bleifreie Kupferknet- und -gusslegierungen, Schlussbericht IGF16867N, 2013
- [NOBE14] Machinability Enhancement of Lead-Free Brass Alloys, C. Nobel, F. Klocke, D. Lung, S. Wolf, Procedia CIRP, Vol. 14, 2014
- [PAN21] Accelerated Discovery of High-Performance Cu-Ni-Co-Si Alloys through Machine Learning, S. Pan, Y. Wang, J. Yu, M. Yang, Y. Zhang, H. Wei, Y. Chen, J. Wu, J. Han, C. Wang, Y. Liu, Materials & Design, Vol. 209, 2021

[REET19] Herausforderungen für die Bleifreiheit von Kupferlegierungen, B. Reetz, T. Münch, Metall, Vol. 73, 2019

[SCHR21] Entwicklung angepasster Werkzeuge und Prozesse zur Steigerung der Produktivität und Prozesssicherheit beim Fräsen innovativer bleifreier Kupferwerkstoffe, D. Schraknepper, Schlussbericht IGF20029N, 2021

[SCHU17] Comparative Study on the Machinability of Lead-Free Brass, F. Schultheiss, D. Johansson, V. Bushlya, J. Zhou, K. Nilsson, J.-E. Stahl, Journal of Cleaner Production, Vol. 149, 2017

[STEV22] A Coming Shortage Could Derail the Energy Transition, P. Stevens, CNBC, 2022

[UHLM18] Influence of Cutting Edge Micro-Geometry in Micro-Milling of Copper Alloys with Reduced Lead Content, E. Uhlmann, Y. Kuche, J. Polte, M. Polte, Procedia CIRP, Vol. 77, 2018

[ZOGH21] Modeling and Optimization of Drilling Operation of Lead-Free Brass Alloys Considering Various Cutting Tool Geometries and Copper Content, N. Zoghipour, G. Atay, Y. Kaynak, Procedia CIRP, Vol. 102, 2021

(1) Christoph Zachert, Kilian Brans, Daniel Schraknepper, Thomas Bergs, Laboratory for Machine Tools and Production Engineering (WZL) at RWTH Aachen University, Aachen, Germany

(2) Thomas Bergs, Fraunhofer Institute for Production Technology IPT, Aachen, Germany

Production of Polypropylene and Polyethylene Matrix Copper Reinforced Bio-composite and Investigation of Mechanical, Thermal and Morphologic Properties

Kaplan, Ü. (1); Birol, F. (1); Kaya, Ö. A. (2); Zığındere, O. (1); Taşdemir, M. (3)

Polymer materials are used in many sectors such as automotive, machinery, aviation and medical due to their easy forming, recycling, reuse and strong characteristic properties with their affordable cost. The properties of polymer materials such as thermal, mechanical and electrical conductivity can be improved by using these materials as polymer-metal, polymer-polymer, and polymer-fiber composites. This makes polymer composites the preferred material for many specific applications. Metals such as copper and silver are known as metals with antibacterial properties. Therefore, they are used in various antibacterial applications. However, the relatively high cost of these metals limits their use. In this study, the effect of the addition of some copper alloy powders in specific ratios to the antibacterial properties of Polyethylene (PE) and Polypropylene (PP) matrix, which are used extensively in the health sector, was investigated. Copper alloy powders in the range of 15-45 microns and polymer granules of 3-5 mm were used to prepare PE and PP composites. Components are processed by a twin screw extruder to obtain homogeneous mixtures. Test coupons for mechanical and thermal tests were produced metal powder-reinforced composite granules injection machine. Additions of copper powder to PE and PP materials were made at the rates of 0.5, 1, 3, and 5 wt%. The optimum ratio of copper alloy reinforcement for the mechanically and thermally stable composite was investigated.

Recently, polymer composites have become attractive materials for the medical, automotive and aerospace industries [1]. Composite materials are formed from two or more materials to achieve the desired properties.

Thermoset and thermoplastic materials are used as matrices in the most advanced composite materials. Studies are carried out to meet the needs of different sectors, such as metal and ceramic powders as an additive. [2,3,4]. Additional materials are used

to improve thermal, mechanical, electrical and physical properties [5-6]. These properties depend on the volume, forms and types, interface compatibility of the additive materials in the matrix and the production method composites [7]. In this study, the effect of the addition of some copper alloy powders in specific ratios to the mechanical and thermal properties of Polyethylene (PE) and Polypropylene (PP) matrix, which are used extensively in the health sector, was investigated.

Materials and Experimental

Copper alloy powders (CuCr1Zr) in the range of 15-45 microns and polymer granules of 3-5 mm were used to prepare PE and PP composites. The addition of CuCr1Zr powder to PE and PP materials was made at the rates of 0.5, 1, 3, and 5 wt % (Table 1). Components are processed by a twin screw extruder to obtain a homogeneous mixture of granules. The test coupons for mechanical and thermal tests were produced by using an injection machine.

The mechanical properties of the composites were examined. The average value of 5 samples was declared for each test. Tensile, Izod Impact, and hardness tests measurements were performed in accordance with the ASTM D638, ASTM D256, and ASTM D2240 respectively.

The thermal properties of the composite samples were investigated. The Heat Deflection Test (HDT) and Vicat softening temperature were carried out according to ISO 75 and ISO 307 standards with a Ceast brand tester. The Melt Flow Index (MFI) test was

Sample number	PE (%)	PP (%)	CuCr1Zr (%)
1	0	100	0
2	0	99,5	0,5
3	0	99	1
4	0	97	3
5	0	95	5
6	100	0	0
7	99,5	0	0,5
8	99	0	1
9	97	0	3
10	95	0	5

Table 1. CuCr1Zr alloy powder ratio (wt%) in PE and PP

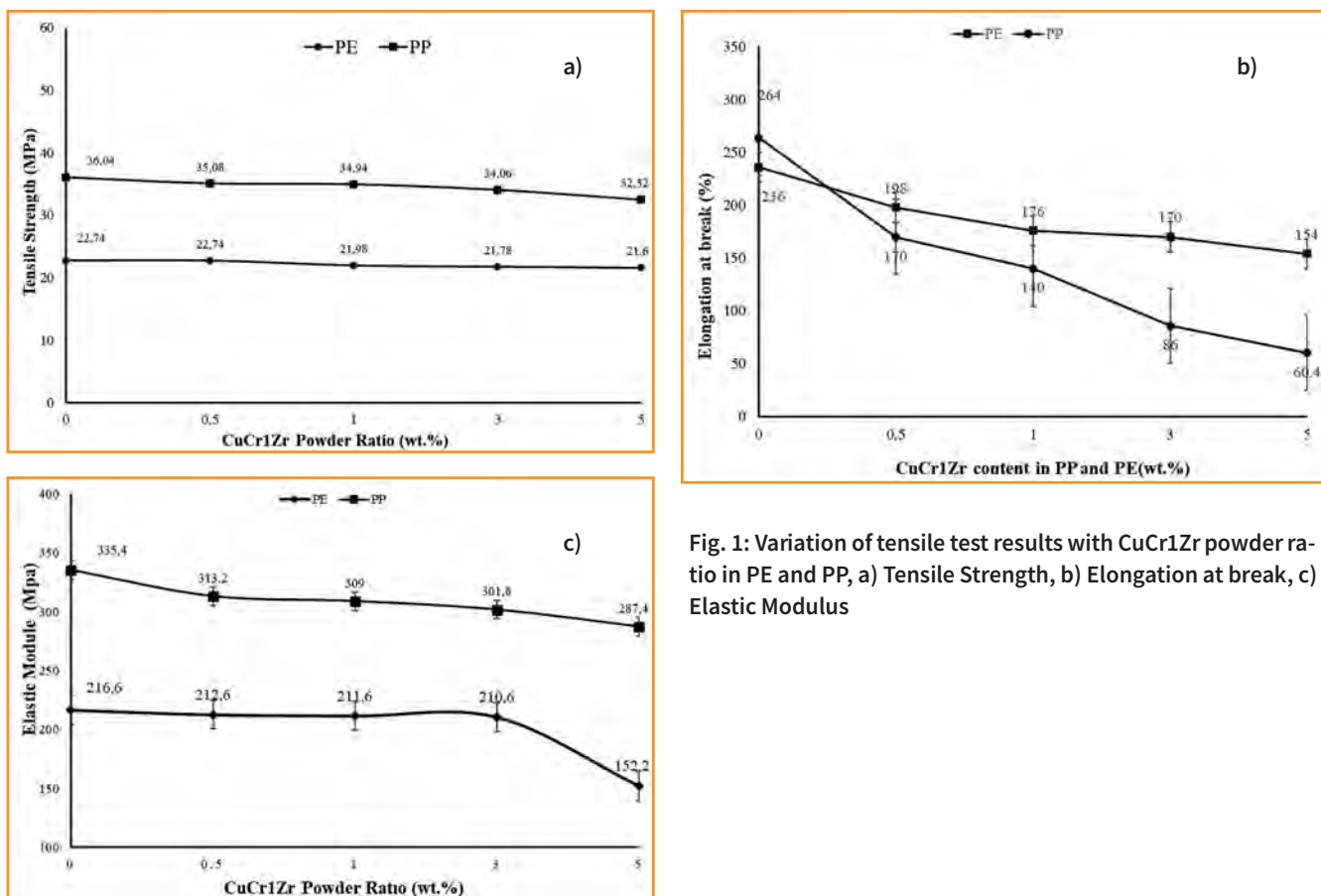


Fig. 1: Variation of tensile test results with CuCr1Zr powder ratio in PE and PP, a) Tensile Strength, b) Elongation at break, c) Elastic Modulus

performed according to ISO 1133 standard. The temperature applied to the sample was 230°C applied and forced to flow under a load of 2.16 kg.

Results and Discussion

The variation of the tensile test values with CuCr1Zr powder content in PE-PP/Cu polymer composite are given in Figure 1. The highest tensile strength values are obtained for the samples of pure PE (22,7 MPa) and PP (36 MPa) and decreased with the increase of

the CuCr1Zr powder ratio for both polymer types (Fig.1a). The tensile strength of pure PP was intrinsically higher than that of pure PE. The addition of 5 (wt.) % CuCr1Zr powder caused a higher decrease in the tensile strength of PP (9,7%) than that of PE (4,8%) while the lower CuCr1Zr addition (0,5 and 1 (wt.) %) was less effective on the tensile strength of both polymers. The elongation at break of both PE (236%) and PP (264%) was also severely affected by the addition of CuCr1Zr powder (Figure 1b).

Even a small amount of powder addition caused a significant reduction in elongation for both polymer composites. The PP with the higher beginning elongation revealed a higher decrease in elongation with increasing powder content, which was 77 % for the 5 (wt.) % CuCr1Zr while the decrease for the elongation of PE was 35% for the same CuCr1Zr content. The elastic modulus of the PE and PP composites changed with CuCr1Zr content as shown in Figure 1c. From the figure, the elastic modulus of the PE composites did not

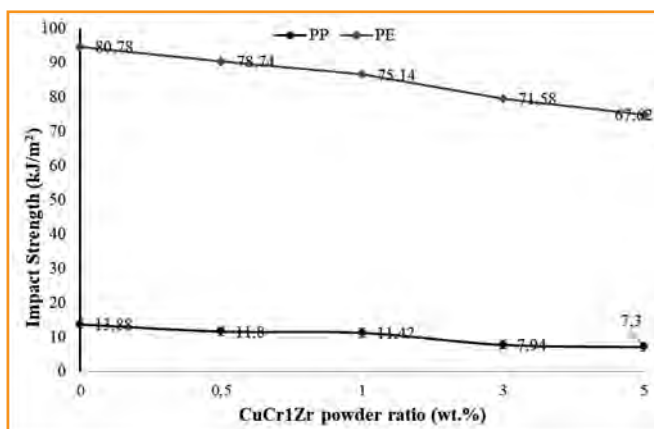


Fig. 2: Variation of Impacts Strength with CuCr1Zr powder ratio in PE and PP

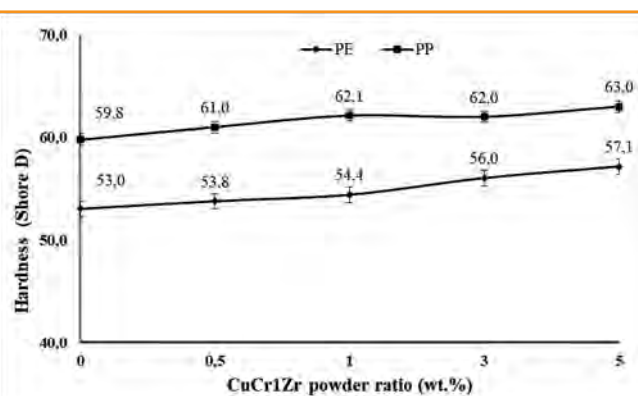


Fig. 3: Hardness values of the PP/PE composites as a function of CuCr1Zr powder concentration Hardness values of the PP/PE composites as a function of CuCr1Zr powder concentration

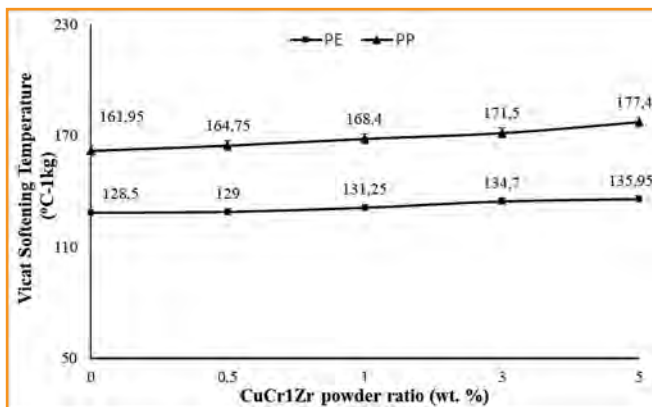


Fig. 4: Variation of VICAT softening temperatures of PP/PE composites with CuCr1Zr powder ratio

influence up to 3 (wt.) % CuCr1Zr content, then it dropped remarkably from 210 to 152,2 MPa (a 27,5 % drop) for the highest CuCr1Zr content (5 wt.%). However, the decrease of elastic modulus of the PP composites was stable and gradual with increasing powder concentration. The drop of the elastic modulus of PP for the highest powder addition (5 wt.%) was from 335,4 MPa to 287,4 MPa (approximately 14%). These mechanical properties findings are consistent with the work of Ying Tang et. al [8].

The impact strength of PP/PE composites was also influenced remarkably by the addition of CuCr1Zr powder and decreased with the rising powder content (Figure 2). Pure PE (80,78 kJ/m²) has a much higher impact strength than PP (13,88 kJ/m²). However, the impact strength of PP was affected by increasing CuCr1Zr powder content and determined a decrease of 47% for 5 % CuCr1Zr content while the decrease was 16% for the PE with the same content.

The hardness measurements of the PE/PP composites were given in Fig-

ure 3. The hardness of PP is slightly higher than that of PE. The addition of CuCr1Zr powders with an increasing ratio enhanced the hardness of both polymers to some extent. However, the effect was not as pronounced as the other features. Li-Xia Hu et al. showed that the addition of metal powder increased the hardness of the polymer composite [9]. Likewise, O.B. Zgalat-Lozynskyy determined that metal powders enhanced the hardness of PE [10].

Thermal properties of the PP/PE-CrCr1Zr composites were examined. Polymers soften at elevated temperatures, which limits their use. The Vicat softening temperature provides information about the elevated temperature behavior of polymers. The change in Vicat softening temperature of the PE and PP composites with the addition of CuCr1Zr powders is presented in Figure 4. It is clear that the addition of an increasing amount of copper alloy powder also affects the Vicat softening temperature of PP/PE in an increasing direction.

The MFI is a measure of the easy flow of the melt of a polymer, which is important data in the production of polymer-based products. The addition of CuCr1Zr powder influenced dramatically the MFI values of both PE and PP samples (Figure 5). However, the increase

in the MFI with increasing CuCr1Zr was remarkably high for the PP samples. Even a small amount addition of CuCr1Zr (0,5 (wt.)) caused the MFI of PP to rise from 0,243 (g/10 min.) to 0,523 (g/10 min.) while the MFI of PE to increase from 0,843 (g/10 min.) to 1,031 (g/10 min.). The MFI of PP composites increased more gradually with increasing CuCr1Zr content compared with the PE composites.

The HDT of PE and PP as a function of CuCr1Zr content was tested (Figure 6). From the diagram, it may be noted that there is a small effect of increasing the addition of CuCr1Zr powder content range used in this study on the heat deflection temperature of the PP and PE composites.

Conclusions

Homogenous PE and PP composites are produced by using a two-step method. The first step was granule preparation by using a twin-screw extruder and then an injection molding machine was used for desired parts.

The addition of various concentrations of CuCr1Zr powder affected the mechanical and thermal properties of PE and PP composites:

- The addition of 5 (wt.) % CuCr1Zr powder caused a higher decrease in the tensile strength of PP (9,7%) than that of PE (4,8%) while the lower CuCr1Zr addition (0,5 and 1 (wt. %)) was less effective on the tensile strength of both polymers.
- The elongation at break of both PE and PP was severely affected by the addition of CuCr1Zr powder and decreased with increasing CuCr1Zr

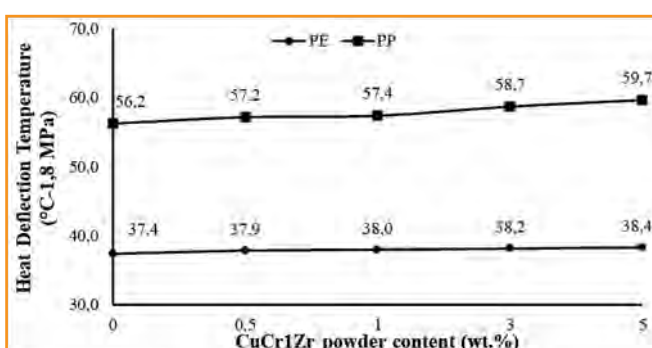


Fig. 5: Graph of the Heat Deflection Temperature-CuCr1Zr powder content

concentration. A decrease in elongation at break of 77% in PP material and 35% in PE material was detected with 5% CuCr1Zr powder added. The elastic modulus of both PE and PP composites was influenced by the addition of CuCr1Zr powder. However, the effect was more pronounced for the PE composite with 5 wt.% powder content.

- The impact strength of PP/PE composites decreased with the rising powder content.
- The addition of CuCr1Zr powders with an increasing ratio enhanced the hardness of both polymers to some extent. However, the effect was not as pronounced as the other features.
- The increasing amount of copper alloy powder addition affected the Vicat softening temperature of PP/PE in an increasing direction.
- The increase in the MFI with increasing CuCr1Zr content was

remarkably high for the PP samples.

- There was a small effect of increasing the addition of CuCr1Zr powder content range used (0,5-5 wt. %) on the HDT of the PP and PP composites.

References

- [1] Brostow, Witold, et al. "Microhybrids of metal powder incorporated in polymeric matrices: Friction, mechanical behavior, and microstructure." Polymer Engineering & Science 48.10 (2008): 1977-1981.
- [2] Zhu, K.; Schmauder, S. Prediction of the failure properties of short fiber reinforced composites with metal and polymer matrix. Computational Materials Sci. 2003, 28, 743.
- [3] Rusu, M., Sofian, N., & Rusu, D. (2001). Mechanical and thermal properties of zinc powder filled high density polyethylene composites. Polymer testing, 20(4), 409-417.
- [4] Cheang, P.; Khor, K.A. Effect of particulate morphology on the tensile behaviour of polymer-hydroxyapatite composites. Mater. Sci. and Eng. A. 2003, 345, 47.
- [5] A.A. Berlin, S.A. Volfson, S.S. Enikolopian, S.S. Negmatov, Principles of Polymer Composites, Akademie Verlag, Berlin, 1986.
- [6] V.A. Paharenko, V.G. Zverlin, E.M. Kirienko, Filled Thermoplastics, Tehnika, Kiev, 1986.
- [7] R. Kilik, R. Davies, Mechanical properties of adhesive filled with metal powders, International Journal of Adhesion and Adhesives 9 (4) (1989) 224.
- [8] Schmidt, M. G., Tuuri, R. E., Dharsee, A., Attaway, H. H., Fairey, S. E., Borg, K. T., & Hirsch, B. E. (2017). Antimicrobial copper alloys decreased bacteria on stethoscope surfaces. American journal of infection control, 45(6), 642-647.
- [9] Różańska, A., Chmielarczyk, A., Romaniszyn, D., Bulanda, M., Wałkowicz, M., Osuch, P., & Knych, T. (2017). Antibiotic resistance, ability to form biofilm and susceptibility to copper alloys of selected staphylococcal strains isolated from touch surfaces in Polish hospital wards. Antimicrobial Resistance & Infection Control, 6(1), 1-12.
- [10] Hollaway, L. C. (2004). Advanced Polymer Composites for Structural Applications in Construction: ACIC, (The University of Surrey, UK).

(1) Ümit Kaplan, Feriha Birol, Orçun Zığındere, Sağlam Metal, TURKEY

(2) Ömer Alparslan Kaya, Sağlam Metal - Marmara University, TURKEY

(3) Münir Taşdemir, Marmara University, TURKEY

Analysis of CuSn8 components manufactured using the material jetting process

Plötz, M.; Kirchebner, B.; Volk, W.; Lechner, P. (1)

The processing of metals in the material jetting process has recently become an increasing focus of science and industry. The present work investigates the processing of copper-tin-bronze in the material jetting process. A print head and a heated platform were developed for the investigations. Subsequently, two test piece geometries are fabricated at different substrate and melt temperatures. The surface of the components is examined using optical microscopy and 3D laser scanning microscopy. In addition, a comparison of the material microstructure is performed. Uniaxial tensile tests are performed to evaluate the mechanical properties. First results show that with increasing temperature there is an improvement of the droplet bonding. In addition, the pores present in the component are reduced and the determined values for tensile strength and uniform elongation increase.

The material jetting process (MJT) is an established process for the production of polymer components (Gülcanc et al., 2021). For some years now, the processing of metallic materials has also been investigated, which have a significantly higher melting temperature compared to the polymers used. In the MJT process, the build material is melted in a print head and deposited via a nozzle, droplet by droplet onto a platform (Gibson, 2021). A wire-shaped semi-finished product can be used as the feedstock for MJT with metals. A three-dimensional component can be built up layer by layer by the solidification of the droplets deposited on the moving platform or on the already partially printed component. The generation of droplets can be, among others, piezoelectric (Lee et al., 2008), magnetohydrodynamic

(Vader et al., 2015) or pneumatic (Lass et al., 2013). For MJT with aluminium materials, several articles already exist, which deal with the influence of different process parameters on droplet bonding. The first aluminium components were produced by Orme and Smith (1999) using a continuous droplet generator. The fabricated components exhibited higher yield strength and tensile strength with similar elongation values compared to cast specimens. Zuo et al. (2016) was able to fabricate Al 7075 test specimens using the MJT process by selecting an appropriate parameter configuration of substrate and droplet temperature. Droplet adhesion was sufficient in this process to produce parts with comparable mechanical properties to extruded parts. The authors explain the reason for the good droplet bonding with the re-melting of the already

deposited droplet. Himmel et al. (2018) investigated the MJT process with Al 4047A. It was shown that good bonding is possible without re-melting of the already deposited substrate and, in particular, that the wetting properties during droplet deposition influence the component properties.

The generation of liquid copper droplets was studied by Zhong et al. (2012). The authors investigated the influence of the pressure level and the valve opening time on the droplet generation and were able to show that an increase in the droplet size is accompanied by an increase in the pressure level. In addition, columnar components could be printed from copper materials. However, the components were not characterized further.

In the present work, components were produced from CuSn8 using the MJT process and the influence of different process temperatures on component quality was investigated.

Methods

For processing copper materials in the MJT process, a drop-on-demand printhead with a pneumatic actuator and a heated build platform were developed. The setup used to perform the experiment is shown in Figure 1. The cylindrical graphite crucible located in the print head can be heated up to a maximum temperature of 1200 °C by means of resistance heating elements. A nozzle plate closes the bottom of the crucible. The wire-shaped semi-finished product can be fed into the crucible at the top. This is melted and stored in the crucible. A pneumatic pressure impulse can be applied to the melt via a solenoid valve. This allows the melt droplets to be ejected through the 500 µm diameter orifice in the nozzle plate. Nitrogen is used as the process gas. The print head is mounted on a process chamber that is also flooded with nitrogen. The build

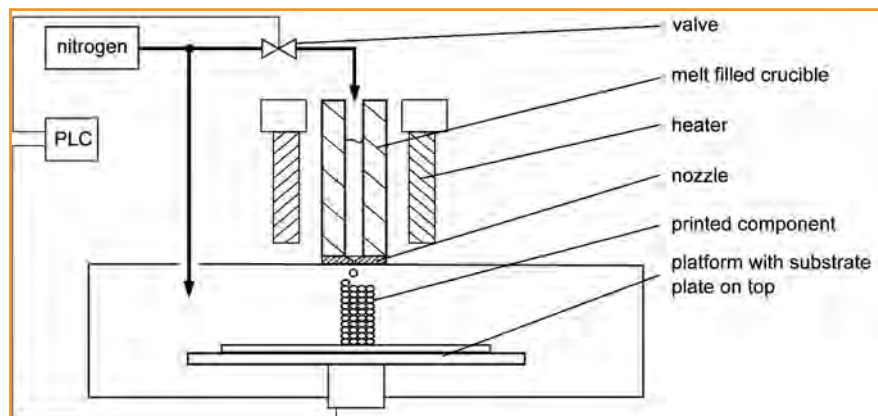


Fig. 1: Schematic illustration of the test stand

platform, which can be moved in all three directions in space, is located in the process chamber. The platform can be heated up to 900 °C using a resistance heating element. The droplets produced by the print head are deposited on a stainless steel substrate plate located on the heating element of the build platform. The parameters of the pressure impulse generation, the temperatures of the crucible and build platform, and the movements of the build platform are controlled by a programmable logic controller (PLC). In order to identify the influence of different process parameters, two parameter configurations are investigated. For the first parameter configuration, a substrate temperature $T_{\text{sub}} = 580 \text{ }^{\circ}\text{C}$ and a melt temperature $T_{\text{melt}} = 1090 \text{ }^{\circ}\text{C}$ are used. For the second parameter configuration, the substrate temperature is $T_{\text{sub}} = 780 \text{ }^{\circ}\text{C}$ and the melt temperature is $T_{\text{melt}} = 1190 \text{ }^{\circ}\text{C}$.

A wire made of CuSn8 is used for all manufactured components. Ten droplets with a diameter of approximately 1 mm are ejected per second from the print head. Two different component geometries are examined in the course of the investigations.

In a first step, a component with a square base area is produced for each of the two parameter configurations. A component layer consists of four parallel rows of four droplets each. To produce a component, 15 layers are placed on top of each other. After fabrication, optical examination of the component surface is performed using a VHX-2000 digital microscope (Keyence Deutschland GmbH, Neu-Isenburg, Germany). The images are taken using the VH-Z20R objective lens with a magnification of 30:1. In addition, further examination of the component surface is performed using a VK-X100 series 3D laser scanning microscope (KEYENCE DEUTSCHLAND GmbH, Neu-Isenburg, Germany) to identify possible defects on the component surface. To investigate the material microstructure, the components are embedded in resin (Kulzer GmbH, Hanau, Germany), ground and polished. The microstructure is examined about 1.5 mm below the component surface, which is used for the optical examination. To make the microstructure visible, the ground

component surface is etched. The AxioCam MRc5 camera system, which is part of the Axioplan 2 reflected-light microscope (Carl Zeiss MicroImaging GbmH, Göttingen, Germany), is used for the examination. The images are taken using polarized light.

The optical examination of the component surface and the material structure is followed by the mechanical characterization of the components. For this purpose, a component with the second component geometry is produced for each of the two parameter configurations. The components consist of seven layers, with one layer consisting of five parallel rows of 30 drops each. The cuboids produced have dimensions of 31 x 6 x 6 mm. A round tensile specimen with a diameter of 3 mm and a parallel length of 18 mm is manufactured from each cuboid. Mechanical properties are determined using a quasi-static tensile test on a 1484/DUPS-M universal testing machine (Zwick GmbH & Co. KG, Ulm, Germany). The strain rate used is $2.5 \times 10^{-4} \text{ s}^{-1}$. A Makro extensometer (Zwick GmbH & Co. KG, Ulm, Germany) is used to determine the change in length.

Results and Discussion

The influence of different process parameters on the external appearance of the components and the material structure are shown in Figure 2. The component shown on the left side of the figure is manufactured at a substrate temperature of $T_{\text{sub}} = 580 \text{ }^{\circ}\text{C}$ and a melt temperature of $T_{\text{melt}} = 1090 \text{ }^{\circ}\text{C}$. The right-hand side shows the component produced at a substrate temperature of $T_{\text{sub}} = 780 \text{ }^{\circ}\text{C}$ and a melt temperature of $T_{\text{melt}} = 1190 \text{ }^{\circ}\text{C}$. For each component, the component surface and the material microstructure are examined. On the left-hand side of the figure, an image of the component surface is shown in each case. In the centre, a scan of the component surface taken with the 3D laser scanning microscope is shown. To compare the surface scans, a reference plane was defined for each component, which intersects the top row of drops in the middle. Next to the surface scan, the micrograph of the component is etched and shown under polarized light.

Comparing the two components produced at different temperatures, a decrease in component height with increasing temperature can be observed. In addition, the component on the right side has a more homogeneous and smoother surface. This can also be seen, when comparing the surface scans. The reason for this is the better fusion of the newly deposited droplets with the already deposited substrate, resulting in a decrease in the size and frequency of the pores between the droplets. The decrease in pores can also be seen from the etched micrographs. The component on the left has several areas across the cross-section where pores are visible between the individual droplets. In addition, there are droplets between which no fusion has taken place. The micrograph of the component on the right side shows significantly fewer pores and unconnected droplets. In addition, this component tends to have a recrystallized microstructure due to the higher temperatures used

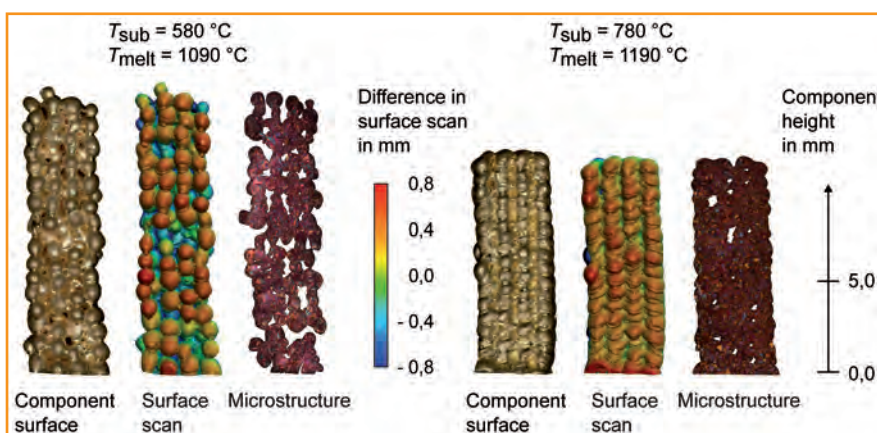


Fig. 2: Comparison of component surface and material structure

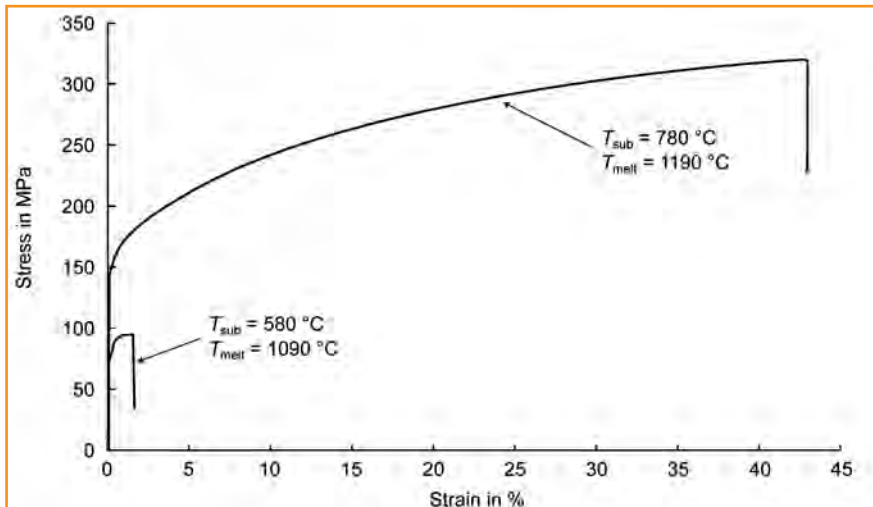


Fig. 3: Stress-strain curves determined in the tensile test

to manufacture the component, while the component on the left has largely a cast microstructure.

Figure 3 shows the stress-strain curves obtained from the second component geometry in the tensile test. The part produced at the low temperatures shows significantly lower values for tensile strength and uniform elongation. This is due to the high amount of pores and unconnected droplets. For the part produced at the higher temperatures, a tensile strength of 321 MPa with a uniform elongation of 43% is achieved.

Conclusion

Based on the investigations in the present work, it could be shown that the substrate and melt temperatures have a significant influence on the properties of bronze components produced

in the MJT process. Higher temperatures lead to a more homogeneous component surface and a reduction in component porosity. In addition, an increase in tensile strength and uniform elongation can be observed due to better fusion of the droplets at higher temperatures. Further extensive investigations are necessary to quantify the influence of the thermal process variables in the processing of copper materials.

Acknowledgements

This research was supported by the AiF (IGF project no. 21553 N).

References

- Gibson, Ian (2021): Additive Manufacturing Technologies. Unter Mitarbeit von David Rosen, Brent Stucker und Mahyar Khorasani. 3rd ed. Cham: Springer International Publishing AG.
- Gülcen, Orhan; Günaydin, Kadir; Tamer, Aykut (2021): The State of the Art of Material Jetting—A Critical Review. In: Polymers 13 (16), S. 2829.
- Himmel, Benjamin; Rumschoettel, Dominik; Volk, Wolfram (2018): Tensile properties of aluminium 4047A built in droplet-based metal printing. In: RPJ 25 (2), S. 427–432.
- Lass, Nils; Rieger, Lutz; Zengerle, Roland; Koltay, Peter (2013): Enhanced Liquid Metal Micro Droplet Generation by Pneumatic Actuation Based on the Star-Jet Method. In: Micromachines 4 (1), S. 49–66.
- Lee, Taik-Min; Kang, Tae Goo; Yang, Jeong Soon; Jo, Jeongdai; Kim, Kwang-Young; Choi, Byung-Oh; Kim, Dong-Soo (2008): Gap Adjustable Molten Metal DoD Inkjet System With Cone-Shaped Piston Head. In: Journal of Manufacturing Science and Engineering 130 (3), Artikel 031113, S. 3.
- Orme, Melissa.; Smith, R. F. (1999): Enhanced aluminum properties by means of precise droplet deposition. In: Journal of Manufacturing Science and Engineering 122 (3), S. 484–493.
- Vader, Scott; Vader, Zachary; Karampelas, Ioannis; Furlani, Edward (2015): Magnetohydrodynamic liquid metal jet printing. In: TechConnect Conference (716), S. 2–4.
- Zhong, Song Yi; Le Qi, Hua; Luo, Jun; Xiao, Yuan (2012): Parameters Study on Generation of Uniform Copper Droplet by Pneumatic Drop-on-Demand Technology. In: AMR 430-432, S. 781–784.
- Zuo, Hansong; Li, Hejun; Qi, Lehua; Zhong, Songyi (2016): Influence of Interfacial Bonding between Metal Droplets on Tensile Properties of 7075 Aluminum Billets by Additive Manufacturing Technique. In: Journal of Materials Science & Technology 32 (5), S. 485–488.
- (1) Maximilian Plötz , Benedikt Kirchbener, Wolfram Volk, Philipp Lechner, Technische Universität München

Overview of non-metallic inclusions in Copper and Copper Alloys

Voigt, C.; Gumban, G. C.; Hubálková, J.; Aneziris, C. G. (1)

The content of non-metallic inclusions, gases and metallic impurities is an important factor influencing the performance and efficiency of copper processing. For this reason, the requirements for purity are constantly increasing. With refining electrolysis, a high purity copper is reachable, but during melting and casting in foundries non-metallic inclusions are introduced and formed. The BMBF-Junior Research Group "PurCo - Purification of copper" at TU Bergakademie Freiberg aims to increase the purity of the copper in foundries by newly developed filter materials. Determination of copper melt purity in terms of non-metallic inclusion content is a prerequisite to the evaluation of the suitability of the newly developed filter materials. Currently, there is a lack of detailed information on the expected non-metallic inclusions with physical, chemical and morphological data. Within the scope of this study, scrap material and used filters will be investigated in order to compile a list of non-metallic inclusions to be expected in copper melts. Emphasis will be placed on characterizing the inclusions using scanning electron microscopy (SEM), energy dispersive X-ray spectroscopy (EDX), and electron backscatter diffraction (EBSD), but also providing light microscopy (LM) images to ensure easy recognition of the non-metallic inclusions by foundries.

Copper is one of the indispensable materials due to its properties. The content of non-metallic inclusions (SiO_2 , Al_2O_3 , SiC , Cu_2O), gases (hydrogen and oxygen) and metallic impurities is an important factor influencing the performance and productivity of copper processing [1]. For this reason, the requirements for purity increase. With refining electrolysis, high purity copper is reachable, but during melting and casting in foundries non-metallic inclusions are introduced and formed. Foundries have started to use foam ceramic filters due to the cleaning effect and a calming of the melt. According to Apsley et al [2], the use of foam ceramic filters in a copper processing company resulted in a reduction of scrap and rejection rates from 12% to 4%. Liu et al [3] used cordierite foam ceramic filters and achieved a reduction in scrap from 30-40% to 3-4%. A reproducible description of the former experiments and a result presentation were not provided in either case.

In order to be able to qualify the newly developed filters, it should first be possible to evaluate the purity of the copper melt in terms of inclusion con-

tent. Experiments towards this direction are described in the final report of the AiF project 16254 N [4], where attempts were made to quantify the concentration of inclusions using a PoDFA device without success due to filter blockages. Another approach was to directly quantify inclusions in molten copper using Coulter counters [5], which was supposed to be successful according to the author but has not yet been used in industry.

In addition to non-metallic impurities, hydrogen dissolved in copper also adversely affects the cast quality. It is important to note that it is not the hydrogen itself that forms gas bubbles, but the hydrogen that molecularly precipitates during solidification [6]. Another theory is that the bubbles are formed by the formation of water vapor during solidification [7]. A reaction of molecular hydrogen (from the atmosphere) with Cu_2O can lead to embrittlement [8]. Therefore, foundries try to achieve the lowest possible hydrogen content when melting cathodes and secondary raw materials by using a slightly reducing atmosphere. This leads to oxygen enrichment in the melt, which is subsequently reduced by means of reducing agents (carbon

monoxide or phosphorus). Purge gas treatments or the application of a vacuum have also been used to degas the melt [9]. Covering the melt with carbonaceous materials (e.g., coke) minimizes new reactions with hydrogen [10]. Despite these measures, the problem of removing hydrogen from the melt to reduce hydrogen porosity and removing oxygen (to avoid Cu_2O formation) has not been solved yet. In addition, due to the energy transition, companies in the copper processing industry have an increasing interest to replace the energy carrier natural gas by hydrogen. The related challenges regarding the hydrogen content in the copper melt will increase further. The BMBF-Junior Research Group "PurCo - Purification of copper" at TU Bergakademie Freiberg aims to increase the purity of the copper in foundries with regard to non-metallic inclusions and hydrogen among others by newly developed filter materials.

Introduction of the junior research group PurCo

The junior research group PurCo - Purification of copper is a BMBF junior research group funded by BMBF (Bundesministerium für Bildung und Forschung - Federal Ministry of Education and Research) has the objective to investigate the possibilities of metal melt filtration in the area of copper foundries. According to the scientific literature, copper melt filtration is a neglected topic in the international research. This is an astonishing fact due to the excellent results in the field of aluminum and iron filtration which is a state-of-the-art procedure since decades.

The junior research group PurCo is scheduled for a funding period of 4,5 years and is a cooperation of the Institute of Ceramics, Refractories and Composite Materials and the Institute of Nonferrous Metallurgy and

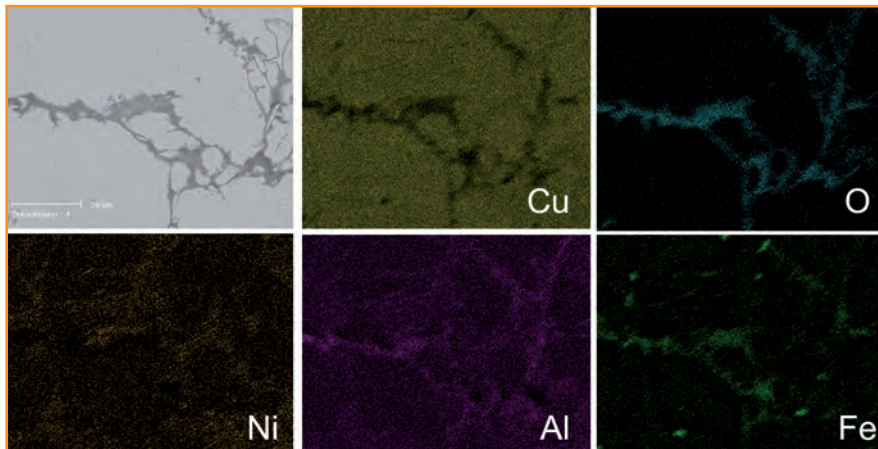


Fig. 1: SEM image (BSE mode) with oxide film in a copper sample (CuAl10Fe5Ni5) and corresponding EDX mapping

Purest Materials at the TU Bergakademie Freiberg. The research focuses on the establishment of an inclusion catalog and a quantification of inclusions to evaluate the copper purity. Furthermore, innovative filter materials should be developed and tested with regard to filtration behavior and interactions between copper and the filter material. For the evaluation of the copper purity after using different filter materials, a pilot filtration apparatus will be designed, constructed and tested. A further research topic is the measurement of filter roughness and the determination of the influence of filter roughness on the filtration behavior. The development of a measurement method for the determination of the hydrogen content in copper and a reduction of the hydrogen content by the application of ceramic foam filters are further objectives of the junior research group PurCo.

Materials and methods

Copper samples provided by different copper foundries were photographed by a digital microscope VHX-2000 (Keyence, Japan). In the next step, the

samples were cut out and embedded in an epoxy resin, ground, polished and analyzed with the SEM XL 30 (Philips, Germany) equipped with an energy-dispersive X-ray spectroscopy device (Phoenix, USA). Furthermore, images of the samples with a digital microscope VHX-2000 (Keyence, Japan) were taken.

Results

Non-metallic inclusions in copper or copper alloys can be divided into different groups based on their origin:

- Endogenous inclusions which are formed by chemical reactions in the copper melt, i.e. copper oxide films
- Endogenous inclusions introduced by
 - Auxiliary materials, i.e. refractory particles or graphite particles from the melt cover
 - Metallurgical processes, i.e. slag components, scrap impurities and scale particles

According to Friedrich et al. [1], non-metallic inclusions in copper are easier to remove compared to other metal melts because the large density difference between melt and inclusions

allows larger inclusions float to the melt surface. For smaller inclusions the buoyancy is too low to reach the melt surface in an appropriate time. Inclusions remaining in the copper melt led to problems in the production processes of wire drawing and sheets rolling [1].

Only a part of the inclusions detected in the copper samples will be presented. Oxide films can be found often especially in copper alloys containing aluminum. They are characterized by net-like narrow areas looking like veins. The EDX mapping of the oxide film presented in Figure 1, show the oxygen in the film but also show increased amounts of aluminum, iron and nickel.

A known quality issue is the appearance of black scale particles (copper oxide CuO) which are formed during melt processes, heat treatment or hot forming of copper. Due to large dimensions of the scale particles (see Figure 2), they are a critical quality issue i.e., for the surface quality.

There is a large variety of inclusions consisting of a multiple of elements i.e., the inclusion in Figure 3. The core of the structure is a silicon carbide particle which was served as a docking point for structures consisting of oxygen, aluminum, and phosphorus.

Conclusion

There is a large variety of non-metallic inclusions detectable in copper and copper alloys. A systematic investigation will help to improve the copper quality.

Acknowledgement

The authors would like to thank the Federal Ministry of Education and Research (BMBF) for supporting these

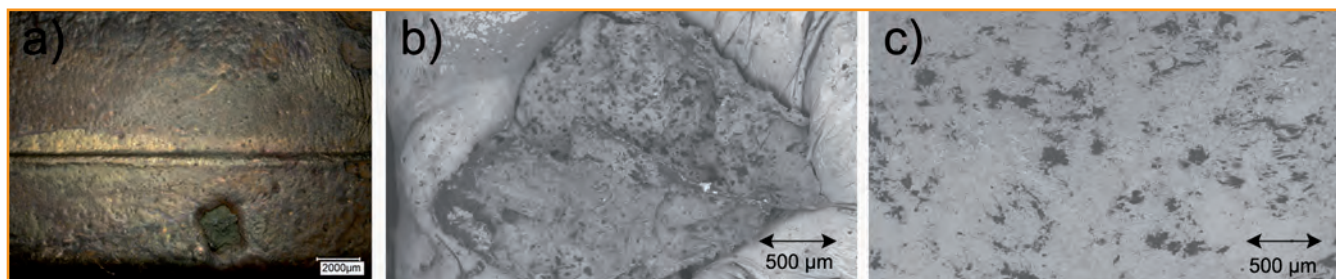


Fig. 2: Scale particle at the surface of a copper casting (CuCr1) a) image of scale particle taken with digital microscope, b) image of scale particle taken with SEM (BSE mode), c) image of area near to scale particle taken with SEM (BSE mode)

investigations as part of the BMBF Junior Research Group PurCo – Purification of Copper (Project-ID 03XP0420).

References

- [1] B. Friedrich, C. Kräutlein: Melt Treatment of copper and aluminium – The complex step before casting (2006) DOI: 10.1002/9783527607969.ch1.
- [2] S.D. Apsley: Energiesparen mit SIVEX FC Filtern, Foundry Practice 228 (1996) S. 13-17.
- [3] P. Liu, G.F. Chen: Porous materials processing and applications (2014) ISBN: 978-0124077881, Butterworth-Heinemann, S. 307.
- [4] Schlussbericht des AiF-Projekts 16254N: Verbesserung der gießtechnischen Eigenschaften neuer bleiarmer Kupfergusslegierungen zur Herstellung druckdichter Armaturen und Rohrverbinder, Bewilligungszeitraum: 01.11.2009-bis 30.04.2012.
- [5] S. Kuyucak & R. I. L. Guthrie: On the Measurement of Inclusions in Copper-Based Melts, Canadian Metallurgical Quarterly 28 (1989) 41-48.
- [6] G. R. Caskey: Hydrogen Transport in Copper Chemistry (2001) Corpus ID: 91319263.
- [7] R. Sandström: The role of hydrogen in copper, Materials Science (2014) Corpus ID: 55758916.

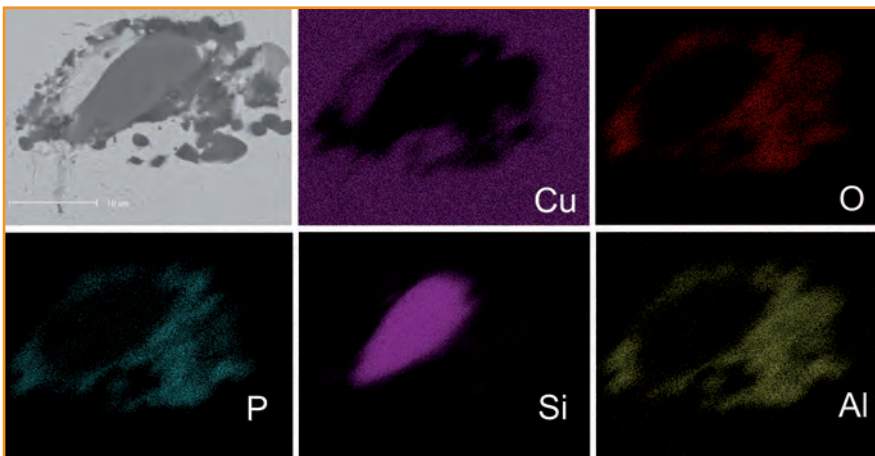


Fig. 3: SEM image (BSE mode) and corresponding EDX mapping

- [8] B. Friedrich, C. Kräutlein, K. Krone: Melt treatment of copper - "Ways to a high-tech material", Metall 59 (2005) 728-734.
- [9] E. Brunhuber, Guss aus Kupferlegierungen. Berlin: Schiele & Schön, (1986), 3-7949-0444-3.
- [10] M.E. Schlesinger, K. Sole, W.G. Davenport, Extractive Metallurgy of Copper (2011) ISBN: 9780080967905.

(1) Claudia Voigt, Gayle Celaida Gumban, Jana Hubálková, Christos G. Aneziris, Technische Universität Bergakademie Freiberg, Institute of Ceramics, Refractories and Composite Materials, Agricolastr. 17, 09599 Freiberg, Germany